Mathematical Modeling of Light Chain Aggregation and Cardiac Damage in AL Amyloidosis

Andrey V. Kuznetsov

Department of Mechanical and Aerospace Engineering, North Carolina State University,

Raleigh, NC 27695-7910, USA; e-mail: avkuznet@ncsu.edu

Abstract

AL amyloidosis is a rapidly progressive disorder characterized by clonal plasma cell expansion, excessive production of light chains (LCs), and their misfolding into aggregation-prone monomers. These monomers assemble into oligomers and ultimately deposit as amyloid fibrils, particularly within cardiac tissue, where they contribute to myocardial stiffening and direct cardiotoxicity. A mechanistic model was developed to quantify the interplay between these two pathogenic processes and to examine the kinetics of LC aggregation in different compartments. Simulations reveal that LC aggregation exhibits pronounced nonlinearity: oligomer concentrations remain low during early disease stages, followed by exponential growth driven by autocatalytic conversion. When aggregation is assumed to occur within cardiac tissue, fibril deposition is approximately 25 times greater, and oligomer-induced cardiotoxicity is about five times higher, compared with aggregation occurring in the blood plasma. These differences stem from the smaller cardiac volume, which accelerates autocatalytic oligomer formation. A combined cardiac damage criterion, integrating both oligomer-induced cardiotoxicity and fibril-associated myocardial stiffening, was introduced and found to reach values approximately tenfold higher when LC aggregation occurs within cardiac tissue compared with aggregation in the blood plasma. This parameter may serve as a quantitative measure of cardiac aging or disease severity. The model also predicts that therapeutic intervention markedly reduces, but does not eliminate cardiac injury, highlighting the importance of early treatment initiation in AL amyloidosis.

Keywords: cardiotoxicity, Finke−Watzky model; cardiac biomarkers; biomarker of aging

Abbreviations

AL	amyloid light chain
dFLC	difference between plasma concentration of involved and uninvolved free LCs
F-W	Finke-Watzky
Ig	immunoglobulin
LC	light chain

1. Introduction

Immunoglobulin (Ig) light chain (AL) amyloidosis is the most prevalent form of systemic amyloidosis in Western countries, accounting for approximately 75% of cases (Rognoni et al. 2021), (Kazman et al. 2021), (Martinez-Rivas et al. 2022), (Palladini and Merlini 2016). AL amyloidosis is characterized by misfolding of monoclonal Ig light chains (LCs) secreted by clonal plasma cells. These misfolded LCs demonstrate structural instability and a marked propensity to self-aggregate, forming soluble oligomers and insoluble fibrils (Eisele et al. 2015), (Blancas-Mejía and Ramirez-Alvarado 2013). Progressive interstitial infiltration by amyloid fibrils compromises organ architecture and function, most prominently in the heart and kidneys, leading to restrictive cardiomyopathy, nephrotic syndrome, and ultimately multi-organ failure (Rognoni et al. 2021).

Cardiac involvement in AL amyloidosis is especially detrimental, presenting with restrictive cardiomyopathy, diastolic dysfunction, and arrhythmias, and remains the principal determinant of prognosis (Dispenzieri et al. 2003), (Kumar et al. 2012). Once heart failure develops, median survival is limited to only a few months, underscoring the aggressive course of the disease (Dubrey et al. 1998).

Current therapeutic strategies in AL amyloidosis are largely adapted from multiple myeloma and focus on targeting the underlying plasma cell clone to suppress the production of pathogenic LCs (Palladini and Merlini 2016). Despite advances with chemotherapy, stem cell transplantation, proteasome inhibitors, immunomodulatory agents, and monoclonal antibodies, outcomes remain poor in patients with advanced cardiac involvement, highlighting a critical unmet need (Palladini et al. 2020), (Kastritis Efstathios et al. 2021). This is due in part to the lack of a detailed quantitative understanding of the processes that govern LC production, clearance, misfolding, and deposition within tissues. Current clinical approaches rely on indirect biomarkers, such as serum free LC assays and cardiac biomarkers (NT-proBNP, troponins), which provide prognostic information but do not capture the underlying dynamic interactions that drive disease progression (Dispenzieri et al. 2004), (Katzmann et al. 2002).

Mathematical modeling offers a unique framework to bridge this knowledge gap. Mathematical modeling has provided important insights into hematologic malignancies, including clonal plasma cell kinetics, disease progression, and therapeutic resistance (Sullivan and Salmon 1972), (Ayati et al. 2010). In parallel, quantitative frameworks describing amyloid fibrillogenesis have clarified the kinetics of nucleation, elongation, and secondary seeding, mechanisms that underlie the accumulation of amyloid burden (Watzky and Finke 1997), (Knowles et al. 2009), (Cohen et al. 2013). Despite these advances, to the best of the author's knowledge, no existing model has incorporated plasma cell–derived LC production with subsequent fibril formation in AL amyloidosis.

This work extends a previously developed model of transthyretin amyloidosis (Kuznetsov 2025a) by formulating a mathematical framework that characterizes plasma cell clone LC secretion, clearance, and the kinetics of nucleation and fibril growth in AL amyloidosis. The simulation of these processes is designed to (1) quantify the relative contributions of clonal plasma cell expansion and LC aggregation to disease progression, (2) identify key parameters that critically influence the timing and extent of amyloid deposition within cardiac tissue, and (3) establish a theoretical framework for assessing the roles of cardiotoxicity and myocardial stiffening in cardiac injury.

2. Materials and models

2.1. Governing equations

2.1.1. Equations expressing conservation of abnormal clonal plasma cells in the bone marrow and folded LCs secreted by plasma cell clones

The mathematical model is formulated using balance equations for clonal plasma cells and LC species, including monomers, free oligomers, and fibrils (Fig. 1). A lumped capacitance model is employed, assuming spatial homogeneity of clonal plasma cells within the bone marrow and uniform distribution of all LC species across blood plasma and cardiac tissue, with time as the sole independent variable. In this formulation, time is equivalent to calendar age. The dependent variables are defined in Table 1, and model parameters are summarized in Table 2.

AL amyloidosis is a clonal plasma cell dyscrasia that shares biological features with multiple myeloma but represents a distinct clinical entity (Falk et al. 2016). The first equation of the model characterizes the population dynamics of clonal plasma cells, derived from the balance governing the number of these cells. The Gompertz equation is a widely used mathematical model for describing tumor growth, characterized by an initial phase of exponential expansion that gradually decelerates as tumor size approaches a biological maximum or carrying capacity (Vaghi et al. 2020). This model has been successfully adapted to represent hematologic malignancies, including multiple myeloma, by capturing the sigmoidal growth behavior typical of proliferative clonal expansions in constrained environments. In these models, the Gompertzian growth rate slows as the population increases, reflecting limitations imposed by nutrient availability, immune surveillance, and microenvironmental factors (Sullivan and Salmon 1972), (Ribba et al. 2014), (Gallaher et al. 2018).

$$\frac{dN}{dt} = \left(\alpha - \beta \ln\left(\frac{N}{N_0} \right) \right) N - \mu N \tag{1}$$

where the last term on the right-hand side represents the effect of anticancer therapy (Murphy et al. 2016), (Usher 1994). In Eq. (1), α denotes the specific growth rate at $N = N_0$, β is the deceleration factor of the growth rate, and μ is the kinetic constant describing the rate of plasma cell clone elimination by anticancer treatment.

Eq. (1) is solved subject to the following initial condition:

$$N(0) = N_0 \tag{2}$$

where N_0 denotes the number of plasma cell clones at t=0. In AL amyloidosis, the abnormal plasma cells are clonal, arising from a single progenitor cell ($N_0 = 1$) and therefore genetically identical.

The solution to Eqs. (1) and (2) is given by the following function:

$$N = N_0 \exp\left(\frac{\alpha - \mu}{\beta}\left(1 - \exp(-\beta t)\right)\right) \tag{3}$$

For the case of $\mu = 0$, the expression in Eq. (3) reduces to the Gompertzian function, which is defined in Eq. (S1). Further details of the process described by the Gompertzian function are provided in Section S1 of the Supplemental Materials.

If $t \to \infty$, in the absence of anticancer treatment ($\mu = 0$), Eq. (3) reduces to:

$$N_\infty = N_0 \exp\left(\frac{\alpha}{\beta}\right) \tag{4}$$

where N_∞ is the plateau number of plasma cells.

From Eq. (4) the following is obtained:

$$\beta = \frac{\alpha}{\ln\left(\frac{N_\infty}{N_0}\right)} \tag{5}$$

At $t_{AL,f} = 6$ months (1.58×10^7 s)—the median survival time following the onset of congestive heart failure in patients with AL amyloidosis (Hassan et al. 2005)—the clonal plasma cell population is assumed to reach 90% of their number at steady-state (N_∞). Stating this condition for $\mu = 0$, the following equation is obtained:

$$0.9N_{\infty} = N_0 \exp\left(\frac{\alpha}{\beta}\left(1-\exp\left(-\beta t_{AL,f}\right)\right)\right) \tag{6}$$

Substituting Eq. (5) into Eq. (6), the following equation for α is obtained:

$$0.9N_{\infty} = N_0 \exp\left(\ln\left(\frac{N_{\infty}}{N_0}\right)\left(1-\exp\left(-\frac{\alpha}{\ln\left(\frac{N_{\infty}}{N_0}\right)}t_{AL,f}\right)\right)\right) \tag{7}$$

The parameter value for α is found by solving Eq. (7), and the parameter value for β is estimated by substituting the result in Eq. (5).

Although AL amyloidosis originates from proliferation of plasma cell clone, prognosis is determined primarily by the extent of cardiac LC deposition in the heart, making reduction of circulating pathologic LCs the central therapeutic objective (Witteles and Liedtke 2019). Accordingly, the model incorporates conservation equations for LCs at distinct stages of aggregation, including monomeric LCs secreted by clonal plasma cells, soluble oligomers, and insoluble fibrils.

The excess monoclonal LCs fail to assemble into intact Igs and instead exhibit conformational instability, leading to misfolding and aggregation into amyloid fibrils. The progressive deposition of these fibrils in vital organs, particularly heart, disrupts tissue architecture and function, ultimately leading to organ dysfunction and clinical disease manifestations. In AL amyloidosis, either κ or λ LCs may be overproduced, with λ chains more commonly implicated (Falk et al. 2016). Plasma cells secrete λ LCs primarily as monomers; however, once in circulation, these proteins exhibit a strong propensity to self-associate into noncovalent or disulfide-linked dimers (Goldis et al. 2024). In a simplified model, the dimerization of λ LCs may be considered an integral step in the aggregation process of λ LCs into oligomers. Therefore, at the resolution of the present model, the specific LC type (κ or λ) is not differentiated.

In contrast to intrinsically disordered proteins, Ig LCs are natively folded and require partial unfolding as a prerequisite for aggregation (Blancas-Mejía and Ramirez-Alvarado 2013), (Morgan et al. 2019), (Kazman et al. 2021). Although LC unfolding is reversible, in AL amyloidosis the equilibrium is likely shifted toward irreversible misfolding and aggregation (Blancas-Mejía et al. 2015). Once partially unfolded, LCs preferentially misfold and self-associate rather than refolding into their native conformation. For this reason, the transition of folded LCs to the unfolded state is modeled as an irreversible process:

$$F \xrightarrow{k_u} U \tag{8}$$

Formulating the conservation of the number of natively folded LC monomers secreted by plasma cell clones and dividing by V_{plasma} yields the following equation:

$$\frac{d[F]}{dt} = \frac{q_{LC} a_6}{V_{plasma} b_3 N_A} N - k_u [F] - [F] \frac{\ln(2)}{T_{1/2,F,plasma}} \tag{9}$$

In Eq. (9), the terms on the right-hand side correspond to distinct biological processes: (i) secretion of properly folded LCs by clonal plasma cells; (ii) loss due to conversion into misfolded species prone to aggregation; and (iii) clearance governed by the finite half-life of circulating LCs through renal filtration and proximal tubular catabolism (Hutchison et al. 2008), (Sanders 2012).

Eq. (9) is solved subject to the following initial condition:

$$\text{At } t = 0: \qquad [F] = 0 \tag{10}$$

The initial concentration of natively folded LC monomers in Eq. (10) is set to zero, as for sufficiently long simulation times—corresponding to the timescale of cardiac fibril deposition (months) (Hassan et al. 2005)—the influence of the initial condition becomes negligible.

The model incorporates assumptions regarding the site of LC aggregation, considering two potential scenarios: (1) aggregation occurs in blood plasma, generating protofibrils that subsequently deposit in organ tissues and become uniformly distributed by diffusion (Fig. 1a); or (2) unfolding of LCs occurs in blood plasma, after which the unfolded LCs deposit in organ tissues, where aggregation subsequently proceeds locally (Fig. 1b). In this study, LC deposition in cardiac tissue was simulated, as cardiac involvement is associated with the poorest prognosis (Banypersad et al. 2012), (Tahir et al. 2019).

2.1.2. Development of conservation equations describing amyloid fibril formation for the scenario when they aggregate in blood plasma

The minimal model for this scenario tracks unfolded LC monomers susceptible to aggregation, free oligomers in the circulation, oligomers incorporated into amyloid protofibrils within the plasma, and oligomers deposited as amyloid fibrils infiltrating cardiac tissue (Fig. 1a).

In many protein misfolding disorders, aggregation is governed by two principal mechanisms: primary nucleation and secondary nucleation (Rinauro et al. 2024). Secondary nucleation is an autocatalytic

process in which pre-existing aggregates catalyze their own formation. This phenomenon has also been demonstrated in LC aggregation (Kazman et al. 2021), (Pradhan et al. 2023).

LC oligomerization was modeled using the Finke–Watzky (F–W) kinetic framework, a minimal two-step scheme that captures both nucleation and autocatalytic growth (Morris et al. 2008), (Iashchishyn et al. 2017), (Finke et al. 2020). This model has been extensively utilized to characterize aggregation dynamics in various amyloidogenic proteins (Morris et al. 2008). In this framework, the first pseudo-elementary step corresponds to the primary nucleation of LC oligomers, while the second step represents their secondary, autocatalytic conversion into oligomers. The latter process is catalyzed by pre-existing oligomers that act as catalytic templates, enhancing the formation of new oligomers from LC monomers (Aragonès Pedrola et al. 2025).

The first pseudoelementary step corresponds to the primary nucleation of LC oligomers:

$$U \xrightarrow{k_1} B \tag{11}$$

In the F-W model, oligomers are treated as activated monomers capable of autocatalysis. The model does not distinguish between the size or mass of a monomer and an oligomer. The second pseudoelementary step represents the autocatalytic conversion of monomeric LCs into oligomers:

$$U + B \xrightarrow{k_2} 2B \tag{12}$$

Conservation of unfolded LC monomers in blood plasma gives:

$$\frac{d[U]_{plasma}}{dt} = k_u [F] - k_1 [U]_{plasma} - k_2 [U]_{plasma} [B]_{plasma} - [U]_{plasma} \frac{\ln(2)}{T_{1/2,U,plasma}} \tag{13}$$

In Eq. (13), the terms on the right-hand side describe the following processes: (i) gain of unfolded LC monomers through conversion from natively folded monomers (corresponding to the second term in Eq. (9), but with opposite sign); (ii) loss of unfolded monomers via nucleation-driven oligomer formation; (iii) loss of unfolded monomers through autocatalytic oligomer production; and (iv) clearance of unfolded monomers, governed by their finite half-life in circulation due to renal filtration and proximal tubular catabolism (Hutchison et al. 2008), (Sanders 2012).

The transformation of free LC oligomers into protofibrils is simulated using an analogy to coagulation phenomena in colloidal suspensions (Boltachev and Ivanov 2020). In this framework, oligomeric LCs (*B*) are assigned a characteristic half-deposition time, $\theta_{1/2,B}$, defined as the interval required for half of the

oligomer population to incorporate into protofibrils. Conservation of free LC oligomers in plasma, normalized by V_{plasma}, yields:

$$\frac{d[B]_{plasma}}{dt} = k_1[U]_{plasma} + k_2[U]_{plasma}[B]_{plasma} - [B]_{plasma}\frac{\ln(2)}{T_{1/2,B}} - [B]_{plasma}\frac{\ln(2)}{\theta_{1/2,B}} \tag{14}$$

In Eq. (14), the right-hand side terms correspond to the following processes: (i) generation of oligomers through nucleation-driven formation; (ii) additional generation of oligomers via autocatalytic formation (these two terms are equivalent to the second and third terms in Eq. (13), but with opposite signs); (iii) degradation of oligomers due to their finite half-life; and (iv) loss of oligomers through deposition into protofibrils.

Conservation of LC oligomers incorporated into protofibrils circulating in blood plasma, normalized by V_{plasma}, yields the following equation:

$$\frac{d[I]_{plasma}}{dt} = [B]_{plasma}\frac{\ln(2)}{\theta_{1/2,B}} - [I]_{plasma}\frac{\ln(2)}{T_{1/2,I}} - [I]_{plasma}\frac{\ln(2)}{\theta_{1/2,I}} \tag{15}$$

Here, the terms on the right-hand side represent: (i) an increase in the concentration of LC oligomers deposited into protofibrils as free oligomers incorporate into these structures; (ii) a reduction in protofibril concentration in the bloodstream due to their finite half-life; and (iii) a further reduction in concentration resulting from capture of protofibrils in the bloodstream by cardiac tissue.

In this model, protofibrils are assumed to form within the bloodstream, circulate, and deposit in tissues that provide compatible binding sites. The analysis specifically focuses on deposition within cardiac tissue. Conservation of LC oligomers incorporated into fibrils infiltrating the myocardium, after normalization by V_{heart}, yields the following equation:

$$\frac{d[I]_{tissue}}{dt} = [I]_{plasma}\frac{\ln(2)}{\theta_{1/2,I}} - [I]_{tissue}\frac{\ln(2)}{T_{1/2,I}} \tag{16}$$

Here, the terms on the right-hand side represent: (i) an increase in cardiac fibril concentration driven by the capture of circulating protofibrils and their subsequent infiltration into myocardial tissue; and (ii) degradation of existing deposits over time (regression), a phenomenon observed when treatment (for example, high-dose chemotherapy combined with stem cell transplantation) induces hematologic remission (Fitzgerald et al. 2013).

The initial conditions for Eqs. (13)–(16) are given by:

At $t = 0$: $\quad [U]_{plasma} = 0, \quad [B]_{plasma} = 0, \quad [I]_{plasma} = 0, \quad [I]_{tissue} = 0$ (17a,b,c,d)

In Eq. (17), the initial concentrations of all LC species are set to zero, as their influence becomes negligible over the extended simulation timescale corresponding to cardiac fibril deposition (on the order of months) (Hassan et al. 2005).

Details of the numerical solution methodology are provided in Section S2 of the Supplemental Materials.

2.1.3. Development of conservation equations describing amyloid fibril formation for the scenario when they aggregate in cardiac muscle tissue

In the second scenario, unfolded (and prone to aggregation) LC monomers are taken up by myocardial tissue, where they subsequently aggregate to form amyloid fibrils (Fig. 1b). This scenario is supported by evidence that prefibrillar LC precursors exert direct cardiotoxic effects (Ikura et al. 2022), (Rinauro et al. 2024). If aggregation occurred exclusively in the bloodstream with only mature fibrils depositing in cardiac tissue, prefibrillar LCs would not be present within the myocardium.

This model assumes that unfolding of LC monomers occurs in blood plasma. Applying conservation of unfolded monomers in plasma, and normalizing both sides of the equation by V_{plasma} yields the following equation:

$$\frac{d[U]_{plasma}}{dt} = k_u [F] - h_U \frac{S_{heart}}{V_{plasma}} \left([U]_{plasma} - [U]_{tissue} \right) - [U]_{plasma} \frac{\ln(2)}{T_{1/2,U,plasma}} \tag{18}$$

In Eq. (18), the terms on the right-hand side correspond to: (i) generation of unfolded LC monomers via conversion from natively folded species (analogous to the second term on the right-hand side of Eq. (9), but with opposite sign); (ii) deposition of unfolded monomers into cardiac tissue, with $h_U S_{heart} \left([U]_{plasma} - [U]_{tissue} \right)$ representing the total deposition rate into the myocardium; and (iii) clearance of unfolded monomers, determined by their finite half-life due to renal filtration and proximal tubular catabolism (Hutchison et al. 2008), (Sanders 2012). Note that as infiltration of LCs into the cardiac tissue progresses, the total LC concentration in the heart—including all aggregation states, such as monomers, oligomers, and fibrils—becomes greater than that in the plasma and is likely to exceed the total plasma LC concentration. However, the concentration of unfolded LC monomers is assumed to remain higher in the plasma than in the cardiac tissue, providing the driving force for their deposition into the heart. The

concentration of unfolded monomeric LCs within the cardiac tissue remains low because they rapidly assemble into oligomers. Although certain tissues are capable of internalizing specific proteins via receptor-mediated mechanisms, it is unlikely that cardiac tissue possesses dedicated receptors for the uptake of unfolded LCs, which are inherently cytotoxic to the myocardium.

Conservation of the number of unfolded LC monomers in cardiac tissue, normalized by V_{heart}, gives:

$$\frac{d[U]_{tissue}}{dt} = h_U \frac{S_{heart}}{V_{heart}}\left([U]_{plasma} - [U]_{tissue}\right) - k_1[U]_{tissue} - k_2[U]_{tissue}[B]_{tissue} - [U]_{tissue}\frac{\ln(2)}{T_{1/2,U,tissue}} \quad (19)$$

The terms on the right-hand side of Eq. (19) correspond to the following processes: (i) deposition of unfolded monomers into cardiac tissue (analogous to the second term in Eq. (18), but with opposite sign); (ii) and (iii) loss of unfolded monomers through conversion into oligomers via nucleation and autocatalytic mechanisms, respectively; and (iv) clearance of unfolded monomers, determined by their finite half-life within cardiac tissue.

Applying the conservation principle to LC oligomers in cardiac tissue and normalizing the resulting equation by V_{heart} gives the following:

$$\frac{d[B]_{tissue}}{dt} = k_1[U]_{tissue} + k_2[U]_{tissue}[B]_{tissue} - [B]_{tissue}\frac{\ln(2)}{T_{1/2,B}} - [B]_{tissue}\frac{\ln(2)}{\theta_{1/2,B}} \quad (20)$$

The terms on the right-hand side of Eq. (20) correspond to the following processes: (i) and (ii) represent the generation of free LC oligomers from unfolded monomers through nucleation and autocatalytic pathways, respectively (they are analogues to the second and third terms on the right-hand side of Eq. (19), but with opposite signs); (iii) denotes clearance of oligomers due to their finite half-life; and (iv) accounts for their loss through incorporation into LC fibrils.

By applying the conservation principle to LC oligomers sequestered into fibrillar structures within cardiac tissue, and subsequently normalizing the equation by V_{heart}, the following equation is obtained:

$$\frac{d[I]_{tissue}}{dt} = [B]_{tissue}\frac{\ln(2)}{\theta_{1/2,B}} - [I]_{tissue}\frac{\ln(2)}{T_{1/2,I}} \quad (21)$$

The terms on right-hand side of Eq. (21) simulate the following processes: (i) accumulation of LC fibrils through incorporation of free oligomers into existing fibrillar deposits within cardiac tissue (corresponding to the fourth term in Eq. (20), but with opposite sign); and (ii) degradation of established

fibril deposits, a regression that has been observed following successful treatment with high-dose chemotherapy and subsequent stem cell transplantation (Fitzgerald et al. 2013).

Eqs. (18)–(21) are solved subject to the following initial conditions:

$$\text{At } t=0: \qquad [U]_{plasma}=0, \quad [U]_{tissue}=0, \quad [B]_{tissue}=0, \quad [I]_{tissue}=0 \qquad \text{(22a,b,c,d)}$$

In Eq. (22), all LC species are initialized at zero, since over the prolonged simulation period—spanning months, which is consistent with the timescale of cardiac fibril deposition (Hassan et al. 2005)—the effect of initial concentrations becomes negligible.

Table 1. Summary of the model's dependent variables.

Symbol	Definition	Unit
$[B]_{plasma}$	Molar concentration of free LC oligomers in blood plasma	μM
$[B]_{tissue}$	Molar concentration of free LC oligomers in the cardiac tissue	μM
$[F]$	Plasma molar concentration of natively folded LC monomers secreted by clonal plasma cells	μM
$[I]_{plasma}$	Molar concentration of LC oligomers deposited into amyloid protofibrils circulating in blood plasma	μM
$[I]_{tissue}$	Molar concentration of LC oligomers deposited into amyloid fibrils that infiltrated the cardiac tissue	μM
$[U]_{plasma}$	Plasma molar concentration of unfolded LC monomers susceptible to aggregation	μM
$[U]_{tissue}$	Cardiac tissue molar concentration of unfolded LC monomers susceptible to aggregation	μM
N	Number of plasma cell clones in bone marrow	

Table 2. Summary of the model's parameters and their estimated values.

$k_1 = 10^{-6}$ s^{-1}, $k_2 = 10^{-6}$ μM^{-1} s^{-1}, $k_u = 4\times10^{-4}$ s^{-1}, $q_{LC} = 10^5 \ \frac{\text{LC molecules}}{\text{cell s}}$, $\theta_{1/2,B} = 10^7$ s, and $\theta_{1/2,I}$ s.

Symbol	Definition	Unit	Value or range	Reference or estimation method	Value(s) used in computations
a_6	Factor that converts from mol to μmol	$\frac{\mu\text{mol}}{\text{mol}}$	10^6		10^6
b_3	Factor that converts from m^3 to L	$\frac{\text{L}}{\text{m}^3}$	10^3		10^3
a_{21}	Factor that converts from $\frac{\text{mol}}{\mu\text{m}^3}$ to μM	$\frac{\mu\text{M}\ \mu\text{m}^3}{\text{mol}}$	10^{21}		10^{21}
c	Coefficient in Eq. (30)	μM^{-1}			1.4×10^{-3}
h_U	Mass transfer coefficient describing the rate at which unfolded LC monomers deposit onto the endocardial surface (for scenario 2)	m s^{-1}			10^{-6} [a]
k_1	Rate constant describing the first pseudoelementary (nucleation) step in the F-W model of LC oligomer formation	s^{-1}			10^{-8}, 10^{-6}, 10^{-4} [b]

k_2	Rate constant describing the second pseudoelementary (autocatalytic growth) step in the F-W model of LC oligomer formation	$\mu M^{-1}\ s^{-1}$			10^{-8}, 10^{-6}, 10^{-4} [c]
k_u	Rate of unfolding of LC monomers	s^{-1}	4×10^{-4} [d]		4×10^{-5}, 4×10^{-4}, 4×10^{-3}
MW_{LC}	Average molecular weight of an LC monomer (λ or κ)	$g\ mol^{-1}$	2.5×10^{4} [e]	(Basnayake et al. 2011)	2.5×10^{4}
N_A	Avogadro's number	mol^{-1}	6.022×10^{23}		6.022×10^{23}
N_0	Number of plasma cell clones at t=0			(Sender et al. 2023), (Bain 2011), (Lu and Richards 2019)	1 (for simulation of clonal expansion), 0.5×10^{11} (for simulations showing the effects of anticancer treatment) [f]
N_∞	Number of clonal plasma cells at steady-state (the plateau number of plasma cells)		10^{11} [g]	(Sender et al. 2023), (Bain 2011), (Lu and Richards 2019)	10^{11}
$N_{total\ plasma}$	Total plasma cell count in healthy bone marrow		2×10^{10}	(Sender et al. 2023)	2×10^{10}

q_{LC}	Rate of secretion of folded LCs by a single plasma cell belonging to a clonal population	$\frac{\text{LC molecules}}{\text{cell s}}$			0.5×10^5, 10^5, 2×10^5 [h]
S_{heart}	Vascular endothelial surface area within the human heart	m^2			10 [i]
$t_{AL,onset}$	Typical age of onset of AL amyloidosis	s	2.02×10^9 [j]	(Baker 2022)	2.02×10^9
$t_{AL,f}$	Average survival time among patients with AL amyloidosis after the development of congestive heart failure	s	1.58×10^7 [k]	(Hassan et al. 2005)	1.58×10^7
$T_{1/2,B}$	Half-life of LC oligomers	s			6.5×10^7 [l]
$T_{1/2,F,plasma}$	Half-life of natively folded LC monomers in blood plasma	s	7.2×10^3 - 2.1×10^4 [m]	(Tosi et al. 2013)	1.44×10^4
$T_{1/2,I}$	Half-life of LC oligomers incorporated into LC fibrils	s		(Fitzgerald et al. 2013)	6.5×10^7 [n]
$T_{1/2,U,plasma}$	Half-life of unfolded LC monomers in blood plasma	s	7.2×10^3 - 2.1×10^4 [o]	(Tosi et al. 2013)	1.44×10^4

$T_{1/2,U,tissue}$	Half-life of unfolded LC monomers in cardiac tissue	s			6.5×10^{7} [p]
V_{plasma}	Average plasma volume in the human body	m^3	0.003 [q]	(Sharma and Sharma 2025)	0.003
V_{heart}	Total myocardial tissue volume within the human heart	m^3	5.76×10^{-4} [r]	(Betts 2013)	5.76×10^{-4}
α	Specific growth rate of clones at $N = N_0$ (at t=0)	s^{-1}		The value of α was determined by solving Eq. (7)	
β	Deceleration factor of the growth rate of clones	s^{-1}		The value of β was estimated by substituting the value of α into Eq. (5)	
μ	Kinetic constant describing a rate of killing of plasma cell clones by an anticancer treatment	s^{-1}			0 (no anticancer treatment), 10^{-6} [s]
$\theta_{1/2,B}$	Half-deposition time for free LC oligomers to be incorporated into LC fibrils	s			10^5, 10^7, 10^9 [t]
$\theta_{1/2,I}$	Half-deposition time required for LC-derived amyloid fibrils in blood	s			10^5, 10^7, 10^9 [u]

	plasma to accumulate within cardiac tissue				
$\rho_{fibrils}$	Density of LC fibrils	g/μm^3	1.35×10^{-12} [v]	(Cavicchi et al. 2018)	1.35×10^{-12}
$\Xi_{comb,crit}$	Critical threshold of the combined extent of cardiac damage, beyond which survival is no longer possible	μM s			8×10^{11}
ω	Weighting factor in Eq. (28)	μM s			1.17×10^{12}
%AL	Expansion of space between cardiomyocytes due to infiltration of LC fibrils [w]	%	30.5	(Maceira et al. 2005)	30.5

[a] Values of h_U below 10^{-7} m s^{-1} yield unrealistically high values of $[U]_{tissue}$, whereas increasing h_U above 10^{-5} m s^{-1} produces no further effect on the solution. The average value of 10^{-6} m s^{-1} is used for computations.

[b] In the absence of published kinetic parameters specific for LC aggregation within the F-W model framework, three representative values for the nucleation rate constant, k_1 —10^{-8}, 10^{-6}, 10^{-4} s^{-1}—were selected. These values were guided by the range of nucleation rates reported for various protein systems in (Morris et al. 2008), as summarized in Table S1 of (Kuznetsov 2025b).

[c] In the absence of published kinetic parameters specific for LC aggregation within the F-W model framework, three representative values for the kinetic constant describing autocatalytic growth, k_2 —10^{-8}, 10^{-6}, 10^{-4} μM^{-1} s^{-1}—were selected. These values were guided by the range of autocatalytic growth rates reported for various protein systems in (Morris et al. 2008), as summarized in Table S1 of (Kuznetsov 2025b).

[d] The unfolding rate constant was set to $k_u = 4 \times 10^{-4}$. This value is obtained as follows: $k_u = \frac{\ln 2}{T_{1/2,F \to U}}$, where half-life of folded LCs prior to transition to the unfolded state, $T_{1/2,F \to U}$, was estimated to be 0.5 hours. This choice is justified as follows: if the folded-to-unfolded transition were substantially slower, most unfolded LCs would be eliminated by clearance in the kidneys before reaching the unfolded state in which aggregation can occur. Therefore, the half-life for unfolding must be considerably shorter than the clearance half-life of folded LC, which has been reported to be 2–6 hours (Tosi et al. 2013). On this basis, a value of 0.5 hours was selected for $T_{1/2,F \to U}$.

[e] Although minor differences exist between the molecular weights of λ and κ LCs, the average molecular weight of a LC is approximately 25 kDa (Basnayake et al. 2011).

[f] The number of plasma cells in healthy bone marrow, $N_{total\ plasma}$, is estimated as 2×10^{10} (Sender et al. 2023). Since plasma cells normally account for approximately 2% of bone marrow cells (Bain 2011), compared to about 10% in AL amyloidosis (Lu and Richards 2019), the total plasma cell population in AL amyloidosis increases approximately fivefold, primarily due to clonal expansion. Model simulations of clonal expansion were initiated with a single plasma cell. This corresponds to a total clonal plasma cell population of $5 \times 2 \times 10^{10} = 10^{11}$ cells. Simulations assessing the effects of anticancer treatment were initiated with a clonal plasma cell population equal to one-half of this value.

[g] The total number of plasma cells in healthy bone marrow has been estimated at approximately 2×10^{10} cells (Sender et al. 2023). For a healthy human, plasma cells constitute ~2% of bone marrow cellularity (Bain 2011), whereas in AL amyloidosis they account for ~10% (Lu and Richards 2019). This shift corresponds to an approximately fivefold increase in the plasma cell number, attributable predominantly to clonal proliferation. The steady-state clonal plasma cell burden (plateau phase) is therefore estimated at $5 \times 2 \times 10^{10} = 10^{11}$ cells.

[h] Most published studies report the difference between involved and uninvolved free LCs (dFLC). In AL amyloidosis, a moderate disease burden is typically defined as a dFLC of 180–400 mg/L, whereas values exceeding 400 mg/L indicate a high burden (Saunders et al. 2025). To convert LC concentrations from mg/L to μM, the following relationship is applied:

$$[LC](\mu\text{M}) = \frac{[LC](\mu\text{g/L})}{MW_{LC}} = 0.04[LC](\mu\text{g/L}) \tag{23}$$

As an example, a representative LC monomer concentration corresponding to a high burden of 500 mg/L is approximately 20 μM. The total molar concentration of LC monomers (both folded and unfolded) in blood plasma can be calculated as $[F]+[U]_{plasma}$. Computational analyses performed with varying values of q_{LC} (data not shown) suggest that an estimated q_{LC} value of $10^5 \frac{\text{LC molecules}}{\text{cell s}}$ yields a free LC monomer concentration of approximately 20 μM.

[i] In the adult human, the cumulative surface area of all capillary networks has been estimated at approximately 6,000 m² (Li and Jain 2009). By comparison, the alveolar surface area in the lungs is estimated to be about 100 m² (Ananda Rao and Johncy 2022). Given these values, the vascular surface area within the human heart is expected to be substantially smaller than that of the alveoli and is approximated at 10 m².

[j] The median age at diagnosis of LA amyloidosis is 64 years (Baker 2022).

[k] Once congestive heart failure develops in patients with AL amyloidosis, the median survival is markedly reduced, averaging only about 6 months (Hassan et al. 2005).

[l] In the absence of published data, the half-life of LC oligomers was assumed to be the same as that of LC fibrils, $T_{1/2,I}$.

[m] The serum half-life of folded LC monomers is approximately 2–6 hours (Tosi et al. 2013).

[n] Studies have demonstrated that effective therapy for AL amyloidosis may result in a gradual regression of amyloid deposits (van Gameren et al. 2009). (Fitzgerald et al. 2013) reported a mean time to cardiac remission of approximately 25 months, which has been used as an estimate for the half-life of LC–derived fibrils.

[o] It is assumed that folded and unfolded free LCs have the same half-life in blood plasma.

The serum half-life of free LCs is approximately 2–6 hours (Tosi et al. 2013).

[p] In the absence of published data, and given that LC monomers within cardiac tissue are not subject to renal clearance, their half-life was assumed to be the same as that of LC fibrils, $T_{1/2,I}$.

[q] With an average total blood volume of 5 L in the human body and plasma accounting for roughly 60% of it (Sharma and Sharma 2025), the estimated volume of plasma is about 3 L.

[r] The human heart is often compared to the size of a closed fist and typically measures about 12 cm long, 8 cm wide, and 6 cm thick (Betts 2013).

[s] A value of $\mu = 0$ corresponds to no anticancer treatment. The alternative value of μ was selected to ensure that the clonal plasma cell population was reduced by at least 95% over a 6-month period.

[t] Assumed range.

[u] Assumed range.

[v] Proteins, regardless of their specific type, are generally assumed to have an average density of approximately 1.35 g/cm³ (Cavicchi et al. 2018).

[w] This results in wall thickening, reduced chamber size, and increased stiffness, thereby producing the restrictive cardiomyopathy phenotype.

2.2. Calculation of the volume occupied by LC fibrils in cardiac tissue

Although AL amyloidosis arises from an underlying plasma cell dyscrasia, clinical outcomes are influenced more by the extent of cardiac involvement than by the characteristics of the hematologic malignancy itself (Witteles and Liedtke 2019). Deposition of LC fibrils in the interstitial space between cardiomyocytes increases myocardial stiffness. Accordingly, it is important for the model to predict the extent of cardiac volume expansion resulting from fibrillar infiltration.

This is done by calculating the total number of LC monomers incorporated into fibrils, $N_{fibrils}$, over a given time *t*. In the F-W model, monomers and oligomers are assumed to have the same molecular weight (see Eq. (11)). Using the approach adapted from (Watzky et al. 2008), the following equation is obtained:

$$N_{fibrils}(t) = \frac{[I]_{tissue}(t)}{a_{21}} V_{heart} N_A \tag{24}$$

where N_A represents Avogadro's number.

An alternative approach for determining $N_{fibrils}(t)$ is based on the principle that the number of monomers incorporated into fibrils is proportional to the volume of fibrillar deposits within the myocardium. This relationship can be expressed using the following equation, as also reported in (Watzky et al. 2008):

$$N_{fibrils}(t) = \frac{V_{fibrils}(t)\rho_{fibrils}}{MW_{LC}} N_A \tag{25}$$

where MW_{LC} denotes the molecular weight of an LC monomer (λ or κ), $V_{fibrils}(t)$ represents the volume of LC amyloid fibril deposits within the myocardium at time *t*, and $\rho_{fibrils}$ specifies the density of the fibrillar material.

By equating the right-hand sides of Eqs. (24) and (25) and solving for the fraction of myocardial volume occupied by LC fibrils, the following equation is obtained:

$$\frac{V_{fibrils}(t)}{V_{heart}} = \frac{[I]_{tissue}(t)}{a_{21}} \frac{MW_{LC}}{\rho_{fibrils}} \tag{26}$$

2.3. Criteria for accumulated cardiotoxicity of LC oligomers, the combined effect of cytotoxicity and myocardial stiffening, and the proposed biomarker of cardiac cellular biological age

Substantial evidence indicates that soluble oligomers are the main species responsible for cytotoxicity in amyloid diseases. Proposed mechanisms include disruption of membrane integrity through interactions of their hydrophobic surfaces with phospholipids, as well as the induction of apoptotic pathways (Absmeier et al. 2023), (Blancas-Mejía and Ramirez-Alvarado 2013), (Pradhan et al. 2023).

Analogous to criteria previously proposed to quantify accumulated neurotoxicity induced by Aβ oligomers in Alzheimer's disease (Kuznetsov 2025c) and by α-synuclein oligomers in Parkinson's disease (Kuznetsov 2025d), a parameter was defined to quantify accumulated cardiotoxicity attributable to LC oligomers as follows.

For the scenario in which amyloid fibril aggregation takes place in the blood plasma, this parameter is defined as follows:

$$\Xi(t) = \int_0^t [B]_{plasma}(\hat{t})\, d\hat{t} \tag{27a}$$

For the scenario in which amyloid fibril aggregation occurs in the cardiac muscle tissue, this parameter is defined as:

$$\Xi(t) = \int_0^t [B]_{tissue}(\hat{t})\, d\hat{t} \tag{27b}$$

Because cardiac injury in AL amyloidosis arises from both the direct cytotoxicity of LC oligomers and the increased myocardial stiffness caused by fibrillar deposition within cardiac tissue (Falk et al. 2016),

the combined extent of cardiac damage —reflecting contributions from both mechanisms—is quantified by the following parameter:

$$\Xi_{comb}(t) = \Xi(t) + \varpi \frac{V_{fibrils}(t)}{V_{heart}} \tag{28}$$

Because LC oligomers circulating in the blood plasma are likely less cytotoxic than those present within cardiac tissue, a scaling factor less than unity should, in principle, be applied to $\Xi(t)$ in Eq. (28) when modeling the scenario in which LCs aggregate in the plasma. This adjustment was not implemented here due to insufficient experimental data to determine the appropriate value of this factor.

The value of ϖ is estimated as follows. It is assumed that cardiotoxicity and myocardial stiffening each contribute around half of overall cardiac injury in AL amyloidosis. From Fig. S8b for $q_{LC} = 10^5$ folded LC molecules per plasma cell per second, the maximum value of Ξ is determined to be 3.58×10^{11} μM·s. The proportion of cardiac tissue occupied by LC fibril deposits is estimated at 30.5% (%AL, Table 2). On this basis, the value of ϖ is calculated as:

$$\varpi = \frac{3.58 \times 10^{11}}{0.305} = 1.17 \times 10^{12} \text{ μM s} \tag{29}$$

(Dormann and Lemke 2024) suggested the development of a new type of aging clock that uses the aggregation dynamics of intrinsically disordered proteins (IDPs)—including amyloid-β (Aβ), tau, α-synuclein, and TDP-43—as a molecular indicator of biological aging. In the present study, this concept is further advanced and applied to Ig LCs, which are natively folded proteins that must undergo partial unfolding as a prerequisite for aggregation. The concept of biological age of the heart (hereafter referred to as biological age) is introduced and defined as follows:

$$\text{biological age} = \text{calendar age} + c\Xi_{comb}(t) = t_{AL,onset} + t + c\Xi_{comb}(t) \tag{30}$$

Simulations modeling amyloid fibril formation within cardiac muscle tissue (scenario 2), conducted using the following parameter values: $k_1 = 10^{-6}$ s^{-1}, $k_2 = 10^{-6}$ μM^{-1} s^{-1}, $k_u = 4 \times 10^{-4}$ s^{-1}, $N_0 = 1$ cell, $q_{LC} = 10^5 \frac{\text{LC molecules}}{\text{cell s}}$, $\theta_{1/2,B} = 10^7$ s, $\mu = 0$ cells^{-1}, together with additional parameter values listed in Table 2, yielded a result of $\Xi_{comb}(t_{AL,f}) = 8 \times 10^{11}$ μM s. Assuming that AL amyloidosis onset occurs at age 64, progresses over 6-months, and that the patient's biological age reaches 100 years (the practical longevity limit) by age 64.5, the following estimate for parameter *c* in Eq. (30) is derived:

$$c = \frac{(100-64)-0.5}{8\times 10^{11}} = 1.4\times 10^{-3}\ \mu\text{M}^{-1} \tag{31}$$

2.4. Sensitivity of the criterion characterizing the combined effects of cytotoxicity and myocardial stiffening to various model parameters

The sensitivity of the criterion quantifying combined cardiac damage—encompassing both cardiotoxicity and myocardial stiffening—to various model parameters was investigated. Sensitivity analysis was performed by calculating local sensitivity coefficients, defined as the first-order partial derivatives of the output variable (the combined cardiac damage criterion) with respect to individual parameters, such as the secretion rate of LCs by a single plasma clone cell, q_{LC}. The methodology followed established approaches (Beck and Arnold 1977), (Zadeh and Montas 2010), (Zi 2011), (Kuznetsov and Kuznetsov 2019).

For example, the sensitivity coefficient of the combined damage criterion with respect to q_{LC} was computed using the following equation:

$$\frac{\partial \Xi_{comb}}{\partial q_{LC}} \approx \left.\frac{\Xi_{comb}\left(q_{LC}+\Delta q_{LC}\right)-\Xi_{comb}\left(q_{LC}\right)}{\Delta q_{LC}}\right|_{\text{other parmeters kept constant}} \tag{32}$$

where $\Delta q_{LC} = 10^{-3} q_{LC}$ denotes the step size employed for numerical differentiation. Different step sizes were tested to verify the independence of the sensitivity coefficients from the step size.

To enable direct comparison across parameters expressed in different units and magnitudes, dimensionless relative sensitivity coefficients were also calculated, following the procedures outlined in (Zadeh and Montas 2010), (Kuznetsov and Kuznetsov 2019). For example:

$$S_{q_{LC}}^{\Xi_{comb}} = \frac{q_{LC}}{\Xi_{comb}} \frac{\partial \Xi_{comb}}{\partial q_{LC}} \tag{33}$$

$S_{q_{LC}}^{\Xi_{comb}}$ represents the fractional change in Ξ_{comb} resulting from a fractional change in q_{LC}, i.e., $\frac{\partial \Xi_{comb} / \Xi_{comb}}{\partial q_{LC} / q_{LC}}$.

3. Results

The concentration of clonal plasma cells initially increases exponentially; however, as proliferation slows, the growth curve assumes an S-shaped (sigmoidal) form and eventually reaches a steady-state value of 10^{11} cells (see footnote *g* after Table 2), consistent with the Gompertz model of cancer cell growth (Fig. S1a). The concentration of folded Ig LC monomers secreted by clonal plasma cells into the blood plasma also exhibits an S-shaped growth profile. The plasma concentration of folded LCs increases with the secretion rate of LCs by an individual clonal plasma cell, and this increase is roughly proportional to the rate of secretion (Fig. S1b).

The plasma molar concentration of unfolded Ig LC monomers initially increases over approximately the first half of the simulated period (the whole simulated period is 6 months) and subsequently declines (Fig. S2). The initial rise reflects the increasing number of folded LC monomers secreted by plasma cells, which undergo unfolding to produce unfolded species. In the latter half of the process, the concentration of unfolded LCs decreases due to their conversion into oligomers, especially by autocatalysis. Notably, in the scenario where aggregation occurs within the cardiac tissue, the concentration of unfolded LCs begins to rise again toward the end of the simulation period (Fig. S2b). The concentration of unfolded LCs increases with increasing secretion rate of folded LCs (Fig. S2).

(Saunders et al. 2025) reported that in AL amyloidosis, the difference between the concentrations of involved and uninvolved free LCs typically ranges from 180 to 400 mg/L. According to Eq. (23), this corresponds to approximately 7.2–16 μM. Because the number of clonal plasma cells in AL amyloidosis is approximately fivefold greater than that of normal plasma cells (Bain 2011), (Lu and Richards 2019), this range can serve as an approximate estimate of the concentration of involved LCs. These values are consistent with the concentrations of $[F]+[U]_{plasma}$ that follow from Figs. S1b and S2.

The concentration of folded LC monomers that infiltrate the cardiac tissue in the scenario where LC aggregation occurs within the tissue (Fig. S3) is only slightly lower than the concentration of unfolded LCs in the plasma in the same scenario (Fig. S2b), which can be attributed to the high value of h_U (10^{-6} $m \cdot s^{-1}$, Table 2).

The concentration of free LC oligomers in blood plasma for the scenario of aggregation occurring in the plasma (Fig. S4a), and in cardiac tissue for the scenario of aggregation occurring within the tissue (Fig. S4b), increases slowly during the first three months and much more rapidly during the subsequent three months. The initial slow increase is due to the nucleation-driven formation of oligomers from unfolded LC monomers, a kinetically slow process that precedes the buildup of a sufficient oligomer population capable of catalyzing their own production. In the later stage, oligomer formation accelerates due to

autocatalytic conversion, which proceeds much faster. The final oligomer concentration is approximately five times higher when aggregation occurs in cardiac tissue, reflecting the roughly fivefold smaller volume of the heart compared to the plasma. Consequently, for an equivalent total number of oligomers, their concentration in the heart is proportionally higher, leading to an approximately fivefold greater rate of oligomer synthesis via autocatalytic conversion.

The plasma concentration of LC oligomers incorporated into amyloid protofibrils, $[I]_{plasma}$, exhibits a pattern similar to that of free oligomers, $[B]_{plasma}$, but is approximately fivefold lower (compare Fig. S5 with Fig. S4a). This difference arises from the long half-deposition time of oligomers into fibrils, $\theta_{1/2,B}$.

The curves displaying the time-dependent concentrations of LC oligomers incorporated into amyloid fibrils infiltrating the cardiac tissue exhibit similar profiles under both scenarios—LC aggregation occurring in the plasma and LC aggregation occurring within the cardiac tissue. However, the concentration is approximately 25 times higher when aggregation occurs in the cardiac tissue (compare Fig. S6b with Fig. S6a). This difference arises because the concentration of LC oligomers is approximately fivefold higher in the scenario where aggregation occurs within the cardiac tissue (compare Fig. S4b with Fig. S4a). An additional fivefold difference results from the fact that, in the plasma aggregation scenario, fibrils must deposit into the cardiac tissue, and the concentration of fibrils in the plasma is about fivefold higher than in the cardiac tissue (compare Fig. S6a with Fig. S5). The latter effect is due to the large half-deposition time of fibrils from the plasma to the cardiac tissue, $\theta_{1/2,I}$.

The curves displaying the time-dependent fraction of myocardial volume occupied by LC fibrils are similar in shape for both aggregation scenarios—in the plasma and within the cardiac tissue—but are approximately 25 times higher when aggregation occurs in the cardiac tissue (compare Fig. S7a and Fig. S7b). When LCs aggregate within the cardiac tissue, a secretion rate of $q_{LC} = 10^5$ folded LC molecules per plasma cell per second results in approximately 40% of the myocardium being occupied by LC fibrils after 6 months of disease progression (Fig. S7b). At a secretion rate of $q_{LC} = 2\times10^5$ folded LC molecules per plasma cell per second, this fraction increases to about 90% after 6 months (Fig. S7b), which likely represents an unrealistically high value, as amyloid fibrils have been estimated to occupy approximately 30.5% of the myocardial volume in patients at the terminal stage of the disease (Maceira et al. 2005).

The criterion representing accumulated cardiotoxicity induced by LC oligomers attains values approximately fivefold higher in the scenario where LC aggregation occurs within the cardiac tissue

(compare Fig. S8b with Fig. S8a). This difference is attributable to the roughly fivefold higher oligomer concentration observed in this scenario (compare Fig. S4b with Fig. S4a). Notably, most of the toxicity accumulation occurs during the latter half of the process, during which it exhibits exponential growth.

The criterion representing the combined effects of LC oligomer-induced cardiotoxicity and myocardial stiffening, Ξ_{comb}, reaches values approximately tenfold higher in the scenario where LC aggregation occurs within the cardiac tissue (compare Fig. 2b and 2a). In the cardiac tissue aggregation scenario, at an LC secretion rate of $q_{LC}=10^5$ folded LC molecules per plasma cell per second, the combined criterion attains a critical value corresponding to patient mortality after 6 months of disease progression. When the secretion rate increases to $q_{LC}=2\times10^5$ folded LC molecules per plasma cell per second, this critical threshold is reached after 5 months (Fig. 2b). In contrast, under the scenario of LC aggregation in the blood plasma, even at an LC secretion rate of $q_{LC}=2\times10^5$ folded LC molecules per plasma cell per second, the combined criterion remains approximately fourfold below the critical value after 6 months of disease progression. These findings suggest that LC aggregation within the cardiac tissue leads to substantially faster disease progression than aggregation occurring in the blood plasma.

Because the combined criterion shown in Fig. 2 is used as a biomarker of aging, Fig. S9, which depicts biological age as a function of chronological age, demonstrates a similar trend. When LC aggregation occurs within cardiac tissue, and the LC secretion rate is $q_{LC}=10^5$ folded LC molecules per plasma cell per second, the biological age reaches 100 years (the assumed human lifespan) at a calendar age of 64.5 years (Fig. S9b). It is assumed that the disease onset occurs at a calendar age of 64 years, resulting in cardiac failure within 6 months. In contrast, when LC aggregation takes place in the blood plasma, the increase in biological age is much slower. For the same secretion rate q_{LC}, the biological age reaches only 68 years after 6 months of disease progression (Fig. S9a).

Figs. S10–S18 and Fig. 3 illustrate the effect of the LC monomer unfolding rate constant, k_u. The unfolding rate constant does not affect the number of plasma cell clones (Fig. S10a). An increase in k_u decreases the concentration of folded LC monomers by accelerating their conversion into unfolded monomers (Fig. S10b). Consequently, higher values of k_u increase the concentration of unfolded LC monomers in the blood plasma (Fig. S11). For the scenario in which LC aggregation occurs within cardiac tissue, increasing k_u similarly elevates the concentration of unfolded LC monomers in the cardiac tissue (Fig. S12). The concentration of free (not incorporated into fibrils) LC oligomers also rises with increasing k_u (Fig. S13). Likewise, the concentrations of oligomers incorporated into fibrils in the blood plasma (Fig. S14) and in

the cardiac tissue (Fig. S15) both increase with increasing k_u. The same trend is observed for the fraction of myocardial volume occupied by LC fibrils (Fig. S16) and for the accumulated cardiotoxicity induced by LC oligomers (Fig. S17).

When LC aggregation occurs within the cardiac tissue, the criterion representing the combined effects of LC oligomer–induced cardiotoxicity and myocardial stiffening, Ξ_{comb}, reaches half of its critical value (corresponding to patient death) after six months of disease progression for $k_u = 4\times10^{-5}$ s^{-1} (Fig. 3b). For the same aggregation scenario, Ξ_{comb} attains the critical value of 8×10^{11} μM·s after six months for $k_u = 4\times10^{-4}$ s^{-1} and approximately one week earlier for $k_u = 4\times10^{-3}$ s^{-1} (Fig. 3b). These results suggest that at lower values, increases in k_u have a strong amplifying effect on Ξ_{comb}, whereas this effect diminishes as k_u becomes larger. When LC aggregation occurs in the blood plasma, Ξ_{comb} remains approximately tenfold below its critical value even for the highest tested k_u value (4×10^{-3} s^{-1}) (Fig. 3a).

Biological age also depends on k_u. In the cardiac tissue aggregation scenario, the biological age reaches approximately 100 years after six months of disease progression for $k_u = 4\times10^{-4}$ s^{-1} and about 105 years for $k_u = 4\times10^{-3}$ s^{-1} (Fig. S18b). In contrast, when aggregation occurs in the blood plasma, the biological age after six months of disease progression is approximately 68 and 68.5 years for $k_u = 4\times10^{-4}$ s^{-1} and 4×10^{-3} s^{-1}, respectively (Fig. S18a).

An increase in the kinetic constant describing the nucleation rate of LC oligomers, k_1, results in a slight increase of the criterion representing the combined effects of LC oligomer–induced cardiotoxicity and myocardial stiffening, Ξ_{comb} (Fig. S19), as well as a modest increase in biological age (Fig. S20). However, the influence of k_1 is considerably smaller than that of k_u.

An increase in the kinetic constant describing the rate of LC oligomer formation by autocatalysis, k_2, leads to a rise in Ξ_{comb}, particularly at lower values of k_2 (Fig. S21). The biological age demonstrates a similar trend. When LC aggregation occurs in cardiac tissue, the biological age after 6 months of disease progression is approximately 66 years for $k_2 = 10^{-8}$ μM^{-1}s^{-1}, about 101 years for $k_2 = 10^{-6}$ μM^{-1}s^{-1}, and approximately 105 years for $k_2 = 10^{-4}$ μM^{-1}s^{-1} (Fig. S22b).

The combined criterion characterizing cardiac damage in AL amyloidosis, Ξ_{comb}, after six months of disease progression, increases with higher rates of LC monomer production per plasma cell, q_{LC} (Fig. 4). When LC aggregation occurs within cardiac tissue, the curve displaying $\Xi_{comb}(q_{LC})$ crosses the critical

threshold of Ξ_{comb} corresponding to heart failure at a specific value of $q_{LC,crit}$. The critical value of q_{LC} increases as the LC monomer unfolding rate constant, k_u, decreases (Fig. 4b). When LC aggregation occurs in the blood plasma, Ξ_{comb} remains below its critical threshold, reaching values approximately fourfold lower than the critical threshold even at the highest k_u value of 4×10^{-3} s^{-1} (Fig. 4a).

The sensitivity of the criterion characterizing cardiac damage, Ξ_{comb}, to q_{LC} is positive (Fig. S23), indicating that Ξ_{comb} increases with rising q_{LC}, consistent with the trend shown in Fig. 4.

Similar to Ξ_{comb}, the biological age after six months of disease progression increases with the secretion rate of LC monomers, q_{LC}. An increase in the unfolding rate constant of LC monomers, k_u, also leads to an increase in biological age (Fig. S24). For instance, at the highest secretion rate q_{LC} (2×10^5 LC molecules per plasma cell per second), in the scenario of LC aggregation within cardiac tissue, the biological age reaches approximately 103 years for $k_u = 4\times10^{-5}$ s^{-1}, 142 years for $k_u = 4\times10^{-4}$ s^{-1}, and 151 years for $k_u = 4\times10^{-3}$ s^{-1} (Fig. S24b). In contrast, for the scenario of LC aggregation in blood plasma, the corresponding biological ages are approximately 68, 72, and 73 years, respectively (Fig. S24a).

For the scenario of LC aggregation in cardiac tissue, an increase in the half-deposition time required for free LC oligomers to be incorporated into fibrils, $\theta_{1/2,B}$, decreases the combined criterion characterizing cardiac damage, Ξ_{comb} (Fig. 5b). Interestingly, in the scenario of LC aggregation in the blood plasma, Ξ_{comb} is independent of $\theta_{1/2,B}$ (Fig. 5a). A similar pattern is observed in Fig. S25a, which demonstrates that biological age remains unaffected by $\theta_{1/2,B}$ when LC aggregation occurs in the plasma.

To elucidate the reason for this unexpected phenomenon, the dependences of Ξ_{comb} vs $\theta_{1/2,B}$ were plotted in Fig. 6. For a secretion rate of $q_{LC} = 10^5$ LC molecules per plasma cell per second, under the scenario in which LC aggregation occurs in the blood plasma (blue dashed curve in Fig. 6a), Ξ_{comb} is nearly independent of $\theta_{1/2,B}$. The blue dashed curve in Fig. 6a is almost horizontal, with only a minor deviation—a small peak in the range of $10^5\,\text{s} < \theta_{1/2,B} < 10^7\,\text{s}$—whose magnitude (from minimum to maximum) is less than 10^{10} μM·s. In contrast, when aggregation occurs within the cardiac tissue, the variation in blue dashed line in Fig. 6b is approximately 2×10^{12} μM·s, about 200-fold greater than that observed in Fig. 6a.

A similar pattern is observed for biological age. For a secretion rate of $q_{LC} = 10^5$ folded LC molecules per plasma cell per second, in the case of LC aggregation occurring in the blood plasma, the variation in

biological age is approximately 0.5 years (blue dashed line in Fig. S26a). For the same value of q_{LC}, when aggregation occurs within the cardiac tissue, the variation in biological age is approximately 100 years (blue dashed line in Fig. S26b), representing the same 200-fold increase as observed in Fig. 6b.

To elucidate the near independence of Ξ_{comb} from $\theta_{1/2,B}$, the behaviors of the two components comprising Ξ_{comb} (as defined in Eq. (28)) were analyzed. The first component, Ξ, represents cardiotoxicity attributable to LC oligomers. The accumulated cardiotoxicity, Ξ, increases with rising $\theta_{1/2,B}$ (Fig. 7), because higher values of $\theta_{1/2,B}$ extend the residence time of oligomers before their incorporation into fibrils. This leads to an increased oligomer concentration (Fig. 8) and consequently greater cardiotoxicity, as oligomers are considered the primary toxic species.

The second component reflects the fraction of myocardial volume occupied by fibrils, $V_{fibrils} / V_{heart}$. As $\theta_{1/2,B}$ increases, this fraction decreases (Fig. 9), since a larger $\theta_{1/2,B}$ corresponds to more stable oligomers that convert into fibrils more slowly. This trend is consistent with the reduced concentration of LC oligomers deposited into amyloid protofibrils for increased $\theta_{1/2,B}$ (Fig. 10).

Thus, the combined criterion characterizing cardiac damage, Ξ_{comb}, comprises two opposing effects: one that increases with $\theta_{1/2,B}$ and another that decreases with $\theta_{1/2,B}$. In Figs. 5a and 6a, which represent the scenario of LC aggregation occurring in the blood plasma, these opposing effects nearly cancel each other, resulting in the apparent independence of Ξ_{comb} from $\theta_{1/2,B}$.

For the scenario in which LC aggregation occurs in the blood plasma, at a secretion rate of $q_{LC} = 10^5$ LC molecules per plasma cell per second, the sensitivity of Ξ_{comb} to $\theta_{1/2,B}$ is positive within the range $10^5\,\mathrm{s} < \theta_{1/2,B} < 10^6\,\mathrm{s}$ (Fig. 11a), corresponding to the slight increase of Ξ_{comb} with $\theta_{1/2,B}$ observed in Fig. 6a in this range (dashed blue line). The sensitivity becomes negative in the range $5\times10^7\,\mathrm{s} < \theta_{1/2,B} < 10^9\,\mathrm{s}$ (Fig. 11a), consistent with the slight decrease of Ξ_{comb} with $\theta_{1/2,B}$ in this range in Fig. 6a. Within the range $5\times10^7\,\mathrm{s} < \theta_{1/2,B} < 10^9\,\mathrm{s}$, the sensitivity approaches zero (Fig. 11a), aligning with the nearly horizontal, $\theta_{1/2,B}$-independent behavior of Ξ_{comb} shown in Fig. 6a in this range.

For the scenario in which LC aggregation occurs within the cardiac tissue, the sensitivity is negative throughout the range $2\times10^5\,\mathrm{s} < \theta_{1/2,B} < 10^9\,\mathrm{s}$ (Fig. 11b), consistent with the decrease of Ξ_{comb} with $\theta_{1/2,B}$ observed in Fig. 6b in this range.

The case involving anticancer treatment is analyzed in Figs. S27–S35 and Fig. 12. The initial number of plasma cell clones was assumed to be 5×10^{10} cells. During therapy, the clone population progressively declined and was completely eliminated after six months of treatment (Fig. S27a). Because folded LC monomers are secreted by plasma cell clones, their concentration likewise decreased over time (Fig. S27b).

The concentration of unfolded LC monomers susceptible to aggregation declined sharply, nearly disappearing within the first month (Figs. S28 and S29). The concentration of free oligomers initially increased during the first month due to conversion of unfolded monomers into oligomers but subsequently decreased as no new oligomers were formed and the remaining oligomeric species were incorporated into fibrils (Fig. S30).

The concentration of oligomers incorporated into fibrils continued to rise over the six months period, indicating ongoing deposition of free oligomers into fibrillar structures (Figs. S31 and S32). In Fig. S31, the concentration of fibril-incorporated oligomers circulating in the blood plasma approaches a steady-state value at longer times as the oligomer population declines (Fig. S30a). The myocardial volume fraction occupied by fibrils also increased gradually over time; however, for a secretion rate of $q_{LC}=10^5$ LC molecules per plasma cell per second, this fraction reached only approximately 13% after six months in the scenario where LC aggregation occurred within cardiac tissue (Fig. S33).

Accumulated cardiotoxicity (Fig. S34) increased monotonically despite the decline in oligomer concentration after the first month (Fig. S30), because cardiotoxicity is defined as the time integral of oligomer concentration and therefore continues to accumulate even as oligomer levels decrease (Eqs. (27a) and (27b)).

Overall, anticancer therapy slowed the progression of the combined parameter representing cardiac damage, Ξ_{comb}, such that after six months it did not reach the threshold associated with heart failure, even for the case of LC aggregation within the myocardium (Fig. 12). For $q_{LC}=10^5$ LC molecules per plasma cell per second, the corresponding biological age after six months was 77 years—well below the threshold of 100 years associated with patient death (Fig. S35). Thus, although anticancer therapy substantially mitigates cardiac damage by reducing plasma cell clone numbers, residual damage from LC aggregation remains significant, albeit markedly less than in the absence of therapy.

4. Discussion, limitations of the model, and future directions

AL amyloidosis is a progressive and dynamic disease (Eisele et al. 2015) characterized by the expansion of clonal plasma cell populations, production of folded LC monomers by these cells, conversion of folded LCs into unfolded aggregation-prone monomers, aggregation of unfolded monomers into oligomers, and subsequent deposition of oligomers into amyloid fibrils. Depending on the site of aggregation, either unfolded LC monomers or LC fibrils infiltrate the cardiac tissue, contributing to increased myocardial stiffness. In addition, LC oligomers are considered the primary mediators of cardiotoxicity. Consequently, two pathological processes act concurrently to damage the heart: structural stiffening due to LC fibril infiltration and direct cardiotoxicity induced by LC oligomers.

Given the rapid progression of AL amyloidosis, early diagnosis is critical (Palladini et al. 2020), underscoring the importance of understanding the disease's underlying dynamic processes.

The model predicts that LC aggregation is a highly nonlinear process; oligomer concentrations remain very low during the first three months of the six-month disease progression, after which they increase exponentially. This behavior can be explained by the kinetics of oligomer formation: initially, oligomer production is governed by nucleation, a relatively slow process. Once a sufficient concentration of oligomers has formed, they begin to catalyze their own production, leading to a rapid rise in oligomer concentration during the latter three months due to autocatalysis, which proceeds much faster than nucleation.

The model indicates that when LC aggregation occurs within the cardiac tissue, the resulting fraction of the myocardium occupied by LC fibrils is approximately 25 times greater than in the scenario where aggregation occurs in the blood plasma. This outcome can be attributed to the higher oligomer concentration in the cardiac tissue compared to the plasma when aggregation takes place in the heart. The difference arises because the volume of the heart is roughly five times smaller than that of the blood plasma. Given that oligomer formation is an autocatalytic process, higher oligomer concentrations accelerate the reaction, resulting in markedly faster fibril accumulation within the cardiac tissue. For the same reason, the criterion representing accumulated cardiotoxicity induced by LC oligomers is approximately fivefold higher in the scenario where LC aggregation occurs within the cardiac tissue compared to when it occurs in the blood plasma.

A criterion is proposed to quantify the combined cardiac damage resulting from oligomer-induced cardiotoxicity and myocardial stiffening. This criterion attains values approximately tenfold higher when LC aggregation occurs within the cardiac tissue compared with aggregation in the blood plasma. It is further proposed that this criterion may be used as a measure of biological age.

An interesting phenomenon found during this study is the independence of Ξ_{comb} of $\theta_{1/2,B}$ for the scenario when LC aggregation occurs in blood plasma. To elucidate this phenomenon, the behaviors of its two constituent components of Ξ_{comb} were analyzed. The cardiotoxicity component Ξ increases with $\theta_{1/2,B}$ because longer oligomer residence times elevate their concentrations and toxicity, whereas the myocardial volume fraction occupied by fibrils $V_{fibrils} / V_{heart}$, which characterizes cardiac stiffening, decreases as oligomers convert into fibrils more slowly. These opposing effects nearly cancel each other, making the combined cardiac damage criterion Ξ_{comb} effectively independent of $\theta_{1/2,B}$.

The scenario involving anticancer therapy markedly slowed the increase of the combined parameter representing cardiac damage Ξ_{comb}. However, Ξ_{comb} remains appreciable—though substantially reduced compared with the untreated case—indicating that treatment should be initiated as early as possible to minimize residual cardiac injury resulting from LC aggregation.

The findings presented in this study may contribute to the development of novel biomarkers enabling the early diagnosis of AL amyloidosis.

One limitation of this study is that AL amyloidosis exhibits substantial heterogeneity, as each patient possesses a unique pathogenic LC. This limitation could be addressed by tailoring model parameters governing LC aggregation propensity to individual patients or by simulating distinct LC variants.

Author Contribution Statement

AVK is the sole author of this paper.

Funding Declaration

The support for this research was provided by the National Science Foundation (grant DMS-2451660) and the Alexander von Humboldt Foundation through the Humboldt Research Award.

Clinical trial number: not applicable

Ethics Statement: not applicable

References

Absmeier RM, Rottenaicher GJ, Svilenov HL, et al (2023) Antibodies gone bad – the molecular mechanism of light chain amyloidosis. The FEBS Journal 290:1398–1419. https://doi.org/10.1111/febs.16390

Ananda Rao A, Johncy S (2022) Tennis Courts in the Human Body: A Review of the Misleading Metaphor in Medical Literature. Cureus 14:e21474. https://doi.org/10.7759/cureus.21474

Aragonès Pedrola J, Dekker FA, Garfagnini T, et al (2025) FibrilPaint to determine the length of Tau amyloids in fluids. Proceedings of the National Academy of Sciences 122:e2502847122. https://doi.org/10.1073/pnas.2502847122

Ayati BP, Edwards CM, Webb GF, Wikswo JP (2010) A mathematical model of bone remodeling dynamics for normal bone cell populations and myeloma bone disease. Biol Direct 5:28. https://doi.org/10.1186/1745-6150-5-28

Bain B (2011) CHAPTER 5 - Pathology of the marrow: General considerations and infections/reactive conditions. In: Porwit A, McCullough J, Erber WN (eds) Blood and Bone Marrow Pathology (Second Edition). Churchill Livingstone, Edinburgh, pp 79–102

Baker KR (2022) Light Chain Amyloidosis: Epidemiology, Staging, and Prognostication. Methodist Debakey Cardiovasc J 18:27–35. https://doi.org/10.14797/mdcvj.1070

Banypersad SM, Moon JC, Whelan C, et al (2012) Updates in Cardiac Amyloidosis: A Review. Journal of the American Heart Association 1:e000364. https://doi.org/10.1161/JAHA.111.000364

Basnayake K, Stringer SJ, Hutchison CA, Cockwell P (2011) The biology of immunoglobulin free light chains and kidney injury. Kidney International 79:1289–1301. https://doi.org/10.1038/ki.2011.94

Beck JV, Arnold KJ (1977) Parameter Estimation in Science and Engineering. Wiley, New York

Betts JG (2013) Anatomy and Physiology. OpenStax College, Rice University

Blancas-Mejía LM, Horn TJ, Marin-Argany M, et al (2015) Thermodynamic and fibril formation studies of full length immunoglobulin light chain AL-09 and its germline protein using scan rate dependent thermal unfolding. Biophys Chem 207:13–20. https://doi.org/10.1016/j.bpc.2015.07.005

Blancas-Mejía LM, Ramirez-Alvarado M (2013) Systemic amyloidoses. Annu Rev Biochem 82:745–774. https://doi.org/10.1146/annurev-biochem-072611-130030

Boltachev GS, Ivanov MG (2020) Effect of nanoparticle concentration on coagulation rate of colloidal suspensions. Heliyon 6:e03295. https://doi.org/10.1016/j.heliyon.2020.e03295

Cavicchi RE, King J, Ripple DC (2018) Measurement of Average Aggregate Density by Sedimentation and Brownian Motion Analysis. Journal of pharmaceutical sciences 107:1304–1312. https://doi.org/10.1016/j.xphs.2018.01.013

Cohen SIA, Linse S, Luheshi LM, et al (2013) Proliferation of amyloid-β42 aggregates occurs through a secondary nucleation mechanism. Proceedings of the National Academy of Sciences of the United States of America 110:9758–9763. https://doi.org/10.1073/pnas.1218402110

Dispenzieri A, Gertz MA, Kyle RA, et al (2004) Prognostication of survival using cardiac troponins and N-terminal pro-brain natriuretic peptide in patients with primary systemic amyloidosis undergoing peripheral blood stem cell transplantation. Blood 104:1881–1887. https://doi.org/10.1182/blood-2004-01-0390

Dispenzieri A, Kyle RA, Gertz MA, et al (2003) Survival in patients with primary systemic amyloidosis and raised serum cardiac troponins. The Lancet 361:1787–1789. https://doi.org/10.1016/S0140-6736(03)13396-X

Dormann D, Lemke EA (2024) Adding intrinsically disordered proteins to biological ageing clocks. Nature Cell Biology 26:851–858. https://doi.org/10.1038/s41556-024-01423-w

Dubrey SW, Cha K, Anderson J, et al (1998) The clinical features of immunoglobulin light-chain (AL) amyloidosis with heart involvement. QJM 91:141–157. https://doi.org/10.1093/qjmed/91.2.141

Eisele YS, Monteiro C, Fearns C, et al (2015) Targeting protein aggregation for the treatment of degenerative diseases. Nature Reviews Drug Discovery 14:759–780. https://doi.org/10.1038/nrd4593

Falk RH, Alexander KM, Liao R, Dorbala S (2016) AL (Light-Chain) Cardiac Amyloidosis: A Review of Diagnosis and Therapy. Journal of the American College of Cardiology 68:1323–1341. https://doi.org/10.1016/j.jacc.2016.06.053

Finke RG, Watzky MA, Whitehead CB (2020) Response to "Particle Size Is a Primary Determinant for Sigmoidal Kinetics of Nanoparticle Formation: A 'Disproof' of the Finke–Watzky (F-W) Nanoparticle Nucleation and Growth Mechanism." Chemistry of Materials 32:3657–3672. https://doi.org/10.1021/acs.chemmater.0c00780

Fitzgerald BT, Bashford J, Scalia GM (2013) The Return of the Normal Heart: Resolution of Cardiac Amyloidosis After Chemotherapy and Bone Marrow Transplantation. Heart, Lung and Circulation 22:655–660. https://doi.org/10.1016/j.hlc.2013.01.013

Gallaher J, Larripa K, Renardy M, et al (2018) Methods for determining key components in a mathematical model for tumor-immune dynamics in multiple myeloma. J Theor Biol 458:31–46. https://doi.org/10.1016/j.jtbi.2018.08.037

Goldis R, Kaplan B, Arad M, et al (2024) Amino acid sequence homology of monoclonal serum free light chain dimers and tissue deposited light chains in AL amyloidosis: a pilot study. Clin Chem Lab Med 62:464–471. https://doi.org/10.1515/cclm-2023-0591

Hassan W, Al-Sergani H, Mourad W, Tabbaa R (2005) Amyloid heart disease. New frontiers and insights in pathophysiology, diagnosis, and management. Tex Heart Inst J 32:178–184

Hutchison CA, Plant T, Drayson M, et al (2008) Serum free light chain measurement aids the diagnosis of myeloma in patients with severe renal failure. BMC Nephrol 9:11. https://doi.org/10.1186/1471-2369-9-11

Iashchishyn IA, Sulskis D, Ngoc MN, et al (2017) Finke-Watzky Two-Step Nucleation-Autocatalysis Model of S100A9 Amyloid Formation: Protein Misfolding as "Nucleation" Event. ACS chemical neuroscience 8:2152–2158. https://doi.org/10.1021/acschemneuro.7b00251

Ikura H, Endo J, Kitakata H, et al (2022) Molecular Mechanism of Pathogenesis and Treatment Strategies for AL Amyloidosis. Int J Mol Sci 23:. https://doi.org/10.3390/ijms23116336

Kastritis Efstathios, Palladini Giovanni, Minnema Monique C., et al (2021) Daratumumab-Based Treatment for Immunoglobulin Light-Chain Amyloidosis. New England Journal of Medicine 385:46–58. https://doi.org/10.1056/NEJMoa2028631

Katzmann JA, Clark RJ, Abraham RS, et al (2002) Serum Reference Intervals and Diagnostic Ranges for Free κ and Free λ Immunoglobulin Light Chains: Relative Sensitivity for Detection of Monoclonal Light Chains. Clinical Chemistry 48:1437–1444. https://doi.org/10.1093/clinchem/48.9.1437

Kazman P, Absmeier RM, Engelhardt H, Buchner J (2021) Dissection of the amyloid formation pathway in AL amyloidosis. Nature Communications 12:6516. https://doi.org/10.1038/s41467-021-26845-0

Knowles TPJ, Waudby CA, Devlin GL, et al (2009) An Analytical Solution to the Kinetics of Breakable Filament Assembly. Science 326:1533–1537. https://doi.org/10.1126/science.1178250

Kumar S, Dispenzieri A, Lacy MQ, et al (2012) Revised prognostic staging system for light chain amyloidosis incorporating cardiac biomarkers and serum free light chain measurements. J Clin Oncol 30:989–995. https://doi.org/10.1200/JCO.2011.38.5724

Kuznetsov AV (2025a) Does Human Transthyretin Aggregate in Blood Plasma or in Cardiac Tissue? A Mathematical Modeling Study. bioRxiv 2025.07.29.667417. https://doi.org/10.1101/2025.07.29.667417

Kuznetsov AV (2025b) Modeling the growth of cytosolic TDP-43 inclusion bodies and accumulated neurotoxicity of misfolded oligomers in neurons. bioRxiv 2023.11.28.569118. https://doi.org/10.1101/2023.11.28.569118

Kuznetsov AV (2025c) A criterion characterizing accumulated neurotoxicity of Aβ oligomers in Alzheimer's disease. Proceedings of the Royal Society A 481:20240652. https://doi.org/10.1098/rspa.2024.0652

Kuznetsov AV (2025d) Criterion for assessing accumulated neurotoxicity of alpha-synuclein oligomers in Parkinson's disease. International Journal for Numerical Methods in Biomedical Engineering 41:e70027. https://doi.org/doi.org/10.1002/cnm.70027

Kuznetsov IA, Kuznetsov AV (2019) Investigating sensitivity coefficients characterizing the response of a model of tau protein transport in an axon to model parameters. Computer methods in biomechanics and biomedical engineering 22:71–83. https://doi.org/10.1080/10255842.2018.1534233

Li SZ, Jain A (eds) (2009) Capillary Blood Vessel. In: Encyclopedia of Biometrics. Springer US, Boston, MA, pp 178–178

Lu R, Richards TA (2019) AL Amyloidosis: Unfolding a Complex Disease. J Adv Pract Oncol 10:813–825. https://doi.org/10.6004/jadpro.2019.10.8.4

Maceira AM, Joshi J, Prasad SK, et al (2005) Cardiovascular Magnetic Resonance in Cardiac Amyloidosis. Circulation 111:186–193. https://doi.org/10.1161/01.CIR.0000152819.97857.9D

Martinez-Rivas G, Bender S, Sirac C (2022) Understanding AL amyloidosis with a little help from in vivo models. Frontiers in Immunology Volume 13-2022:

Morgan GJ, Yan NL, Mortenson DE, et al (2019) Stabilization of amyloidogenic immunoglobulin light chains by small molecules. Proceedings of the National Academy of Sciences 116:8360–8369. https://doi.org/10.1073/pnas.1817567116

Morris AM, Watzky MA, Agar JN, Finke RG (2008) Fitting neurological protein aggregation kinetic data via a 2-step, Minimal/"Ockham's Razor" model: The Finke-Watzky mechanism of nucleation followed by autocatalytic surface growth. Biochemistry 47:2413–2427. https://doi.org/10.1021/bi701899y

Murphy H, Jaafari H, Dobrovolny HM (2016) Differences in predictions of ODE models of tumor growth: a cautionary example. BMC Cancer 16:163. https://doi.org/10.1186/s12885-016-2164-x

Palladini G, Merlini G (2016) What is new in diagnosis and management of light chain amyloidosis? Blood 128:159–168. https://doi.org/10.1182/blood-2016-01-629790

Palladini G, Milani P, Merlini G (2020) Management of AL amyloidosis in 2020. Blood 136:2620–2627. https://doi.org/10.1182/blood.2020006913

Pradhan T, Sarkar R, Meighen-Berger KM, et al (2023) Mechanistic insights into the aggregation pathway of the patient-derived immunoglobulin light chain variable domain protein FOR005. Nature Communications 14:3755. https://doi.org/10.1038/s41467-023-39280-0

Ribba B, Holford NH, Magni P, et al (2014) A review of mixed-effects models of tumor growth and effects of anticancer drug treatment used in population analysis. CPT Pharmacometrics Syst Pharmacol 3:e113. https://doi.org/10.1038/psp.2014.12

Rinauro DJ, Chiti F, Vendruscolo M, Limbocker R (2024) Misfolded protein oligomers: mechanisms of formation, cytotoxic effects, and pharmacological approaches against protein misfolding diseases. Molecular Neurodegeneration 19:20. https://doi.org/10.1186/s13024-023-00651-2

Rognoni P, Mazzini G, Caminito S, et al (2021) Dissecting the Molecular Features of Systemic Light Chain (AL) Amyloidosis: Contributions from Proteomics. Medicina (Kaunas) 57:. https://doi.org/10.3390/medicina57090916

Sanders PW (2012) Mechanisms of Light Chain Injury along the Tubular Nephron. Journal of the American Society of Nephrology 23:

Saunders B, Theodorakakou F, Fotiou D, et al (2025) Predictive value of free light chain burden in patients with AL amyloidosis treated with bortezomib-based regimens. Blood Advances 9:3771–3779. https://doi.org/10.1182/bloodadvances.2024015528

Sender R, Weiss Y, Navon Y, et al (2023) The total mass, number, and distribution of immune cells in the human body. Proceedings of the National Academy of Sciences 120:e2308511120. https://doi.org/10.1073/pnas.2308511120

Sharma R, Sharma S (2025) Physiology, Blood Volume. In: StatPearls. StatPearls Publishing, Treasure Island (FL)

Sullivan PW, Salmon SE (1972) Kinetics of tumor growth and regression in IgG multiple myeloma. J Clin Invest 51:1697–1708. https://doi.org/10.1172/JCI106971

Tahir UA, Doros G, Kim JS, et al (2019) Predictors of Mortality in Light Chain Cardiac Amyloidosis with Heart Failure. Sci Rep 9:8552. https://doi.org/10.1038/s41598-019-44912-x

Tosi P, Tomassetti S, Merli A, Polli V (2013) Serum free light-chain assay for the detection and monitoring of multiple myeloma and related conditions. Ther Adv Hematol 4:37–41. https://doi.org/10.1177/2040620712466863

Usher JR (1994) Some mathematical models for cancer chemotherapy. Computers & Mathematics with Applications 28:73–80. https://doi.org/10.1016/0898-1221(94)00179-0

Vaghi C, Rodallec A, Fanciullino R, et al (2020) Population modeling of tumor growth curves and the reduced Gompertz model improve prediction of the age of experimental tumors. PLoS Comput Biol 16:e1007178. https://doi.org/10.1371/journal.pcbi.1007178

van Gameren II, van Rijswijk MH, Bijzet J, et al (2009) Histological regression of amyloid in AL amyloidosis is exclusively seen after normalization of serum free light chain. Haematologica 94:1094–1100. https://doi.org/10.3324/haematol.2008.004119

Watzky MA, Finke RG (1997) Transition Metal Nanocluster Formation Kinetic and Mechanistic Studies. A New Mechanism When Hydrogen Is the Reductant: Slow, Continuous Nucleation and Fast Autocatalytic Surface Growth. Journal of the American Chemical Society 119:10382–10400. https://doi.org/10.1021/ja9705102

Watzky MA, Finney EE, Finke RG (2008) Transition-Metal Nanocluster Size vs Formation Time and the Catalytically Effective Nucleus Number: A Mechanism-Based Treatment. Journal of the American Chemical Society 130:11959–11969. https://doi.org/10.1021/ja8017412

Witteles RM, Liedtke M (2019) AL Amyloidosis for the Cardiologist and Oncologist: Epidemiology, Diagnosis, and Management. JACC: CardioOncology 1:117–130. https://doi.org/10.1016/j.jaccao.2019.08.002

Zadeh KS, Montas HJ (2010) A class of exact solutions for biomacromolecule diffusion-reaction in live cells. Journal of theoretical biology 264:914–933. https://doi.org/10.1016/j.jtbi.2010.03.028

Zi Z (2011) Sensitivity analysis approaches applied to systems biology models. Iet Systems Biology 5:336–346. https://doi.org/10.1049/iet-syb.2011.0015

Figure captions

Fig. 1. Block diagrams illustrating pathological processes occurring in the bone marrow, blood plasma, and cardiac tissue. (a) Scenario in which aggregation of Ig LCs takes place in the blood plasma. In this case, LC unfolding, oligomer formation through nucleation and autocatalytic mechanisms, and subsequent deposition of oligomers into amyloid protofibrils all occur within the plasma. Circulating fibrils are then deposited in the cardiac tissue. (b) Scenario in which aggregation of Ig LCs occurs within the cardiac tissue. In this case, LCs unfold in the blood plasma, and the unfolded LCs subsequently deposit into the cardiac tissue. Within the tissue, the unfolded LCs form oligomers via nucleation and autocatalytic growth, which then assemble into amyloid fibrils.

Fig. 2. Time-dependent criterion characterizing the combined effect of cytotoxicity and myocardial stiffening, Ξ_{comb}, vs time, *t*, for two scenarios: (a) aggregation occurring in the blood plasma and (b) aggregation occurring within the cardiac tissue. Results are presented for three different values of the secretion rate of folded LCs produced by a single plasma cell belonging to a clonal population, q_{LC}. $k_1 = 10^{-6}$ s^{-1}, $k_2 = 10^{-6}$ μM^{-1} s^{-1}, $k_u = 4\times10^{-4}$ s^{-1}, $\theta_{1/2,B} = 10^7$ s, and $\theta_{1/2,I} = 10^7$ s. The case without anticancer therapy.

Fig. 3. Time-dependent criterion characterizing the combined effect of cytotoxicity and myocardial stiffening, Ξ_{comb}, vs time, *t*, for two scenarios: (a) aggregation occurring in the blood plasma and (b) aggregation occurring within the cardiac tissue. Results are shown for three different values of the rate of unfolding of LCs, k_u. $k_1 = 10^{-6}$ s^{-1}, $k_2 = 10^{-6}$ μM^{-1} s^{-1}, $q_{LC} = 10^5 \ \frac{\text{LC molecules}}{\text{cell s}}$, $\theta_{1/2,B} = 10^7$ s, and $\theta_{1/2,I} = 10^7$ s. The case without anticancer therapy.

Fig. 4. Criterion characterizing the combined effect of cytotoxicity and myocardial stiffening, Ξ_{comb}, vs the secretion rate of folded LCs produced by a single plasma cell belonging to a clonal population, q_{LC}, after six months of the disease for two scenarios: (a) aggregation occurring in the blood plasma and (b) aggregation occurring within the cardiac tissue. Results are shown for three different values of the rate of unfolding of LCs, k_u. $k_1 = 10^{-6}$ s^{-1}, $k_2 = 10^{-6}$ μM^{-1} s^{-1}, $\theta_{1/2,B} = 10^7$ s, and $\theta_{1/2,I} = 10^7$ s. The case without anticancer therapy.

Fig. 5. Time-dependent criterion characterizing the combined effect of cytotoxicity and myocardial stiffening, Ξ_{comb}, vs time, *t*, for two scenarios: (a) aggregation occurring in the blood plasma and (b) aggregation occurring within the cardiac tissue. Results are shown for three different values of the half-

deposition time for free LC oligomers to be incorporated into LC fibrils, $\theta_{1/2,B}$. Computations were performed for $q_{LC} = 10^5$ LC molecules per plasma cell per second. $k_1 = 10^{-6}$ s^{-1}, $k_2 = 10^{-6}$ μM^{-1} s^{-1}, $k_u = 4\times10^{-4}$ s^{-1}, $q_{LC} = 10^5 \ \frac{\text{LC molecules}}{\text{cell s}}$, and $\theta_{1/2,I} = 10^7$ s. The case without anticancer therapy.

Fig. 6. Time-dependent criterion characterizing the combined effect of cytotoxicity and myocardial stiffening, Ξ_{comb}, vs the half-deposition time for free LC oligomers to be incorporated into LC fibrils, $\theta_{1/2,B}$, for two scenarios: (a) aggregation occurring in the blood plasma and (b) aggregation occurring within the cardiac tissue. Results are presented for three different values of the secretion rate of folded LCs produced by a single plasma cell belonging to a clonal population, q_{LC}. $k_1 = 10^{-6}$ s^{-1}, $k_2 = 10^{-6}$ μM^{-1} s^{-1}, $k_u = 4\times10^{-4}$ s^{-1}, and $\theta_{1/2,I} = 10^7$ s. The case without anticancer therapy.

Fig. 7. Time-dependent criterion for accumulated cardiotoxicity induced by LC oligomers, Ξ, vs time, *t*, for two scenarios: (a) aggregation occurring in the blood plasma and (b) aggregation occurring within the cardiac tissue. Results are shown for three different values of the half-deposition time for free LC oligomers to be incorporated into LC fibrils, $\theta_{1/2,B}$. $k_1 = 10^{-6}$ s^{-1}, $k_2 = 10^{-6}$ μM^{-1} s^{-1}, $k_u = 4\times10^{-4}$ s^{-1}, $q_{LC} = 10^5 \ \frac{\text{LC molecules}}{\text{cell s}}$, and $\theta_{1/2,I} = 10^7$ s. The case without anticancer therapy.

Fig. 8. (a) Molar concentration of free LC oligomers in blood plasma, $[B]_{plasma}$, vs time, *t*, when aggregation occurs in the plasma, and (b) molar concentration of free LC oligomers in cardiac tissue, $[B]_{tissue}$, vs time when aggregation occurs within the tissue. Results are shown for three different values of the half-deposition time for free LC oligomers to be incorporated into LC fibrils, $\theta_{1/2,B}$. $k_1 = 10^{-6}$ s^{-1}, $k_2 = 10^{-6}$ μM^{-1} s^{-1}, $k_u = 4\times10^{-4}$ s^{-1}, $q_{LC} = 10^5 \ \frac{\text{LC molecules}}{\text{cell s}}$, and $\theta_{1/2,I} = 10^7$ s. The case without anticancer therapy.

Fig. 9. Fraction of myocardial volume occupied by LC fibrils, $V_{fibrils} / V_{heart}$, vs time, *t*, for two scenarios: (a) aggregation occurring in the blood plasma and (b) aggregation occurring within the cardiac tissue. Results are shown for three different values of the half-deposition time for free LC oligomers to be incorporated into LC fibrils, $\theta_{1/2,B}$. $k_1 = 10^{-6}$ s^{-1}, $k_2 = 10^{-6}$ μM^{-1} s^{-1}, $k_u = 4\times10^{-4}$ s^{-1}, $q_{LC} = 10^5 \ \frac{\text{LC molecules}}{\text{cell s}}$, and $\theta_{1/2,I} = 10^7$ s. The case without anticancer therapy.

Fig. 10. Molar concentration of LC oligomers incorporated into amyloid fibrils infiltrating the cardiac tissue, $[I]_{tissue}$, vs time, *t*, for two scenarios: (a) aggregation occurring in the blood plasma and (b) aggregation occurring within the cardiac tissue. Results are shown for three different values of the half-deposition time for free LC oligomers to be incorporated into LC fibrils, $\theta_{1/2,B}$. $k_1 = 10^{-6}$ s^{-1}, $k_2 = 10^{-6}$ μM^{-1} s^{-1}, $k_u = 4\times10^{-4}$ s^{-1}, $q_{LC} = 10^5 \ \frac{\text{LC molecules}}{\text{cell s}}$, and $\theta_{1/2,I} = 10^7$ s. The case without anticancer therapy.

Fig. 11. Dimensionless sensitivity of the criterion characterizing the combined effects of cytotoxicity and myocardial stiffening to the half-deposition time for free LC oligomers to be incorporated into LC fibrils, $S_{\theta_{1/2,B}}^{\Xi_{comb}}$, vs $\theta_{1/2,B}$. Results are presented for three different values of the secretion rate of folded LCs produced by a single plasma cell belonging to a clonal population, q_{LC}. $k_1 = 10^{-6}$ s^{-1}, $k_2 = 10^{-6}$ μM^{-1} s^{-1}, $k_u = 4\times10^{-4}$ s^{-1}, and $\theta_{1/2,I} = 10^7$ s. The case without anticancer therapy.

Fig. 12. Time-dependent criterion characterizing combined effect of cytotoxicity and myocardial stiffening, Ξ_{comb}, vs time, *t*, for two scenarios: (a) aggregation occurring in the blood plasma and (b) aggregation occurring within the cardiac tissue. Results are presented for three different values of the secretion rate of folded LCs produced by a single plasma cell belonging to a clonal population, q_{LC}. $k_1 = 10^{-6}$ s^{-1}, $k_2 = 10^{-6}$ μM^{-1} s^{-1}, $k_u = 4\times10^{-4}$ s^{-1}, $\theta_{1/2,B} = 10^7$ s, and $\theta_{1/2,I} = 10^7$ s. The case with anticancer therapy.

(a) Aggregation in blood plasma

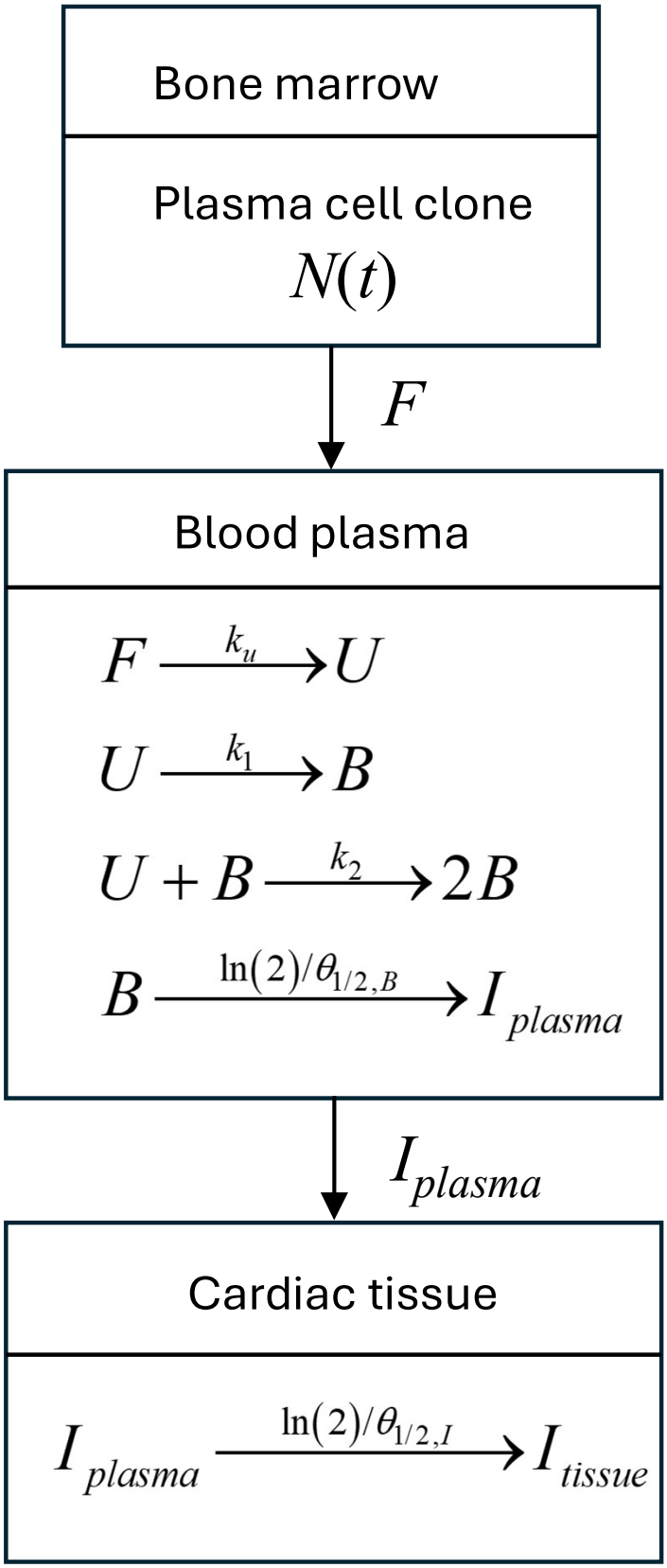

Fig. 1a

(b) Aggregation in cardiac tissue

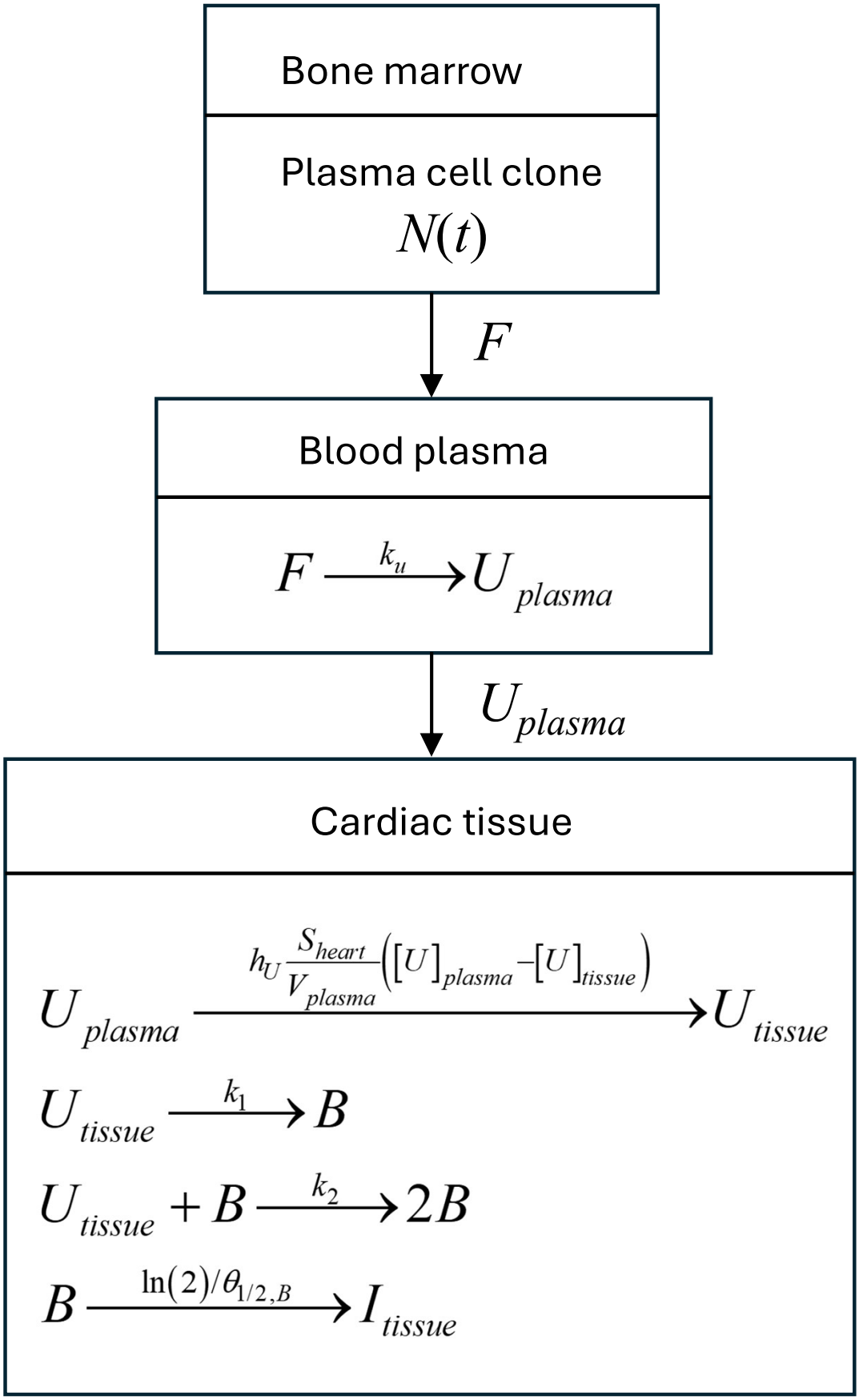

Fig. 1b

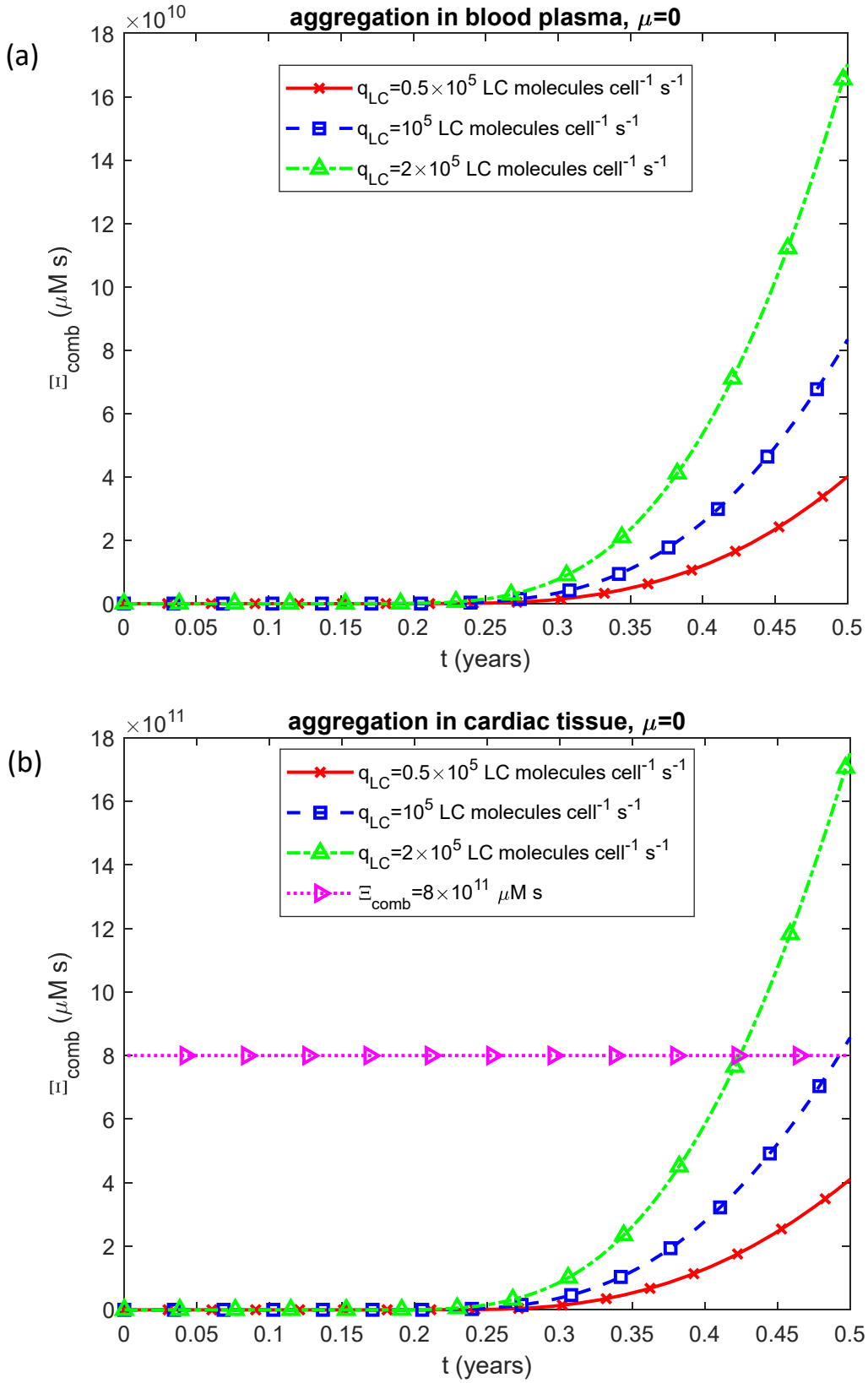
(a)
aggregation in blood plasma, μ=0
×10^10
q_LC=0.5×10^5 LC molecules cell^-1 s^-1
q_LC=10^5 LC molecules cell^-1 s^-1
q_LC=2×10^5 LC molecules cell^-1 s^-1
Ξ_comb (μM s)
t (years)
(b)
aggregation in cardiac tissue, μ=0
×10^11
q_LC=0.5×10^5 LC molecules cell^-1 s^-1
q_LC=10^5 LC molecules cell^-1 s^-1
q_LC=2×10^5 LC molecules cell^-1 s^-1
Ξ_comb=8×10^11 μM s
Ξ_comb (μM s)
t (years)

Figure 2

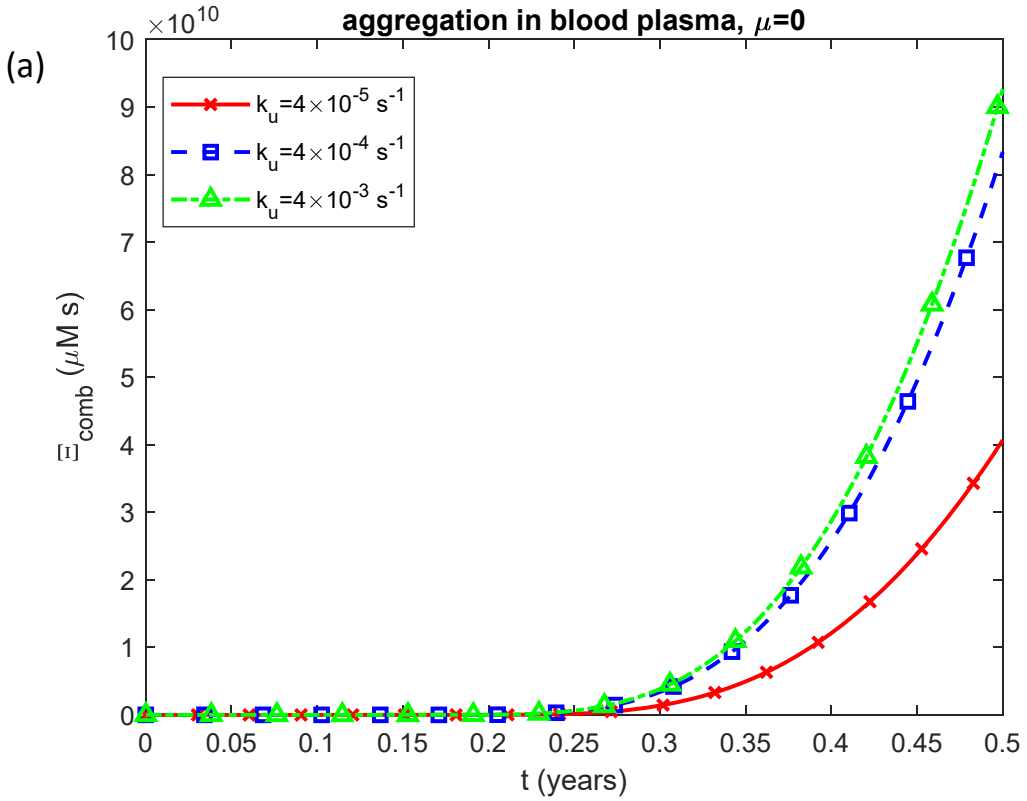
(a)
aggregation in blood plasma, μ=0
×10^10
k_u=4×10^-5 s^-1
k_u=4×10^-4 s^-1
k_u=4×10^-3 s^-1
Ξ_comb (μM s)
t (years)

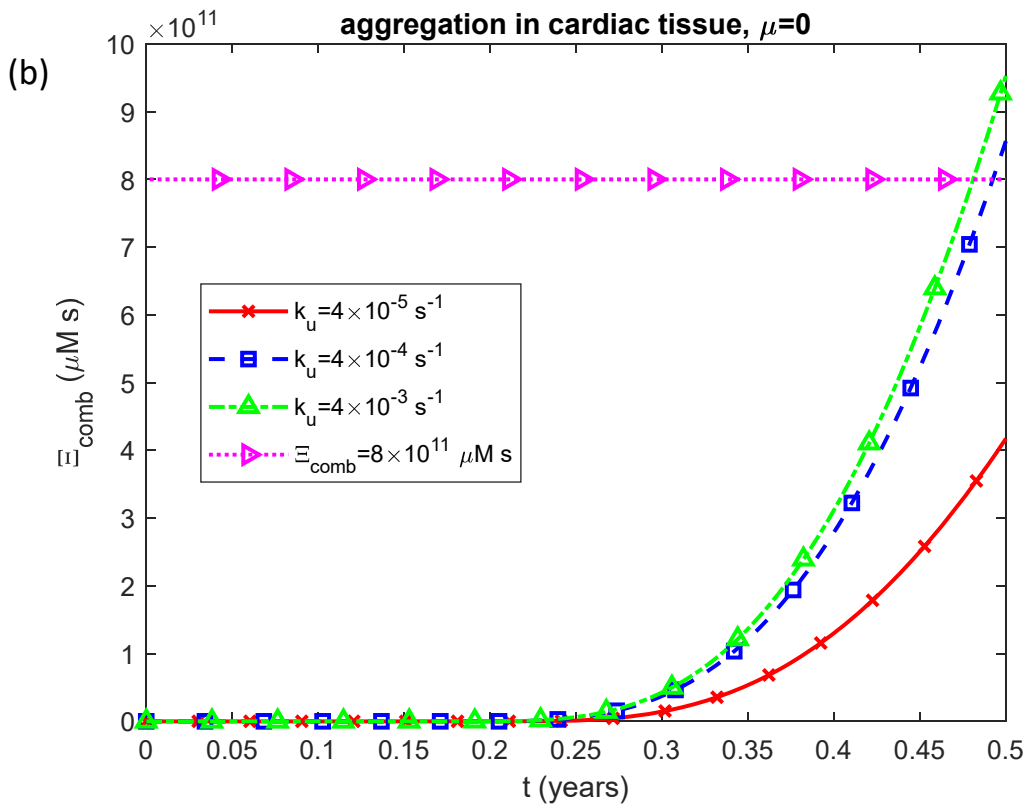
(b)
aggregation in cardiac tissue, μ=0
×10^11
k_u=4×10^-5 s^-1
k_u=4×10^-4 s^-1
k_u=4×10^-3 s^-1
Ξ_comb=8×10^11 μM s
Ξ_comb (μM s)
t (years)

Figure 3

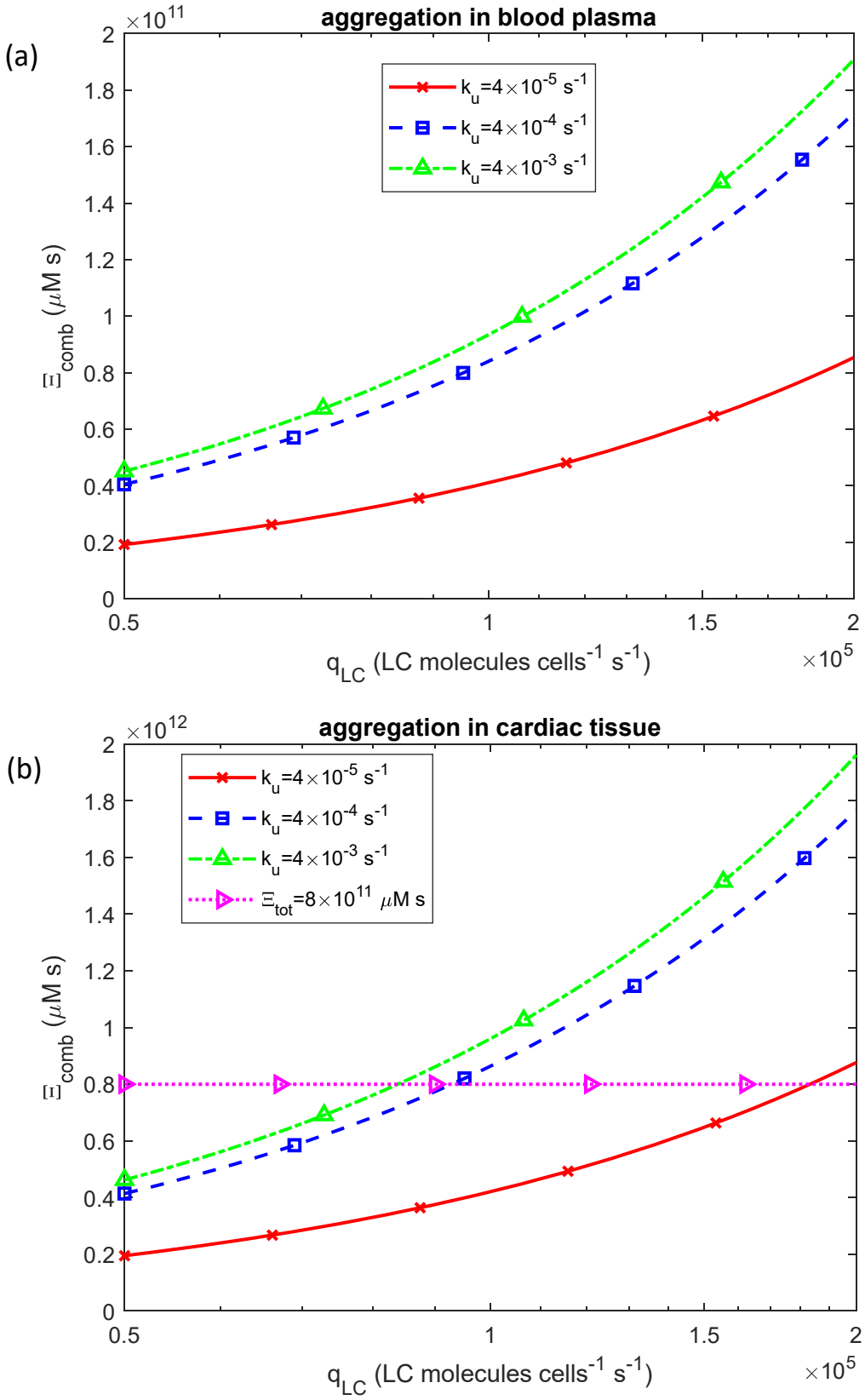
(a)
aggregation in blood plasma
×10^11
2
1.8
1.6
1.4
1.2
1
0.8
0.6
0.4
0.2
0
Ξcomb (μM s)
ku=4×10^-5 s^-1
ku=4×10^-4 s^-1
ku=4×10^-3 s^-1
0.5
1
1.5
2
×10^5
qLC (LC molecules cells^-1 s^-1)
(b)
aggregation in cardiac tissue
×10^12
2
1.8
1.6
1.4
1.2
1
0.8
0.6
0.4
0.2
0
Ξcomb (μM s)
ku=4×10^-5 s^-1
ku=4×10^-4 s^-1
ku=4×10^-3 s^-1
Ξtot=8×10^11 μM s
0.5
1
1.5
2
×10^5
qLC (LC molecules cells^-1 s^-1)

Figure 4

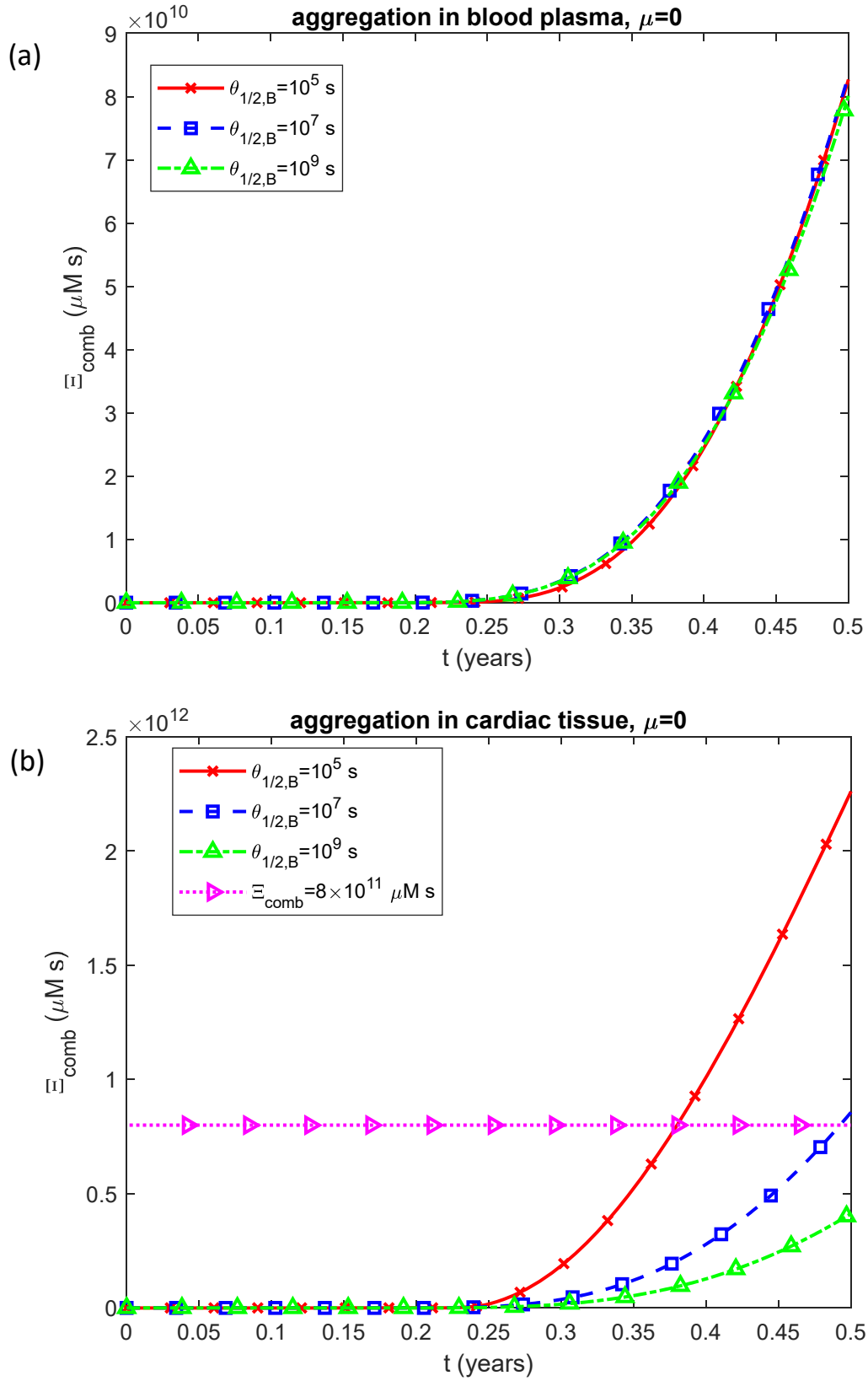
(a)
aggregation in blood plasma, μ=0
$\times 10^{10}$
$\theta_{1/2,B}=10^5$ s
$\theta_{1/2,B}=10^7$ s
$\theta_{1/2,B}=10^9$ s
Ξ_{comb} (μM s)
t (years)
(b)
aggregation in cardiac tissue, μ=0
$\times 10^{12}$
$\theta_{1/2,B}=10^5$ s
$\theta_{1/2,B}=10^7$ s
$\theta_{1/2,B}=10^9$ s
$\Xi_{comb}=8\times 10^{11}$ μM s
Ξ_{comb} (μM s)
t (years)

Figure 5

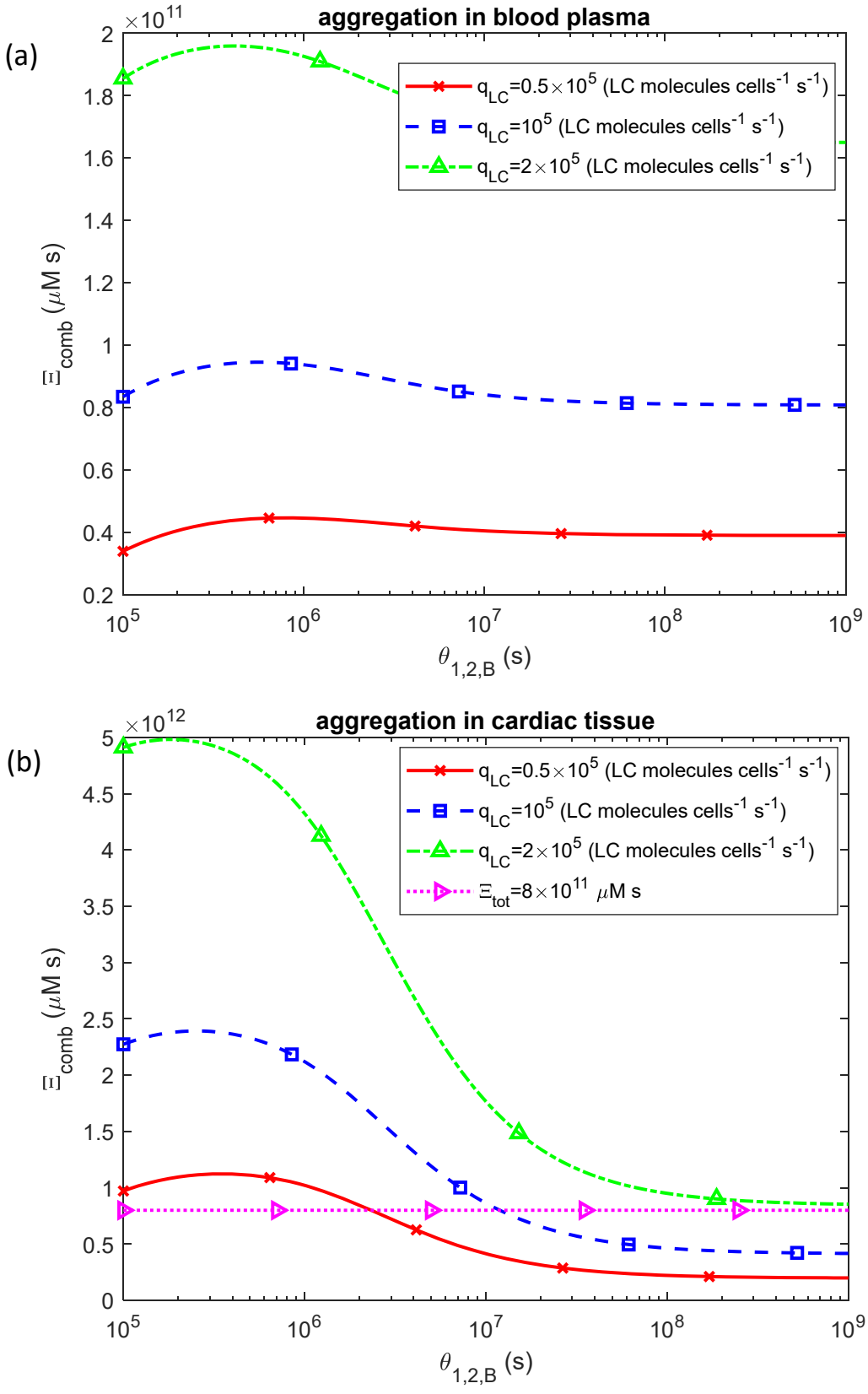
(a)
aggregation in blood plasma
×10^11
2
1.8
1.6
1.4
1.2
1
0.8
0.6
0.4
0.2
Ξcomb (μM s)
10^5
10^6
10^7
10^8
10^9
θ1,2,B (s)
qLC=0.5×10^5 (LC molecules cells^-1 s^-1)
qLC=10^5 (LC molecules cells^-1 s^-1)
qLC=2×10^5 (LC molecules cells^-1 s^-1)
(b)
aggregation in cardiac tissue
×10^12
5
4.5
4
3.5
3
2.5
2
1.5
1
0.5
0
Ξcomb (μM s)
10^5
10^6
10^7
10^8
10^9
θ1,2,B (s)
qLC=0.5×10^5 (LC molecules cells^-1 s^-1)
qLC=10^5 (LC molecules cells^-1 s^-1)
qLC=2×10^5 (LC molecules cells^-1 s^-1)
Ξtot=8×10^11 μM s

Figure 6

(a)

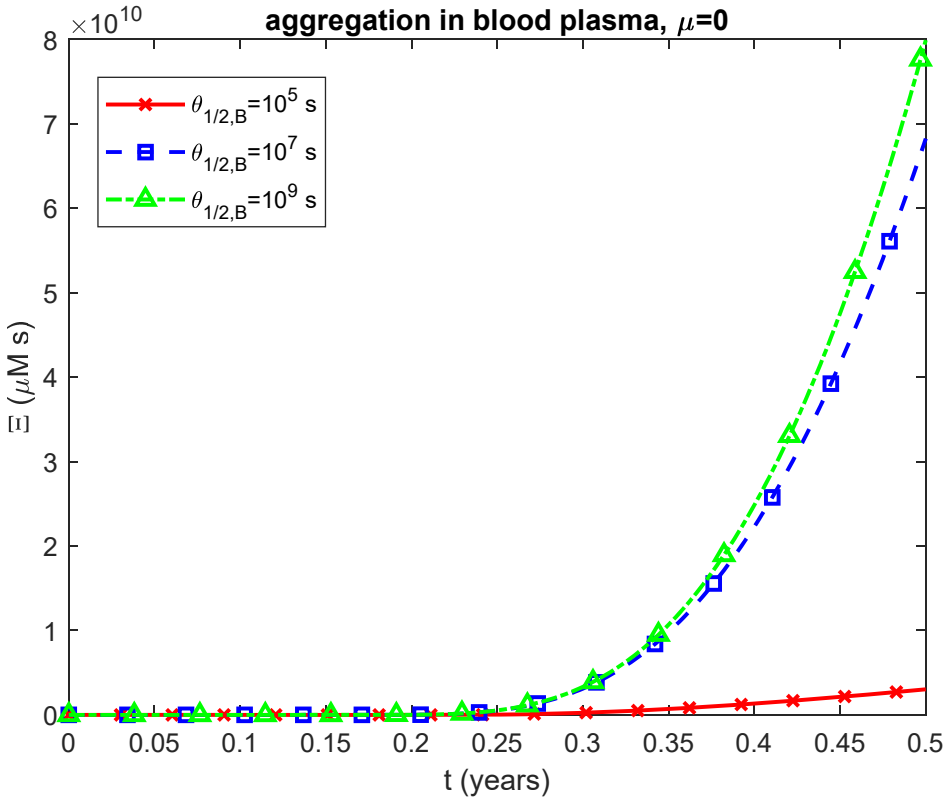
aggregation in blood plasma, μ=0
$\times 10^{10}$
$\theta_{1/2,B}$=10^5 s
$\theta_{1/2,B}$=10^7 s
$\theta_{1/2,B}$=10^9 s
[I] (μM s)
t (years)

(b)

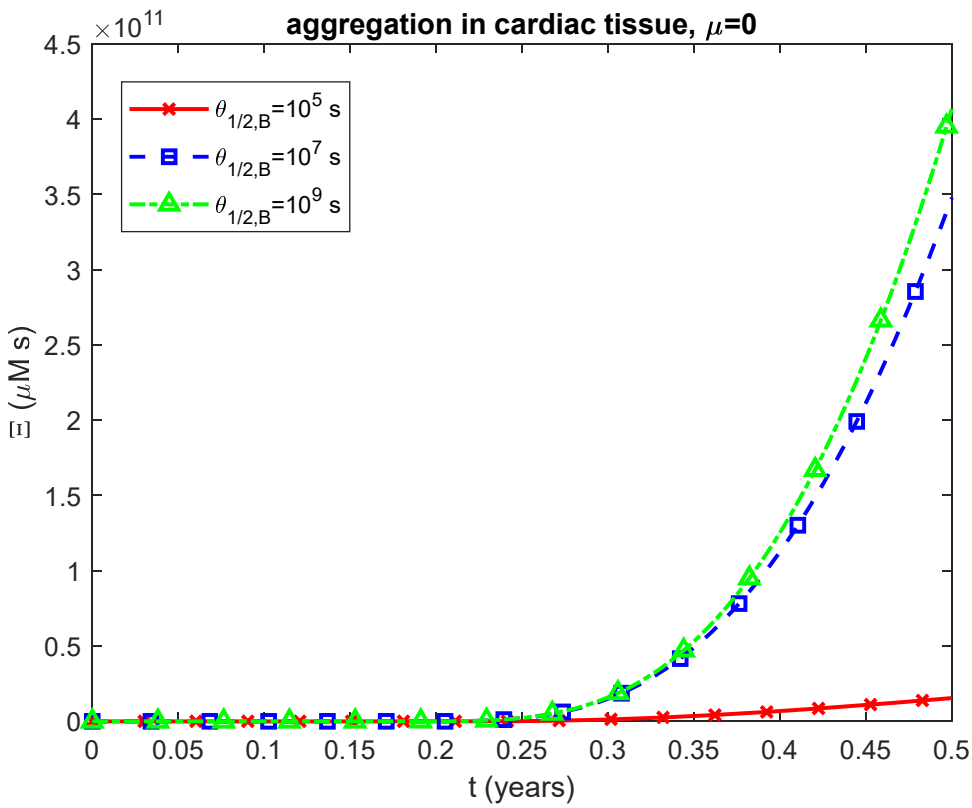
aggregation in cardiac tissue, μ=0
$\times 10^{11}$
$\theta_{1/2,B}$=10^5 s
$\theta_{1/2,B}$=10^7 s
$\theta_{1/2,B}$=10^9 s
[I] (μM s)
t (years)

Figure 7

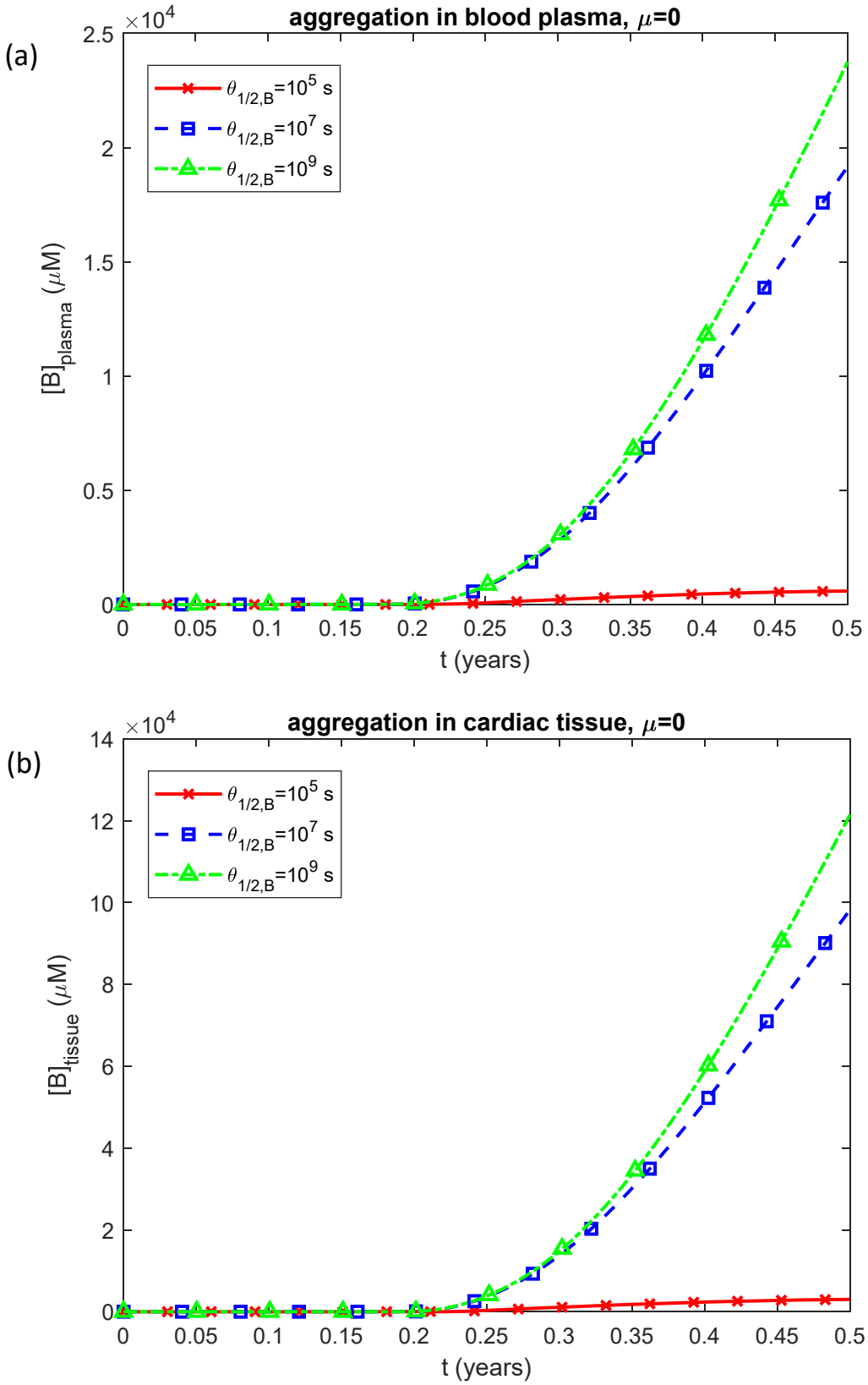
(a)
aggregation in blood plasma, μ=0
$\times 10^4$
$\theta_{1/2,B}=10^5$ s
$\theta_{1/2,B}=10^7$ s
$\theta_{1/2,B}=10^9$ s
$[B]_{plasma}$ (μM)
t (years)
(b)
aggregation in cardiac tissue, μ=0
$\times 10^4$
$\theta_{1/2,B}=10^5$ s
$\theta_{1/2,B}=10^7$ s
$\theta_{1/2,B}=10^9$ s
$[B]_{tissue}$ (μM)
t (years)

Figure 8

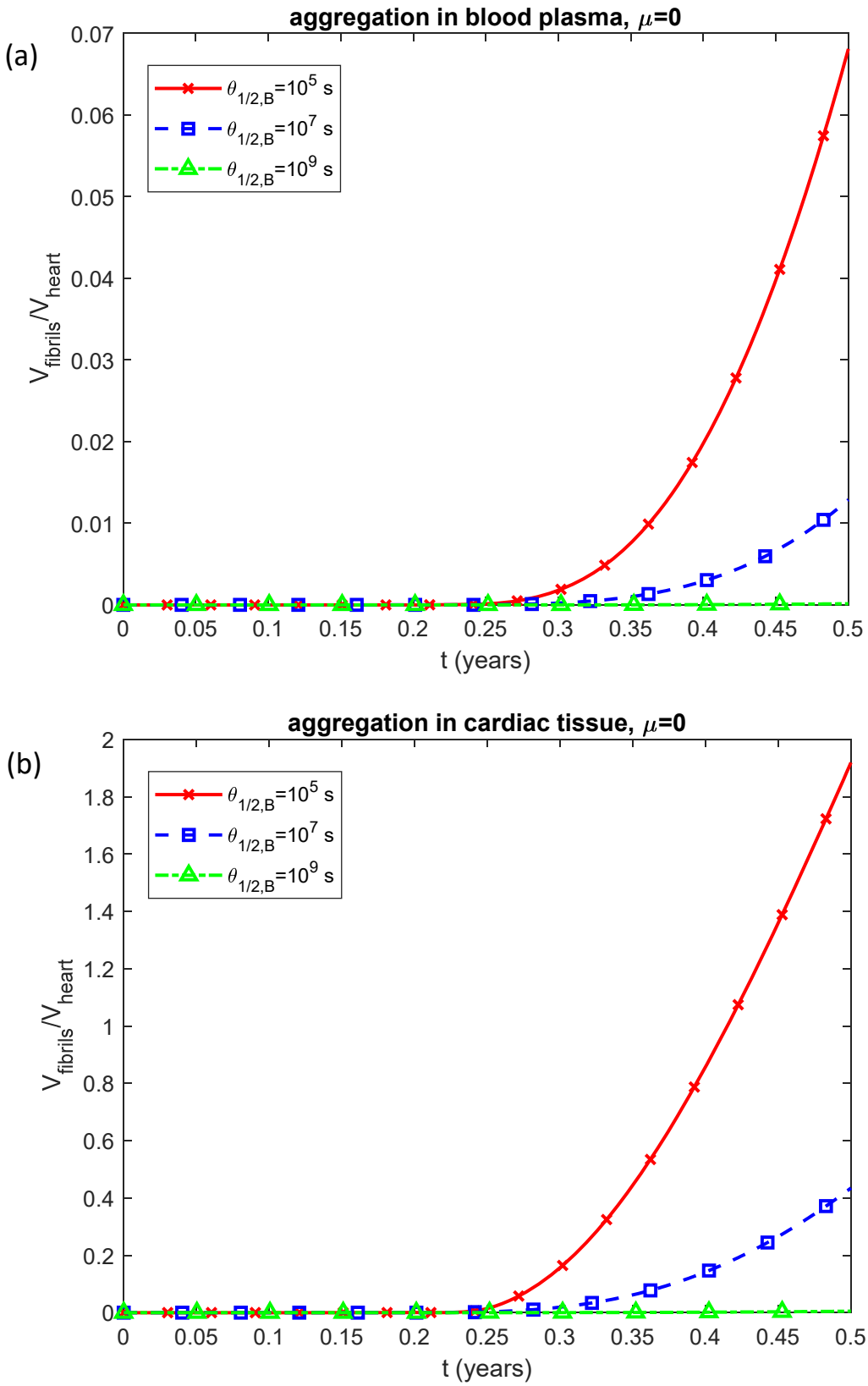
(a)
aggregation in blood plasma, μ=0
$\theta_{1/2,B}$=10^5 s
$\theta_{1/2,B}$=10^7 s
$\theta_{1/2,B}$=10^9 s
$V_{fibrils}/V_{heart}$
t (years)
(b)
aggregation in cardiac tissue, μ=0
$\theta_{1/2,B}$=10^5 s
$\theta_{1/2,B}$=10^7 s
$\theta_{1/2,B}$=10^9 s
$V_{fibrils}/V_{heart}$
t (years)

Figure 9

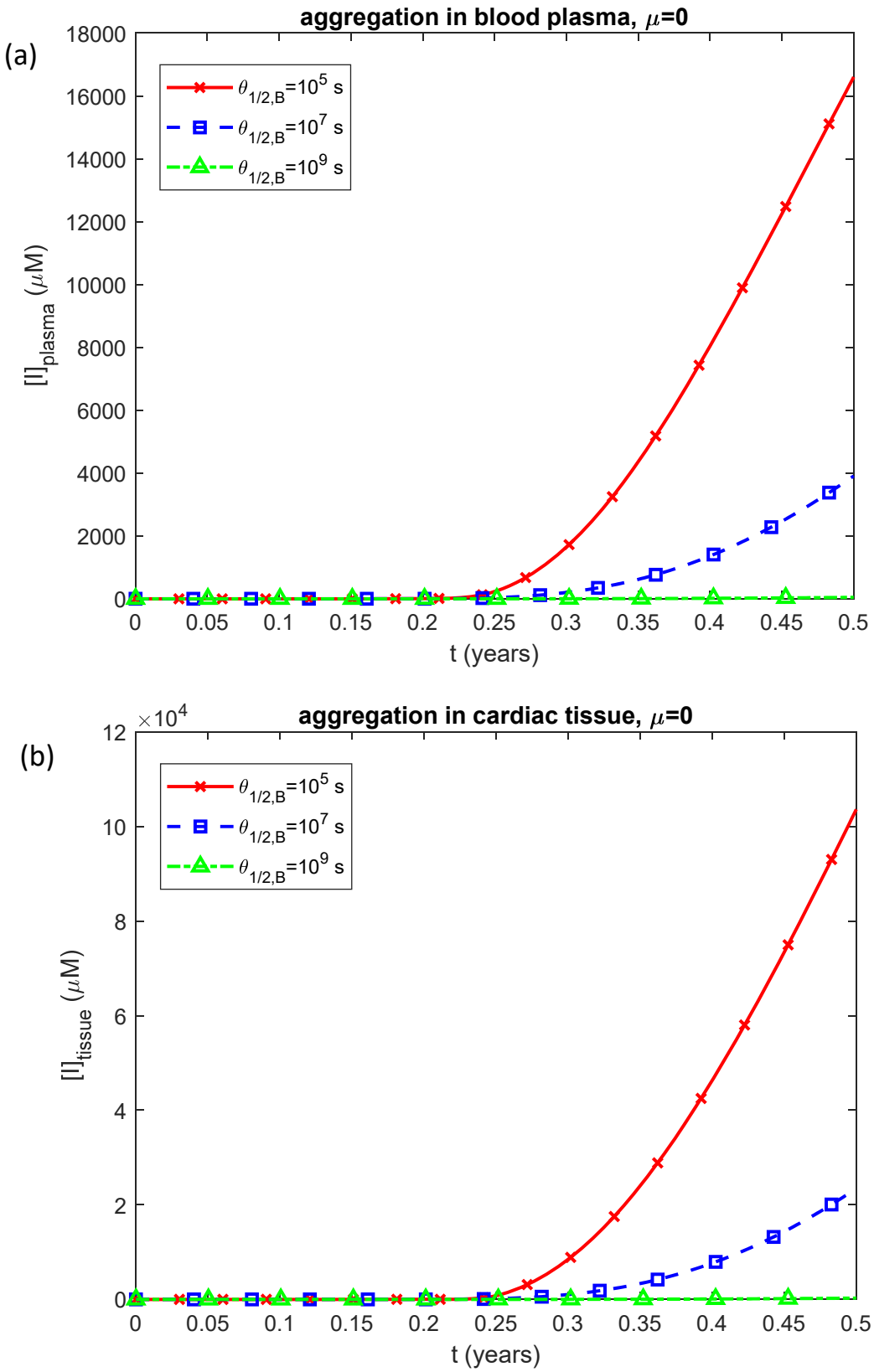
(a)
aggregation in blood plasma, μ=0
$\theta_{1/2,B}$=10^5 s
$\theta_{1/2,B}$=10^7 s
$\theta_{1/2,B}$=10^9 s
$[I]_{plasma}$ (μM)
t (years)
(b)
aggregation in cardiac tissue, μ=0
$\times 10^4$
$\theta_{1/2,B}$=10^5 s
$\theta_{1/2,B}$=10^7 s
$\theta_{1/2,B}$=10^9 s
$[I]_{tissue}$ (μM)
t (years)

Figure 10

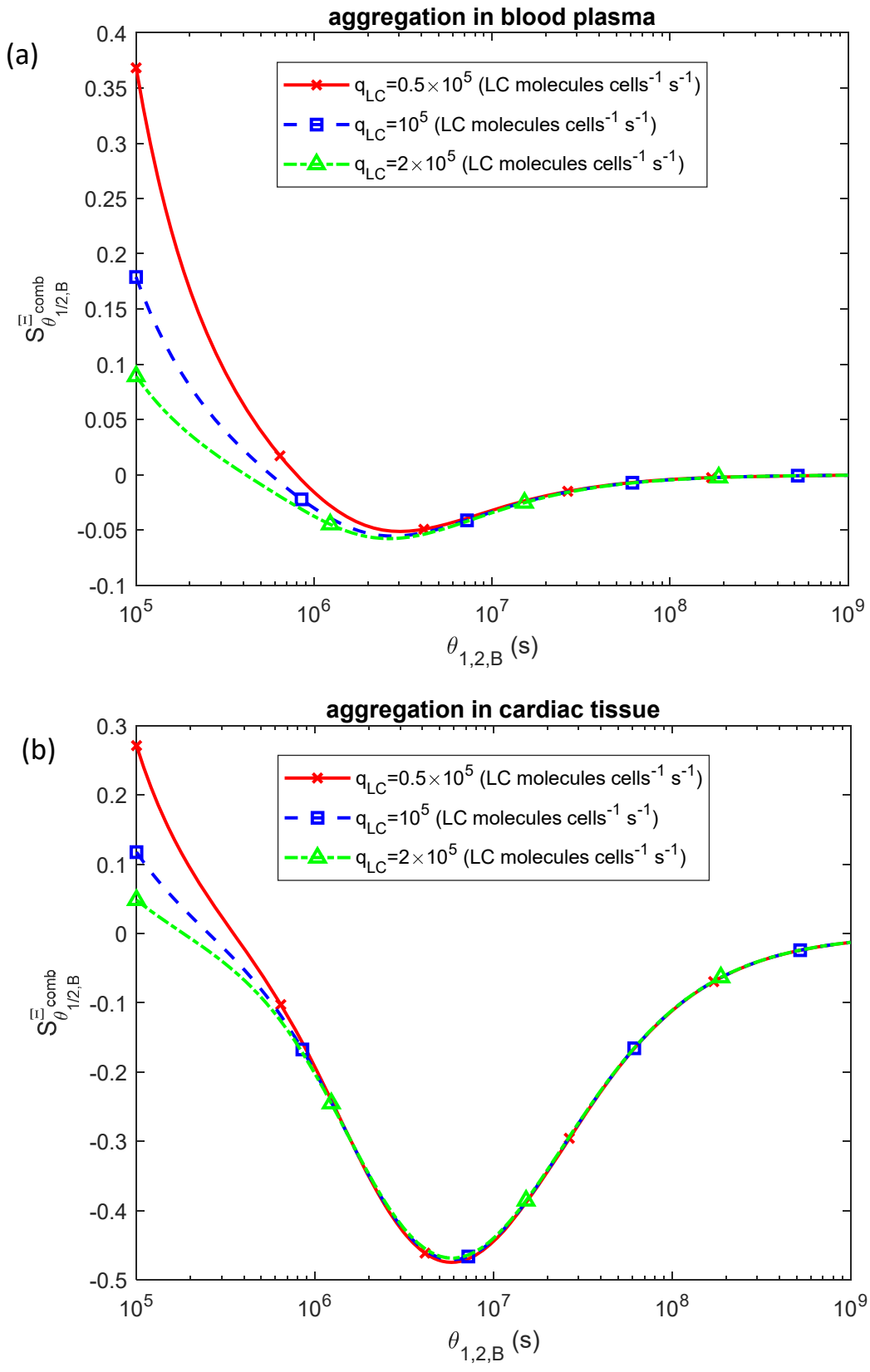
(a)
aggregation in blood plasma
$q_{LC}=0.5\times10^5$ (LC molecules cells^{-1} s^{-1})
$q_{LC}=10^5$ (LC molecules cells^{-1} s^{-1})
$q_{LC}=2\times10^5$ (LC molecules cells^{-1} s^{-1})
$S^{[I]}_{\theta^{comb}_{1/2,B}}$
$\theta_{1,2,B}$ (s)
(b)
aggregation in cardiac tissue
$q_{LC}=0.5\times10^5$ (LC molecules cells^{-1} s^{-1})
$q_{LC}=10^5$ (LC molecules cells^{-1} s^{-1})
$q_{LC}=2\times10^5$ (LC molecules cells^{-1} s^{-1})
$S^{[I]}_{\theta^{comb}_{1/2,B}}$
$\theta_{1,2,B}$ (s)

Figure 11

(a)

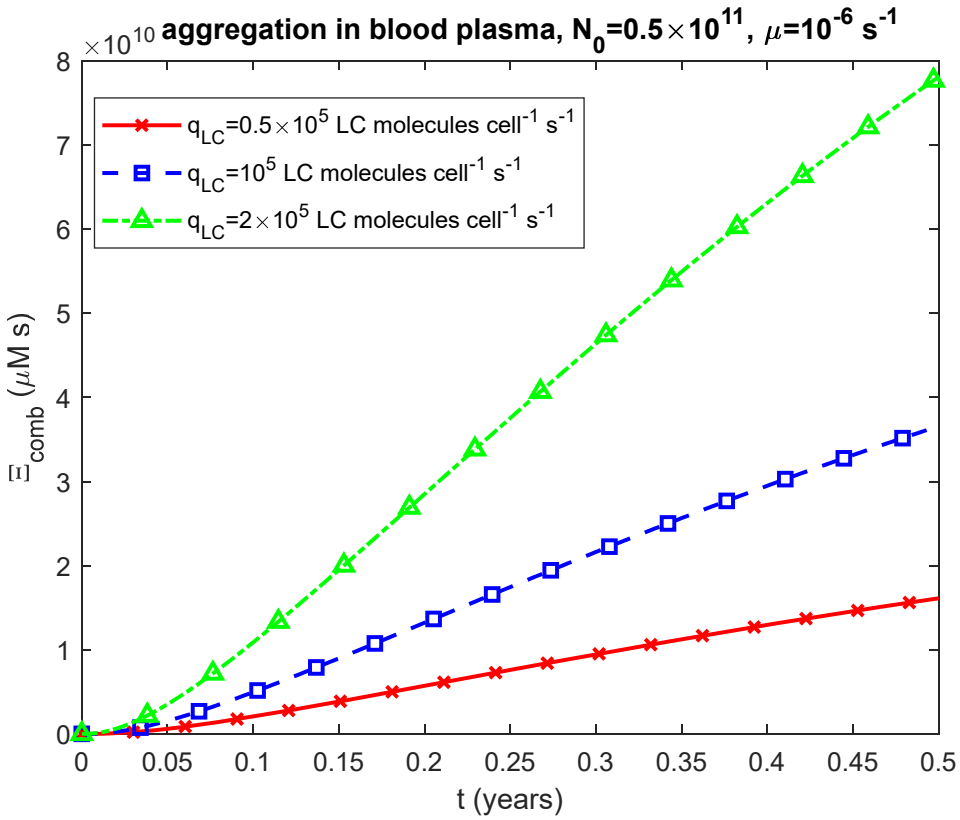
aggregation in blood plasma, N0=0.5×10^11, μ=10^-6 s^-1
×10^10
qLC=0.5×10^5 LC molecules cell^-1 s^-1
qLC=10^5 LC molecules cell^-1 s^-1
qLC=2×10^5 LC molecules cell^-1 s^-1
Ξcomb (μM s)
t (years)

(b)

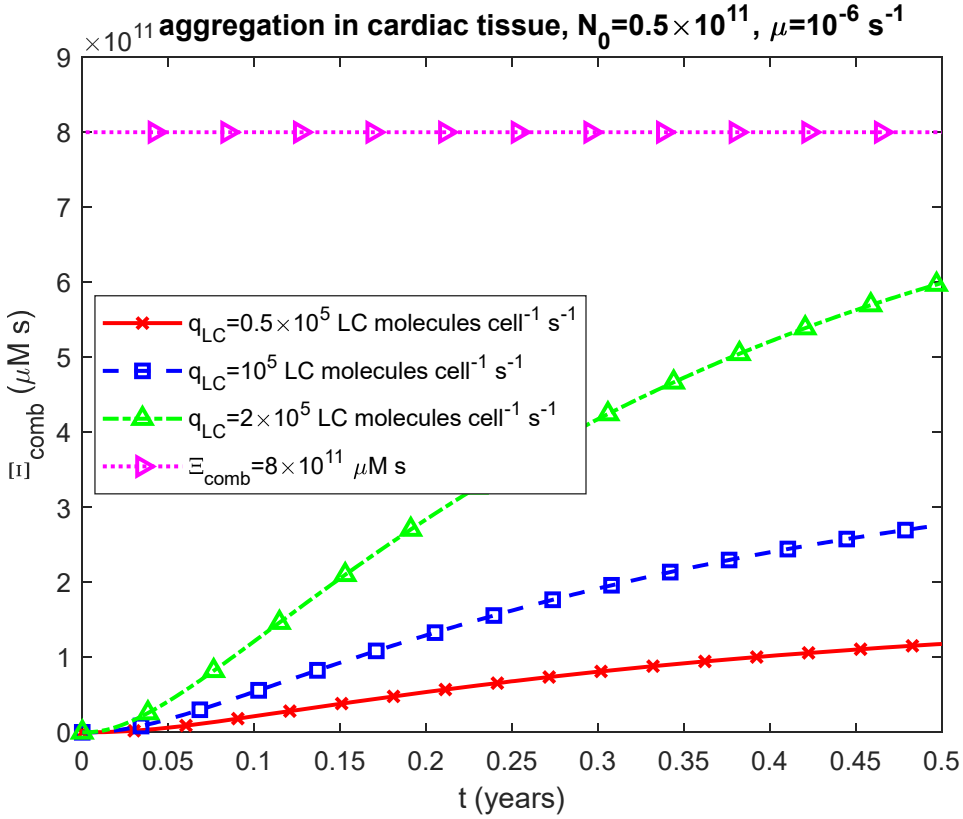
aggregation in cardiac tissue, N0=0.5×10^11, μ=10^-6 s^-1
×10^11
qLC=0.5×10^5 LC molecules cell^-1 s^-1
qLC=10^5 LC molecules cell^-1 s^-1
qLC=2×10^5 LC molecules cell^-1 s^-1
Ξcomb=8×10^11 μM s
Ξcomb (μM s)
t (years)

Figure 12

Mathematical Modeling of Light Chain Aggregation and Cardiac Damage in AL Amyloidosis

Andrey V Kuznetsov

Department of Mechanical and Aerospace Engineering, North Carolina State University,

Raleigh, NC 27695-7910, USA; e-mail: avkuznet@ncsu.edu

Supplemental Materials

S1. Gompertzian function

When $\mu = 0$ in Eq. (1), corresponding to the absence of anticancer treatment, the solution of Eq. (1) with initial condition (2) takes the form of the Gompertzian function:

$$N = N_0 \exp\left(\frac{\alpha}{\beta}\left(1 - \exp\left(-\beta t\right)\right)\right) \tag{S1}$$

In the absence of anticancer treatment Eqs. (1) and (2) can be reformulated as (Sullivan and Salmon 1972):

$$\frac{dN}{dt} = \eta N \tag{S2}$$

$$\frac{d\eta}{dt} = -\alpha\eta \tag{S3}$$

Eqs. (S2) and (S3) are solved subject to the following initial conditions:

$$N(0) = N_0, \qquad \eta(0) = \alpha \tag{S4a,b}$$

The solution of Eqs. (S2)–(S4) is expressed by Eq. (S1), which gives $N(t)$, together with the following solution for $\eta(t)$:

$$\eta(t) = \alpha \exp\left(-\beta t\right) \tag{S5}$$

Accordingly, Eq. (S2) can be reformulated as:

$$\frac{dN}{dt} = \alpha \exp\left(-\beta t\right) N \tag{S6}$$

to be solved under the initial condition (S4a).

Eq. (S6) demonstrates that, in the Gompertzian model, the exponential decay rate—equal to α at $t=0$—decreases exponentially at a constant rate β .

S2. Numerical solution

Algebraic Eq. (7) was solved numerically using the FZERO root-finding algorithm in MATLAB (R2024a, MathWorks, Natick, MA, USA). Initial value problems for ordinary differential equations were addressed using MATLAB's ODE45 solver (R2024a, MathWorks, Natick, MA, USA). Specifically, Eq. (1) was integrated with initial condition (2), and Eq. (9) was solved with initial condition (10). For scenario 1, Eqs. (13)–(16) were solved under initial conditions (17), whereas for scenario 2, Eqs. (18)–(21) were solved with initial conditions (22). The ODE45 solver, which implements an adaptive step-size Runge–Kutta method, was selected for its balance between accuracy and computational efficiency. To ensure high numerical precision, both the relative and absolute tolerances were set to 1e-10.

S3. Supplementary figures

(a)

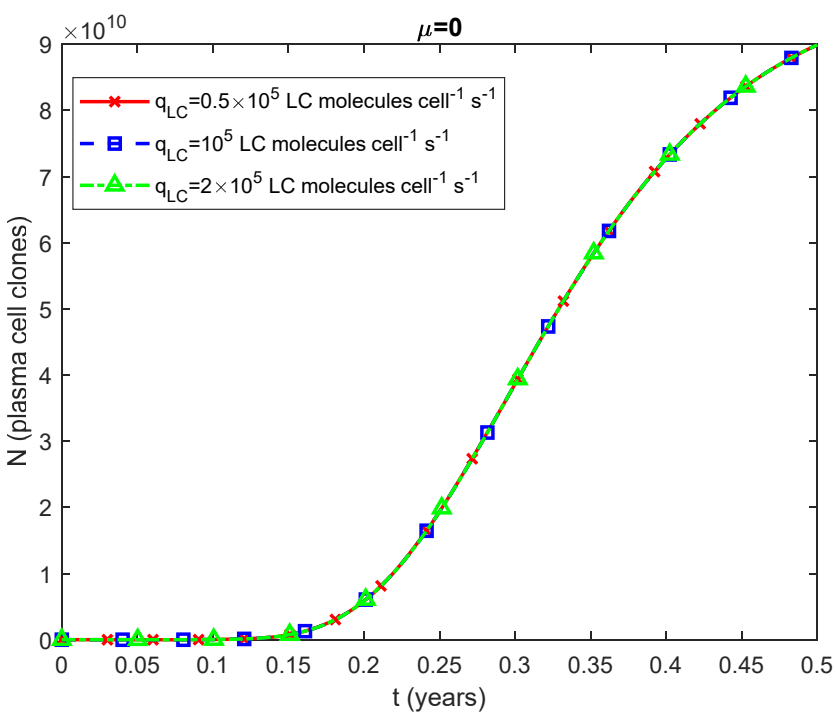

(b)

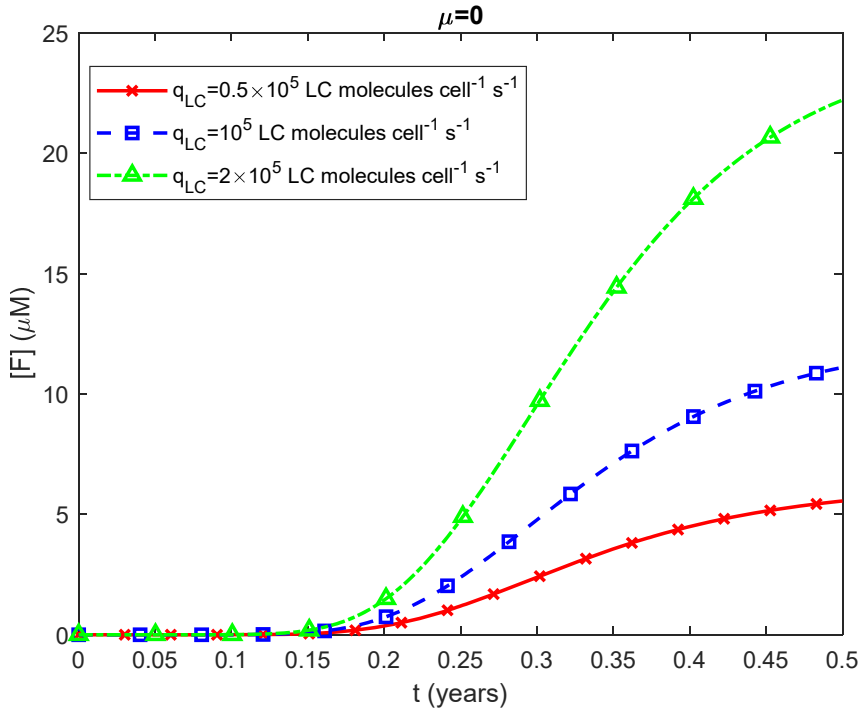

Fig. S1. (a) Number of plasma cell clones, *N*, vs time, *t*. The results indicate that this parameter is independent of q_{LC}. (b) Plasma molar concentration of natively folded Ig LC monomers secreted by clonal plasma cells vs time for three different values of the secretion rate of folded LCs per single plasma cell belonging to a clonal population, q_{LC}. Computations were performed for $k_u = 4\times10^{-4}$ s^{-1}. The case without anticancer therapy.

(a)

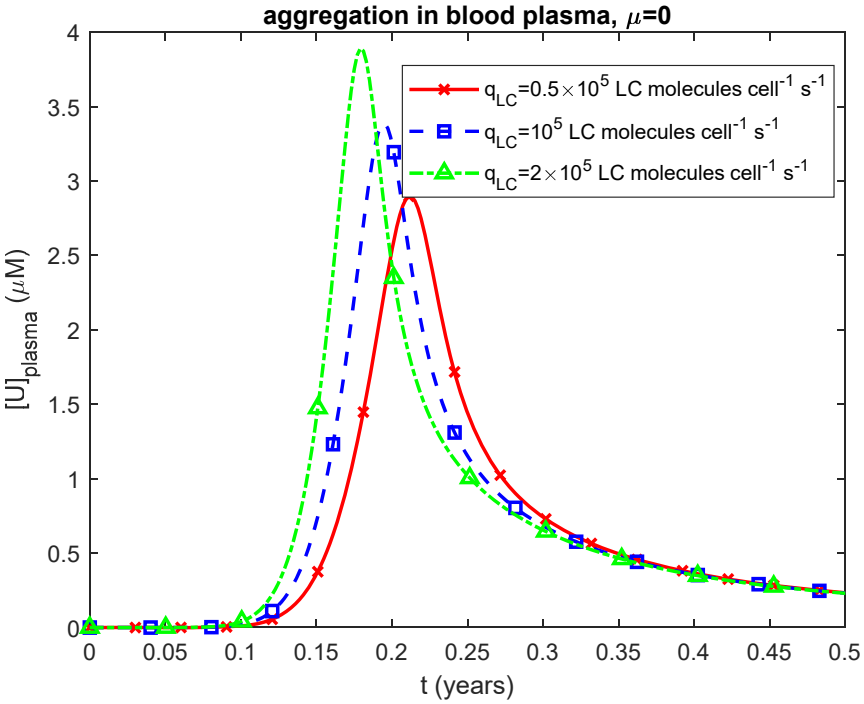

(b)

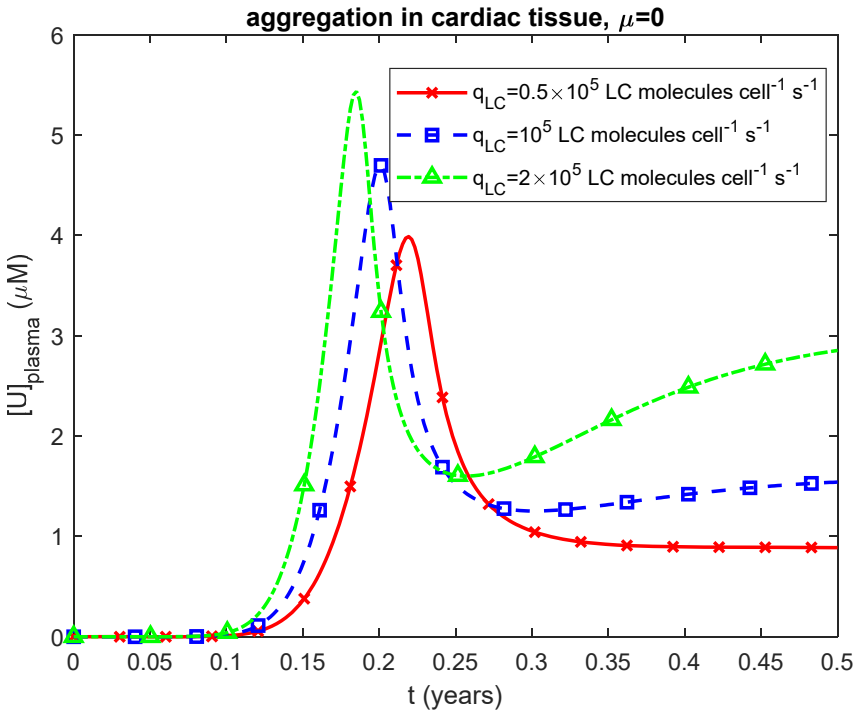

Fig. S2. Plasma molar concentration of unfolded Ig LC monomers susceptible to aggregation, $[U]_{plasma}$, vs time, t, for the scenarios of (a) aggregation occurring in the blood plasma and (b) aggregation occurring within the cardiac tissue. Results are shown for three different values of the secretion rate of folded LCs

produced by a single plasma cell belonging to a clonal population, q_{LC}. Computations were performed for $k_1 = 10^{-6}$ s^{-1}, $k_2 = 10^{-6}$ μM^{-1} s^{-1}, $k_u = 4\times10^{-4}$ s^{-1}, $\theta_{1/2,B} = 10^7$ s, and $\theta_{1/2,I} = 10^7$ s. The case without anticancer therapy.

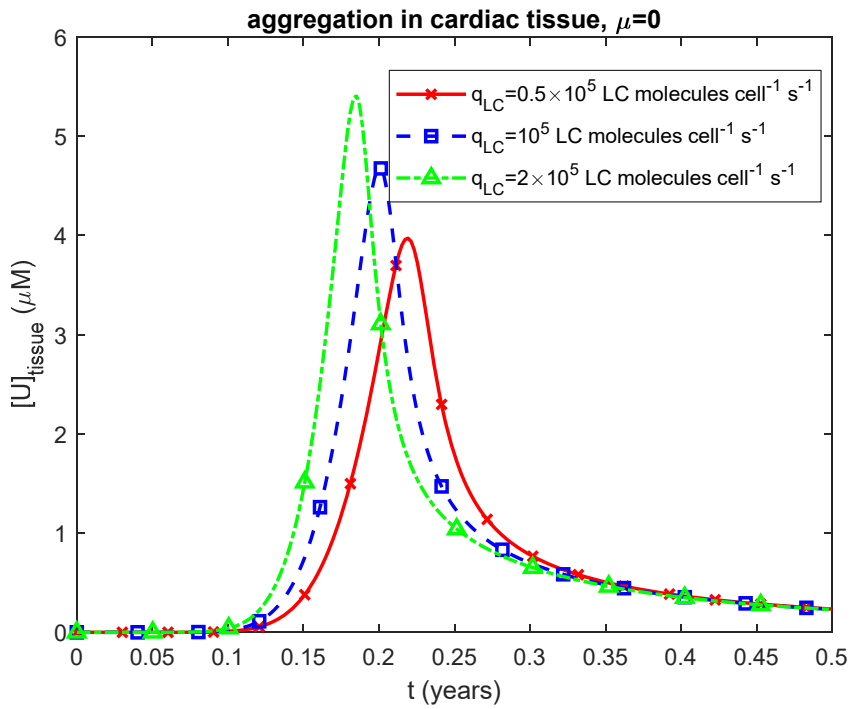

Fig. S3. Molar concentration of unfolded Ig LC monomers in cardiac tissue, $[U]_{tissue}$, vs time, *t*, for the scenario where aggregation occurs within the tissue. Results are shown for three different values of the secretion rate of folded LCs produced by a single plasma cell belonging to a clonal population, q_{LC}. Computations were performed for $k_1 = 10^{-6}$ s^{-1}, $k_2 = 10^{-6}$ μM^{-1} s^{-1}, $k_u = 4\times10^{-4}$ s^{-1}, and $\theta_{1/2,B} = 10^7$ s. The case without anticancer therapy.

(a)

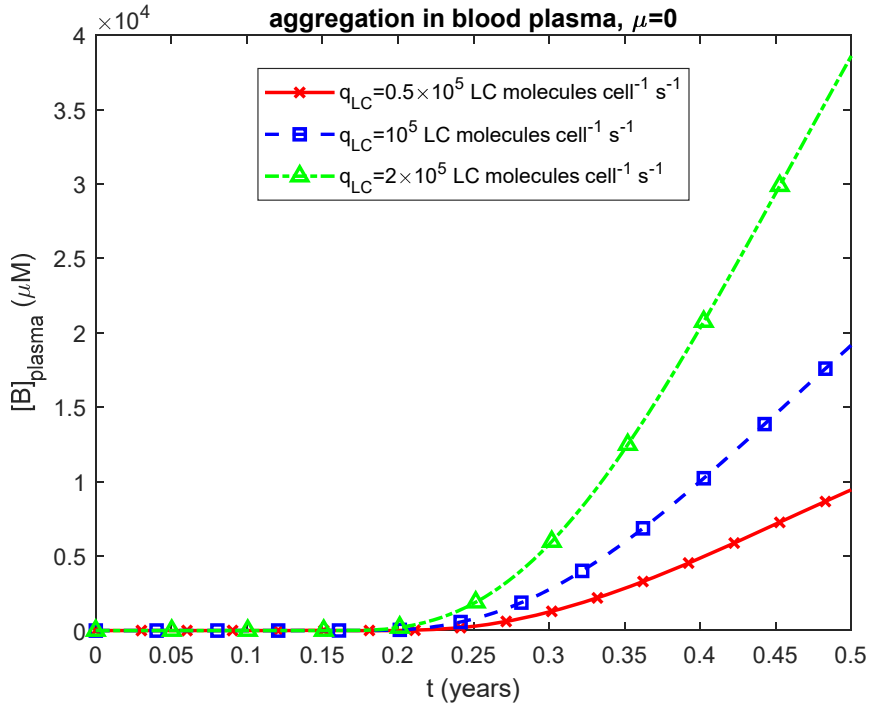

(b)

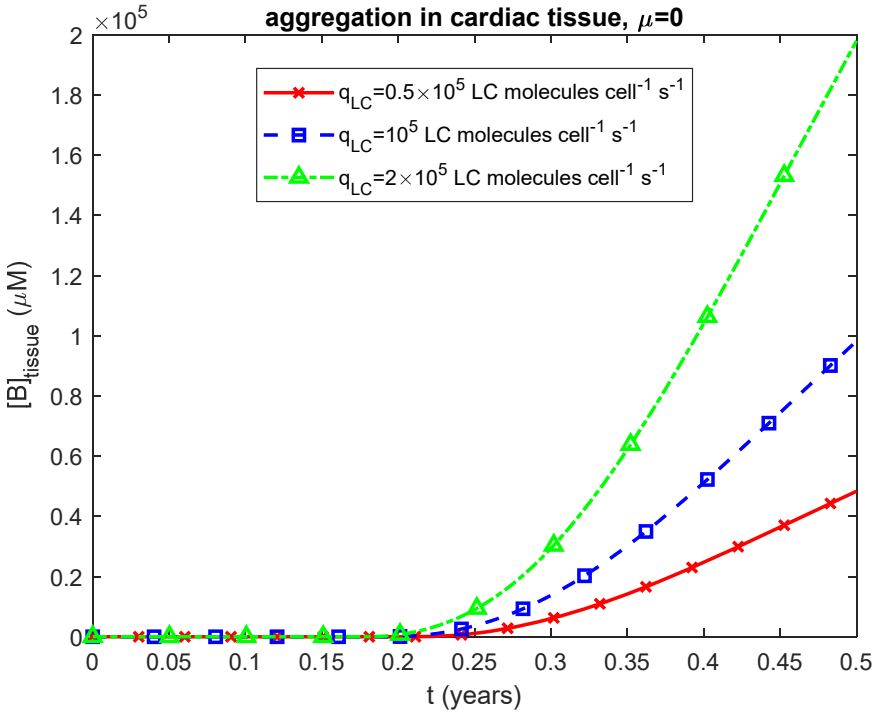

Fig. S4. (a) Molar concentration of free LC oligomers in blood plasma, $[B]_{plasma}$, vs time, t, when aggregation occurs in the plasma, and (b) molar concentration of free LC oligomers in cardiac tissue,

$[B]_{tissue}$, vs time, t, when aggregation occurs within the tissue. Results are shown for three different values of the secretion rate of folded LCs produced by a single plasma cell belonging to a clonal population, q_{LC}. Computations were performed for $k_1 = 10^{-6}$ s^{-1}, $k_2 = 10^{-6}$ μM^{-1} s^{-1}, $k_u = 4\times10^{-4}$ s^{-1}, $\theta_{1/2,B} = 10^7$ s, and $\theta_{1/2,I} = 10^7$ s. The case without anticancer therapy.

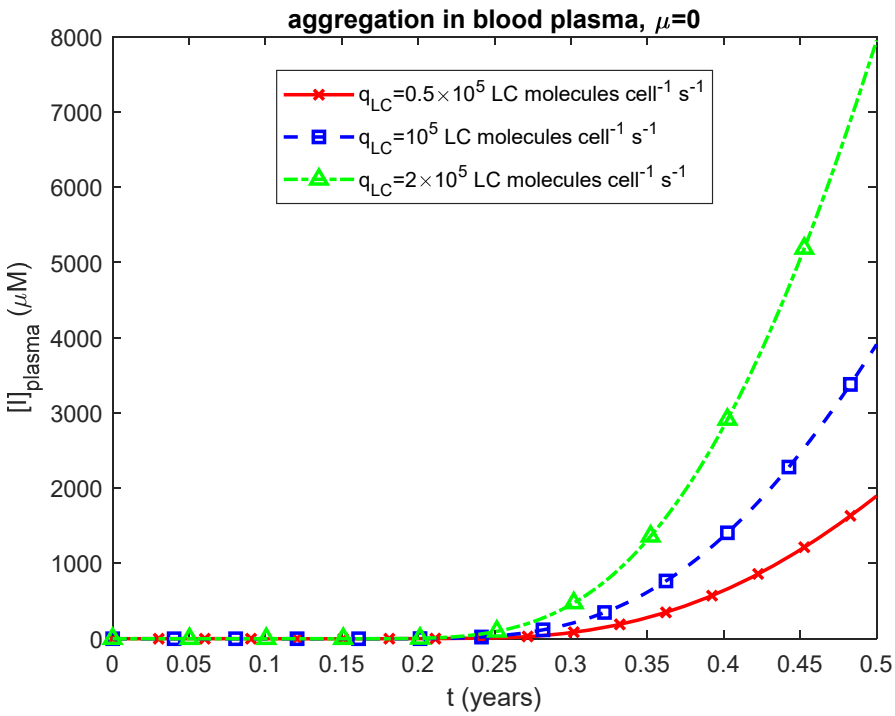

Fig. S5. Molar concentration of LC oligomers deposited into amyloid protofibrils circulating within blood plasma, $[I]_{plasma}$, vs time, t. Results are shown for three different values of the secretion rate of folded LCs produced by a single plasma cell belonging to a clonal population, q_{LC}. Computations were performed for $k_1 = 10^{-6}$ s^{-1}, $k_2 = 10^{-6}$ μM^{-1} s^{-1}, $k_u = 4\times10^{-4}$ s^{-1}, $\theta_{1/2,B} = 10^7$ s, and $\theta_{1/2,I} = 10^7$ s. The case without anticancer therapy.

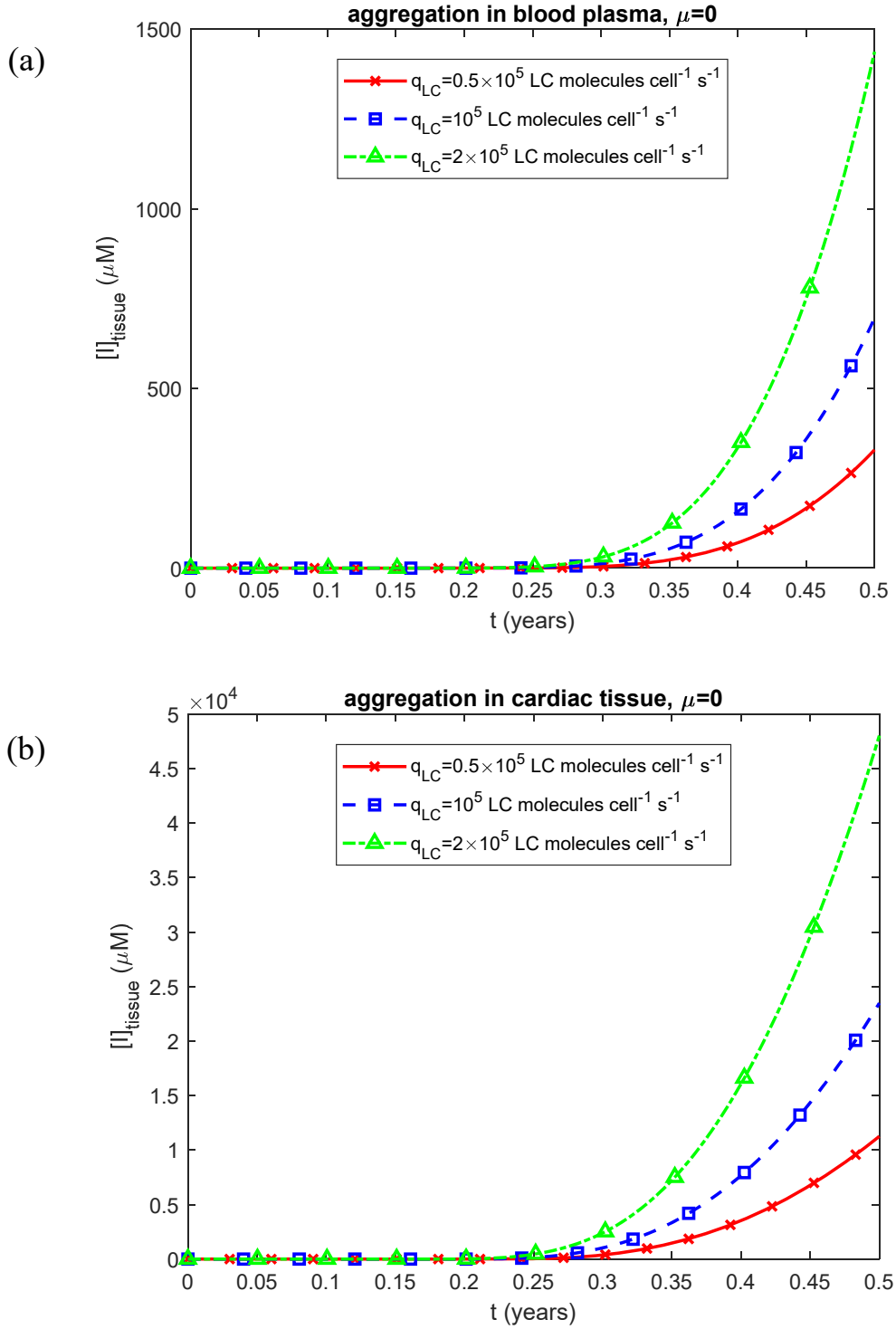

Fig. S6. Molar concentration of LC oligomers incorporated into amyloid fibrils infiltrating the cardiac tissue, $[I]_{tissue}$, vs time, t, for two scenarios: (a) aggregation occurring in the blood plasma and (b) aggregation occurring within the cardiac tissue. Results are shown for three different values of the

secretion rate of folded LCs produced by a single plasma cell belonging to a clonal population, q_{LC}. Computations were performed for $k_1 = 10^{-6}$ s^{-1}, $k_2 = 10^{-6}$ μM^{-1} s^{-1}, $k_u = 4\times10^{-4}$ s^{-1}, $\theta_{1/2,B} = 10^7$ s, and $\theta_{1/2,I} = 10^7$ s. The case without anticancer therapy.

(a)

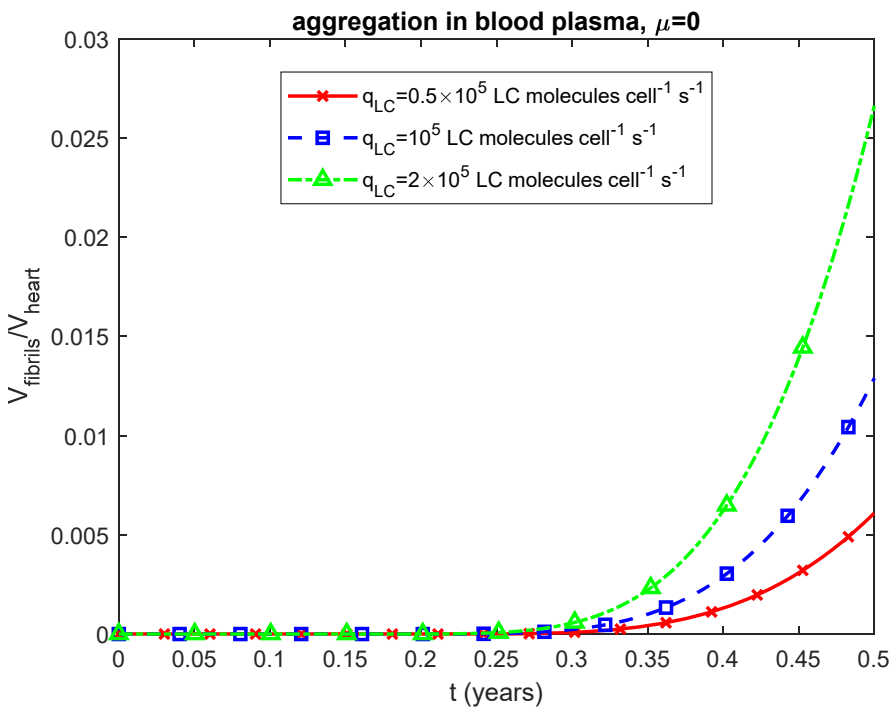

(b)

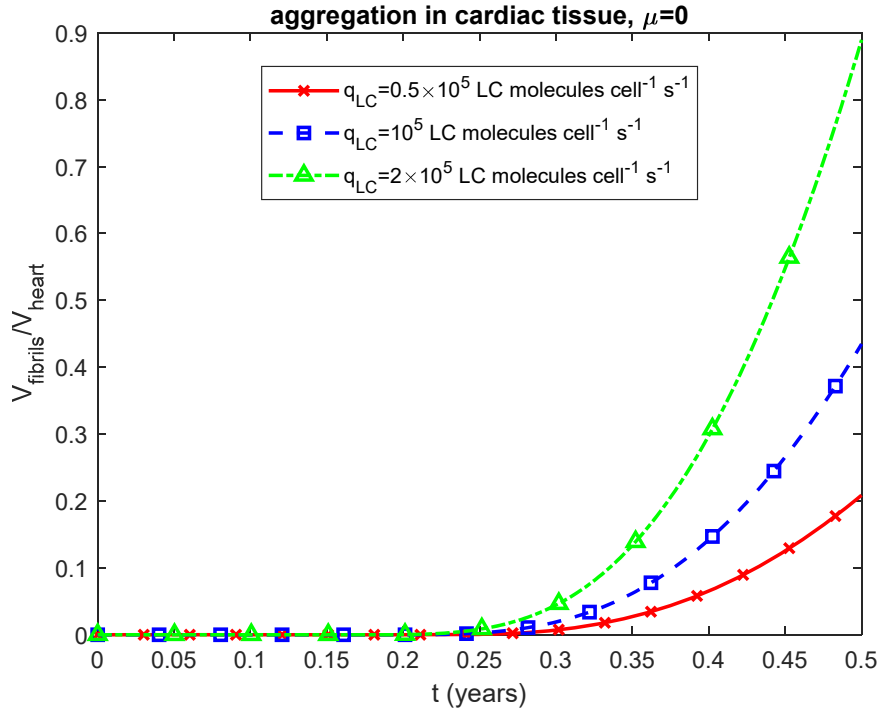

Fig. S7. Fraction of myocardial volume occupied by LC fibrils, $V_{fibrils} / V_{heart}$, vs time, t, for two scenarios: (a) aggregation occurring in the blood plasma and (b) aggregation occurring within the cardiac tissue. Results are presented for three different values of the secretion rate of folded LCs produced by a single plasma cell belonging to a clonal population, q_{LC}. Computations were performed for $k_1 = 10^{-6}$ s^{-1}, $k_2 = 10^{-6}$ μM^{-1} s^{-1}, $k_u = 4\times10^{-4}$ s^{-1}, $\theta_{1/2,B} = 10^7$ s, and $\theta_{1/2,I} = 10^7$ s. The case without anticancer therapy.

(a)

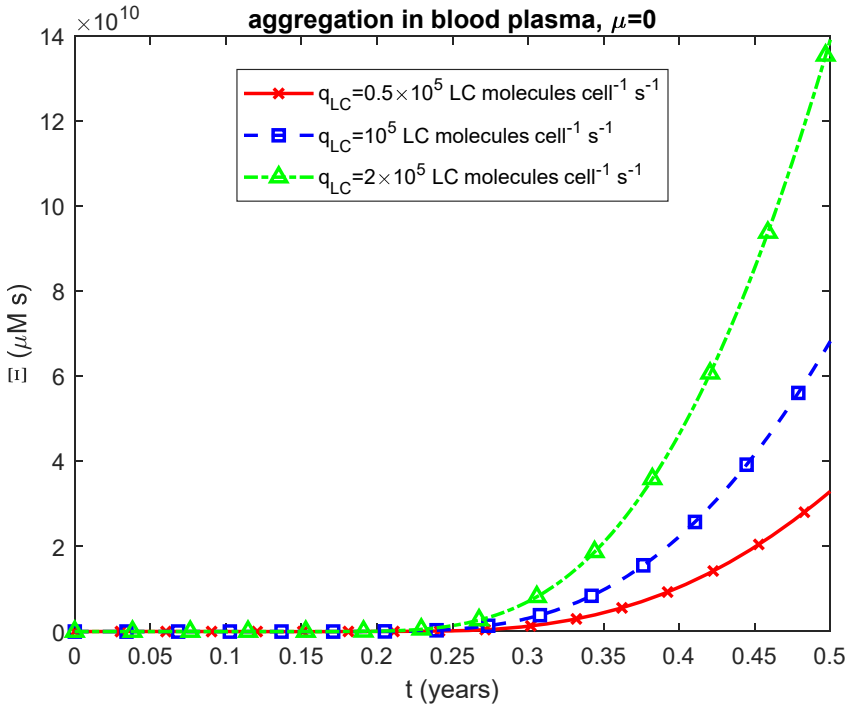

(b)

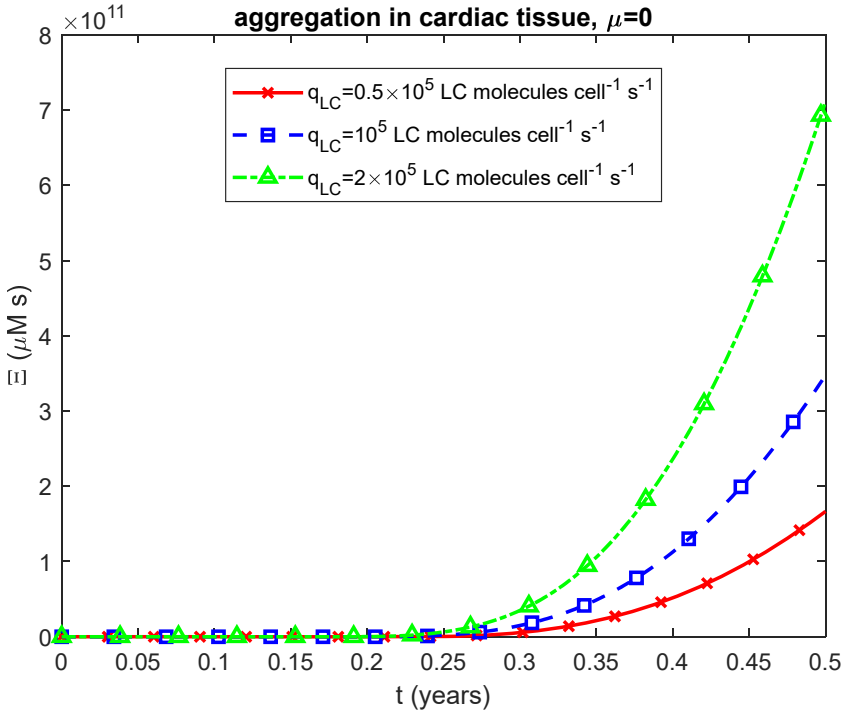

Fig. S8. Time-dependent criterion for accumulated cardiotoxicity induced by LC oligomers, Ξ, vs time, *t*, for two scenarios: (a) aggregation occurring in the blood plasma and (b) aggregation occurring within the cardiac tissue. Results are presented for three different values of the secretion rate of folded LCs produced

by a single plasma cell belonging to a clonal population, q_{LC}. Computations were performed for $k_1 = 10^{-6}$ s^{-1}, $k_2 = 10^{-6}$ μM^{-1} s^{-1}, $k_u = 4\times10^{-4}$ s^{-1}, $\theta_{1/2,B} = 10^7$ s, and $\theta_{1/2,I} = 10^7$ s. The case without anticancer therapy.

(a)

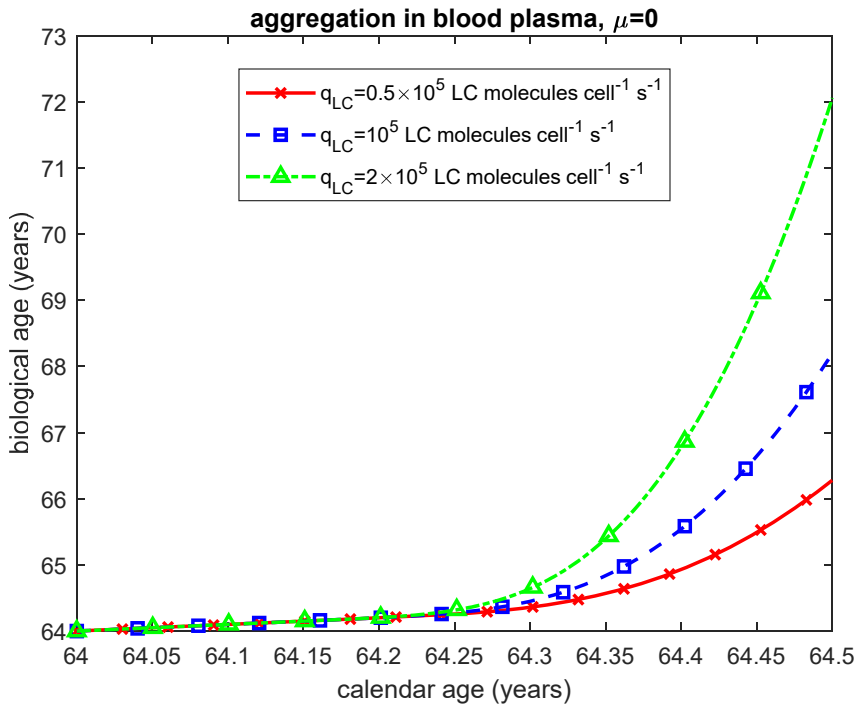

(b)

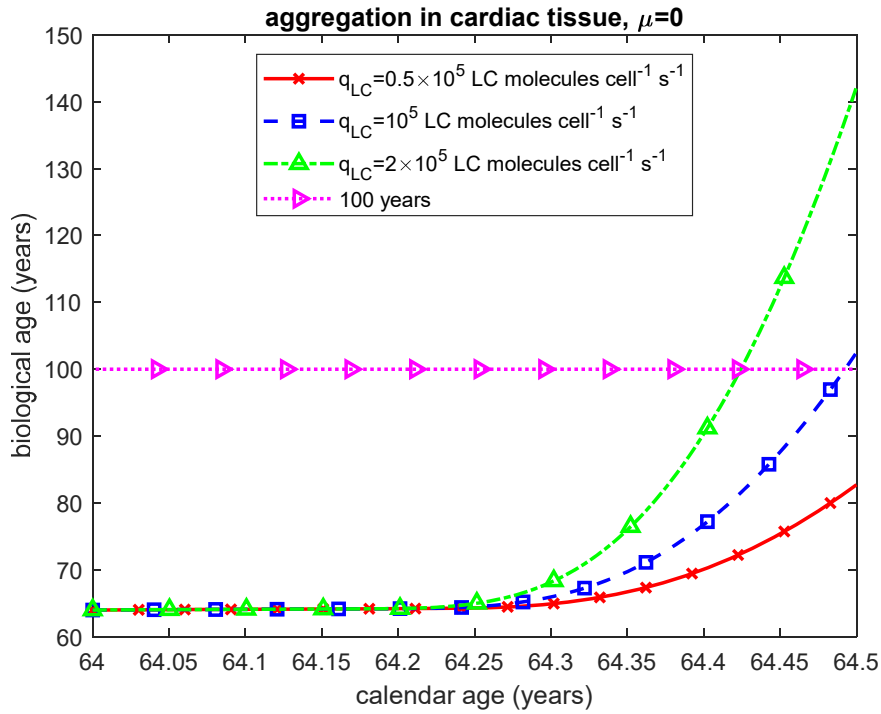

Fig. S9. Biological age vs calendar age under two scenarios: (a) aggregation occurring in the blood plasma and (b) aggregation occurring within the cardiac tissue. Results are presented for three different values of the secretion rate of folded LCs produced by a single plasma cell belonging to a clonal population, q_{LC}. Computations were performed for $k_1 = 10^{-6}$ s^{-1}, $k_2 = 10^{-6}$ μM^{-1} s^{-1}, $k_u = 4\times10^{-4}$ s^{-1}, $\theta_{1/2,B} = 10^7$ s, and $\theta_{1/2,I} = 10^7$ s. The case without anticancer therapy.

(a)

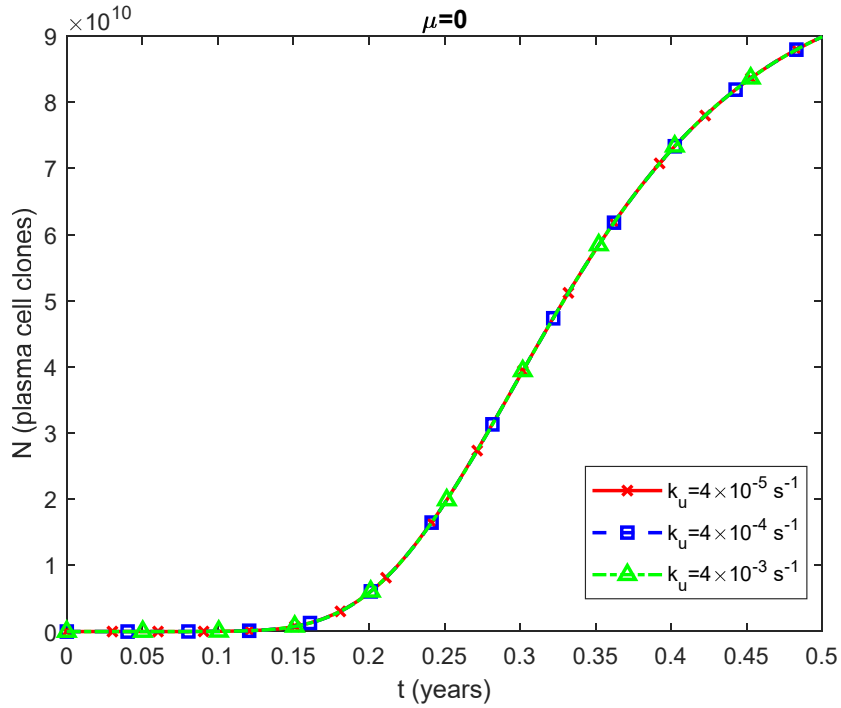

(b)

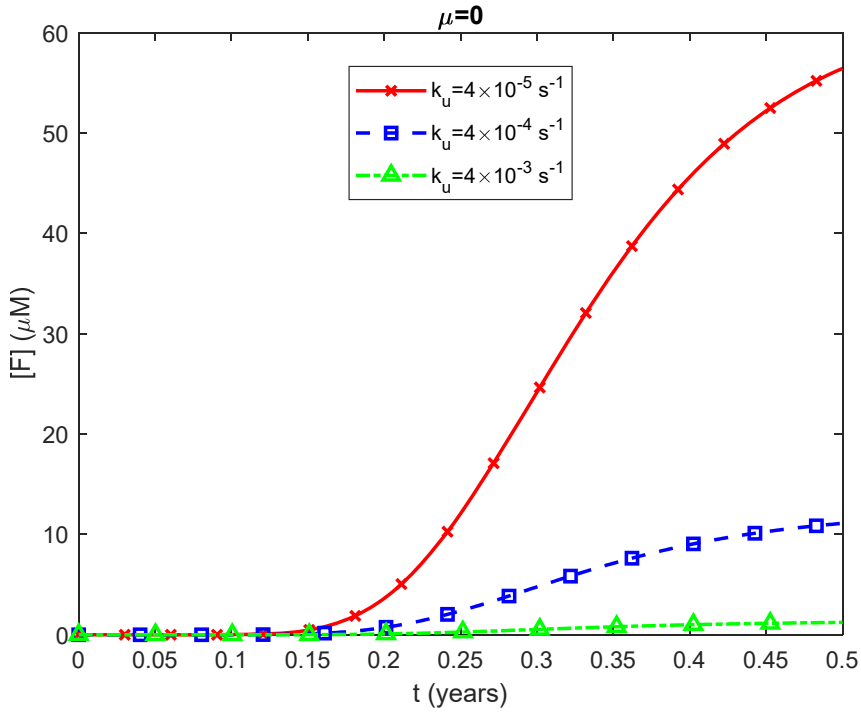

Fig. S10. (a) Number of plasma cell clones, *N*, vs time, *t*. The results indicate that this parameter is independent of k_u. (b) Plasma molar concentration of natively folded Ig LC monomers secreted by clonal

plasma cells, $[F]$, vs time, t, for three different values of the rate of unfolding of LCs, k_u. Computations were performed for $q_{LC} = 10^5 \ \frac{\text{LC molecules}}{\text{cell s}}$. The case without anticancer therapy.

(a)

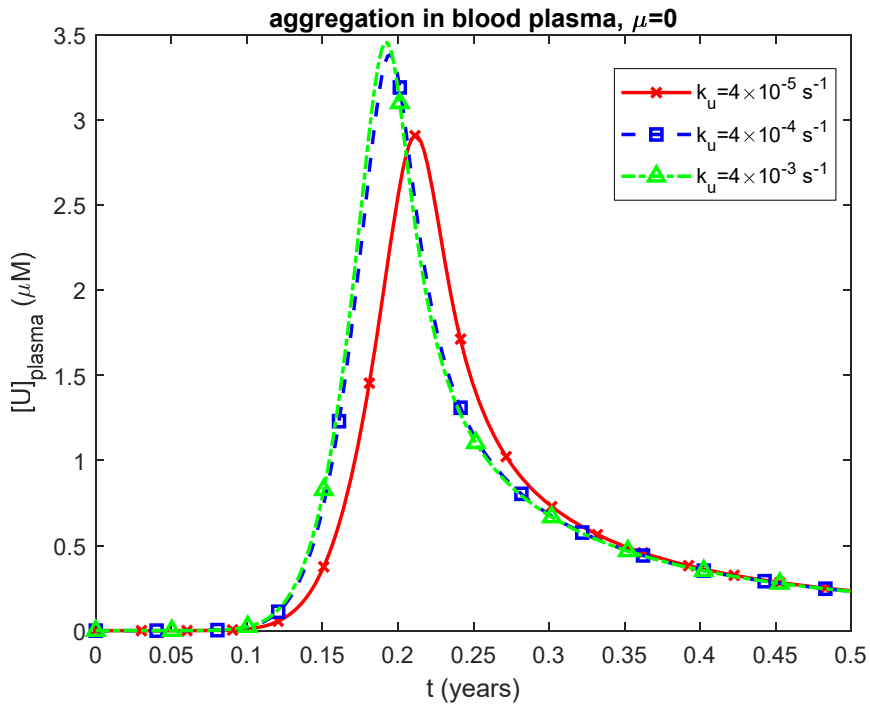

(b)

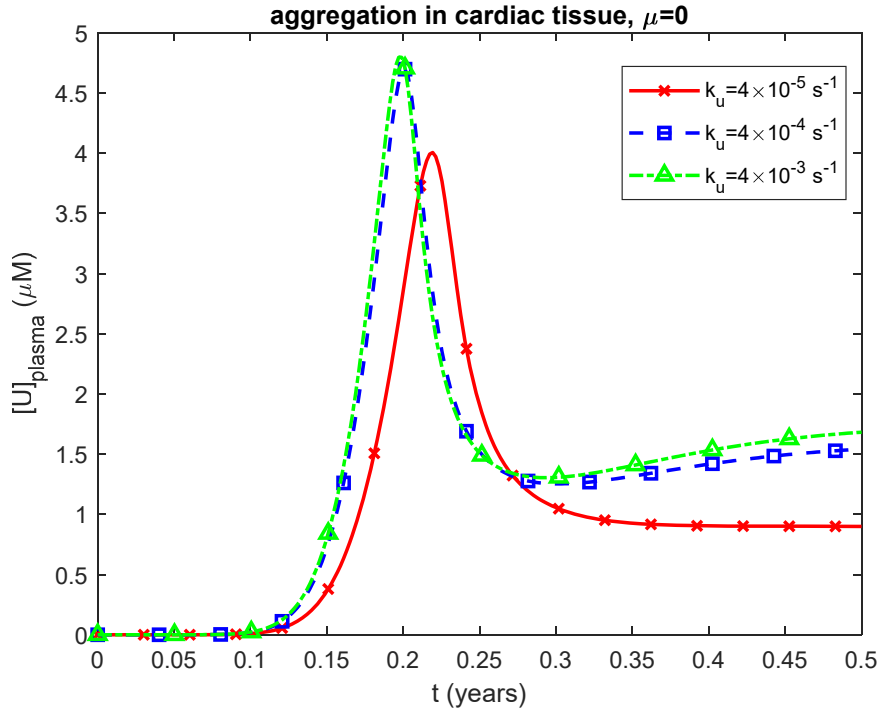

Fig. S11. Plasma molar concentration of unfolded Ig LC monomers susceptible to aggregation, $[U]_{plasma}$, vs time, *t*, for the scenarios of (a) aggregation occurring in the blood plasma and (b) aggregation occurring within the cardiac tissue. Results are shown for three different values of the rate of unfolding of LCs, k_u. Computations were performed for $k_1 = 10^{-6}$ s^{-1}, $k_2 = 10^{-6}$ μM^{-1} s^{-1}, $q_{LC} = 10^5 \ \frac{\text{LC molecules}}{\text{cell s}}$, $\theta_{1/2,B} = 10^7$ s, and $\theta_{1/2,I} = 10^7$ s. The case without anticancer therapy.

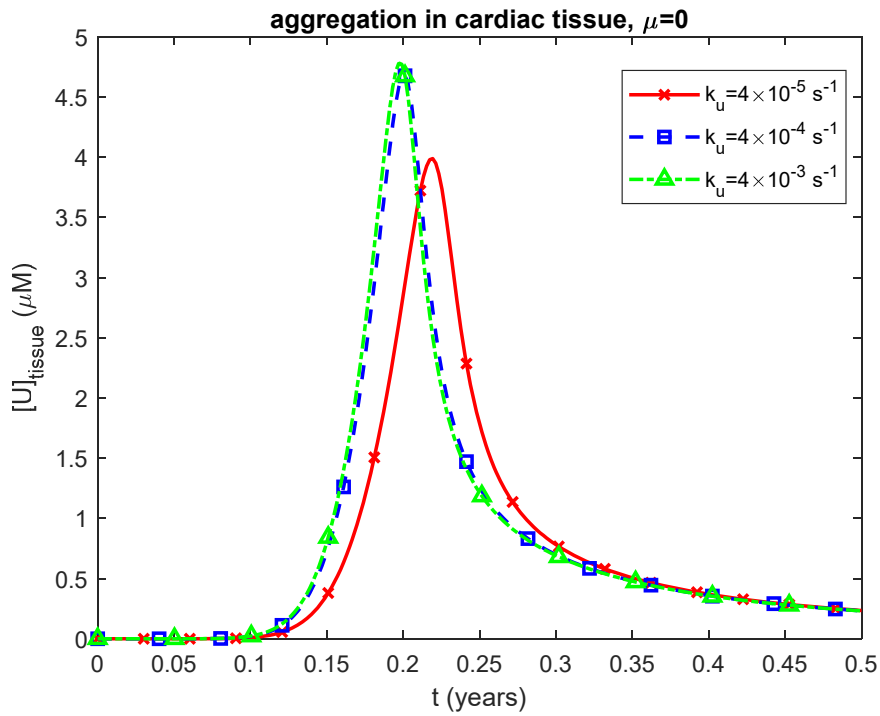

Fig. S12. Molar concentration of unfolded Ig LC monomers in cardiac tissue, $[U]_{tissue}$, vs time, t, for the scenario where aggregation occurs within the tissue. Results are shown for three different values of the rate of unfolding of LCs, k_u. Computations were performed for $k_1 = 10^{-6}$ s^{-1}, $k_2 = 10^{-6}$ μM^{-1} s^{-1}, $q_{LC} = 10^5$ $\frac{\text{LC molecules}}{\text{cell s}}$, and $\theta_{1/2,B} = 10^7$ s. The case without anticancer therapy.

(a)

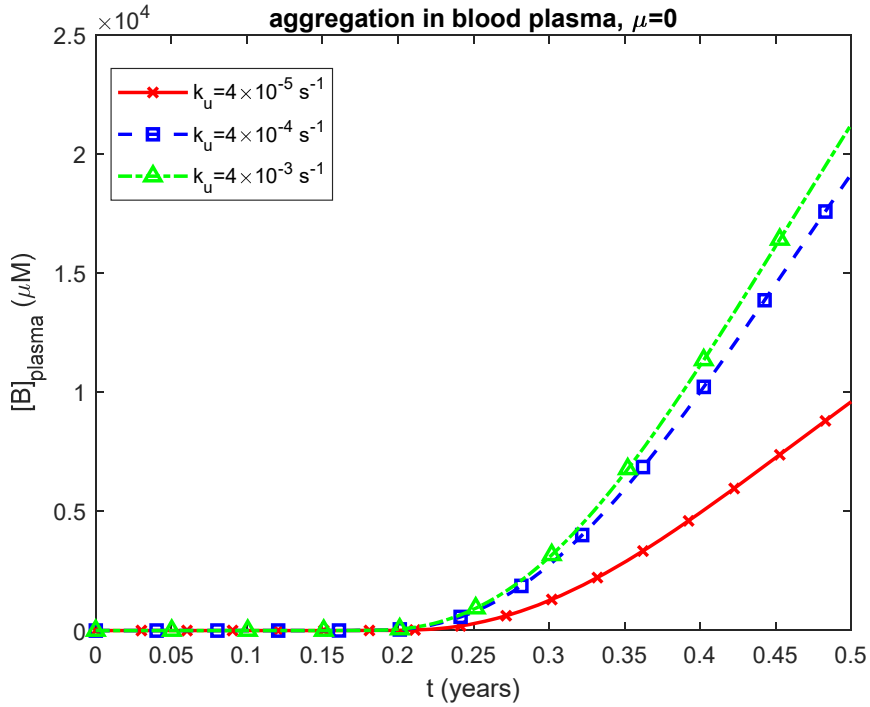

(b)

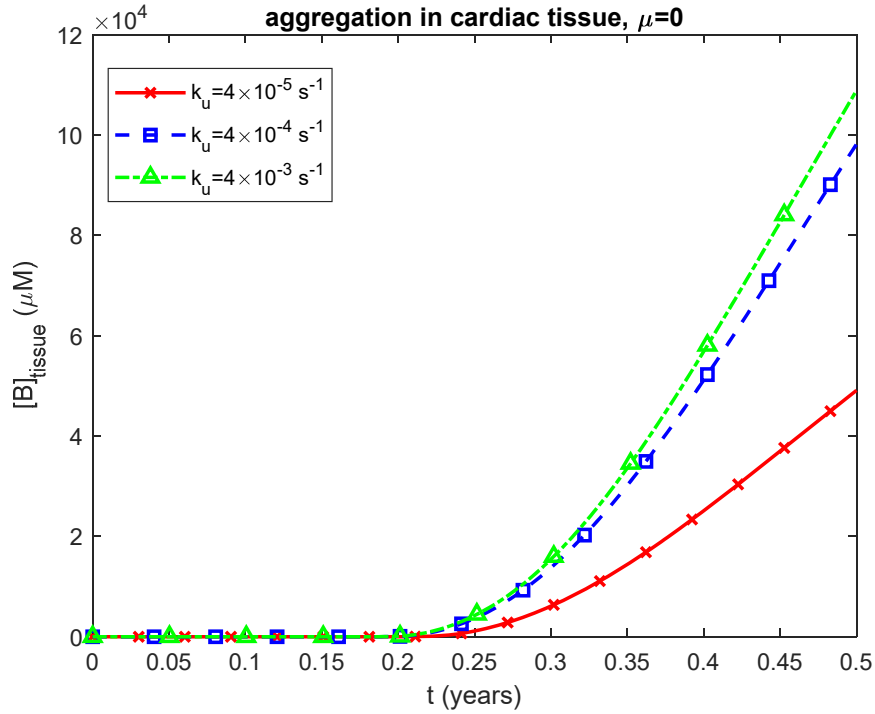

Fig. S13. (a) Molar concentration of free LC oligomers in blood plasma, $[B]_{plasma}$, vs time, t, when aggregation occurs in the plasma and (b) molar concentration of free LC oligomers in cardiac tissue,

$[B]_{tissue}$, vs time, t, when aggregation occurs within the tissue. Results are shown for three different values of the rate of unfolding of LCs, k_u. Computations were performed for $k_1 = 10^{-6}$ s^{-1}, $k_2 = 10^{-6}$ μM^{-1} s^{-1}, $q_{LC} = 10^5 \ \frac{\text{LC molecules}}{\text{cell s}}$, $\theta_{1/2,B} = 10^7$ s, and $\theta_{1/2,I} = 10^7$ s. The case without anticancer therapy.

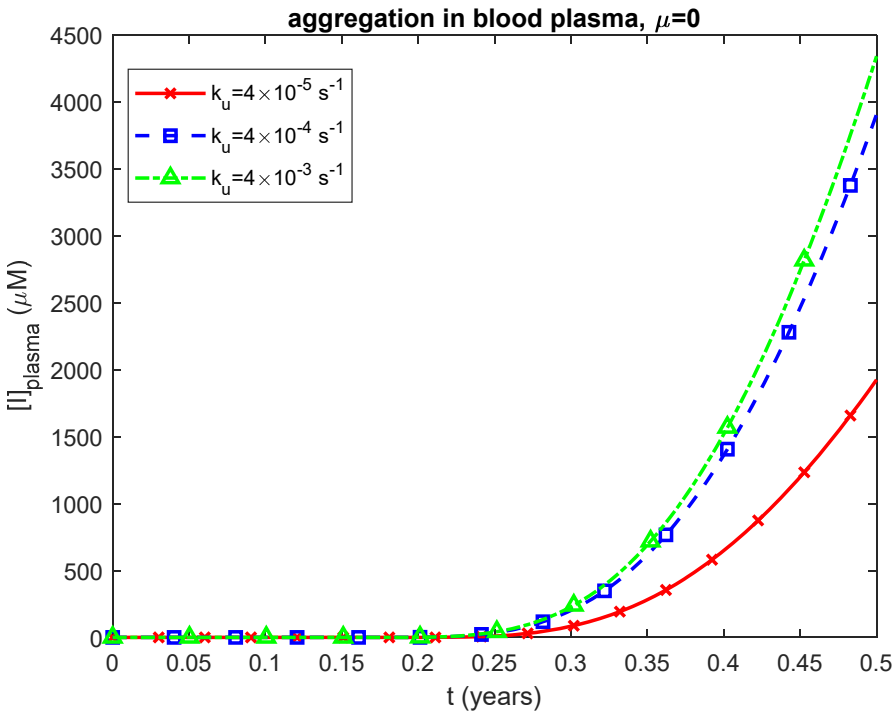

Fig. S14. Molar concentration of LC oligomers deposited into amyloid protofibrils circulating within blood plasma, $[I]_{plasma}$, vs time, t. Results are shown for three different values of the rate of unfolding of LCs, k_u. Computations were performed for $k_1 = 10^{-6}$ s^{-1}, $k_2 = 10^{-6}$ μM^{-1} s^{-1}, $q_{LC} = 10^5 \ \frac{\text{LC molecules}}{\text{cell s}}$, $\theta_{1/2,B} = 10^7$ s, and $\theta_{1/2,I} = 10^7$ s. The case without anticancer therapy.

(a)

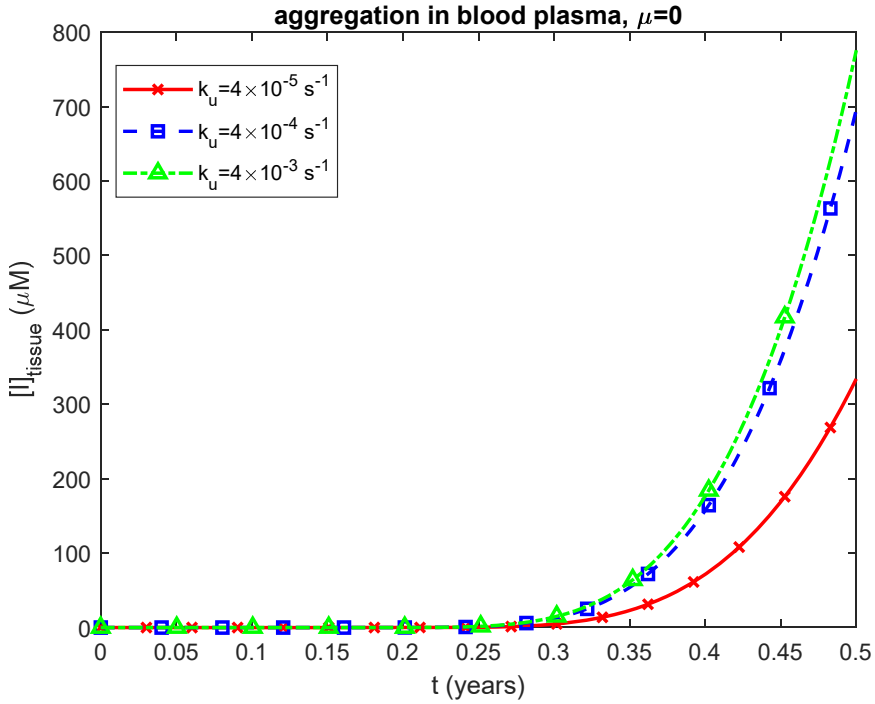

(b)

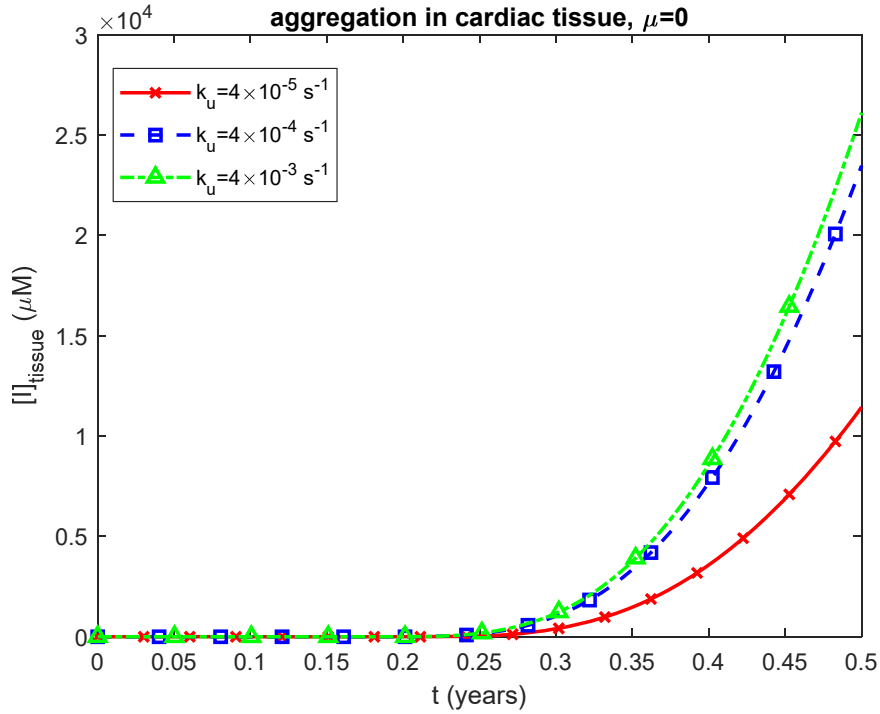

Fig. S15. Molar concentration of LC oligomers incorporated into amyloid fibrils infiltrating the cardiac tissue, $[I]_{tissue}$, vs time, t, for two scenarios: (a) aggregation occurring in the blood plasma and (b) aggregation occurring within the cardiac tissue. Results are shown for three different values of the rate of

unfolding of LCs, k_u. Computations were performed for $k_1 = 10^{-6}$ s^{-1}, $k_2 = 10^{-6}$ μM^{-1} s^{-1}, $q_{LC} = 10^5$ $\frac{\text{LC molecules}}{\text{cell s}}$, $\theta_{1/2,B} = 10^7$ s, and $\theta_{1/2,I} = 10^7$ s. The case without anticancer therapy.

(a)

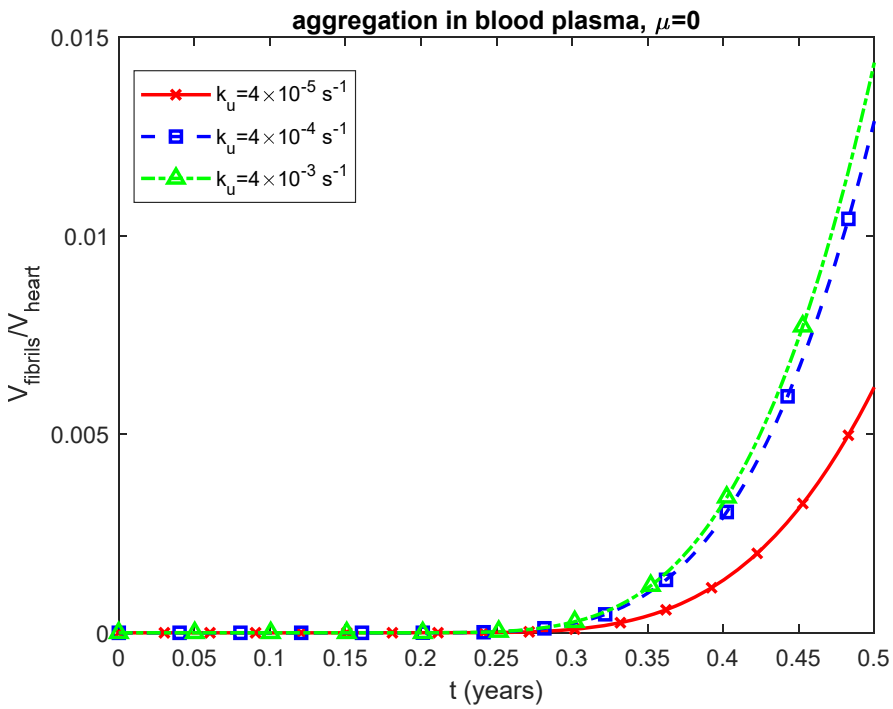

(b)

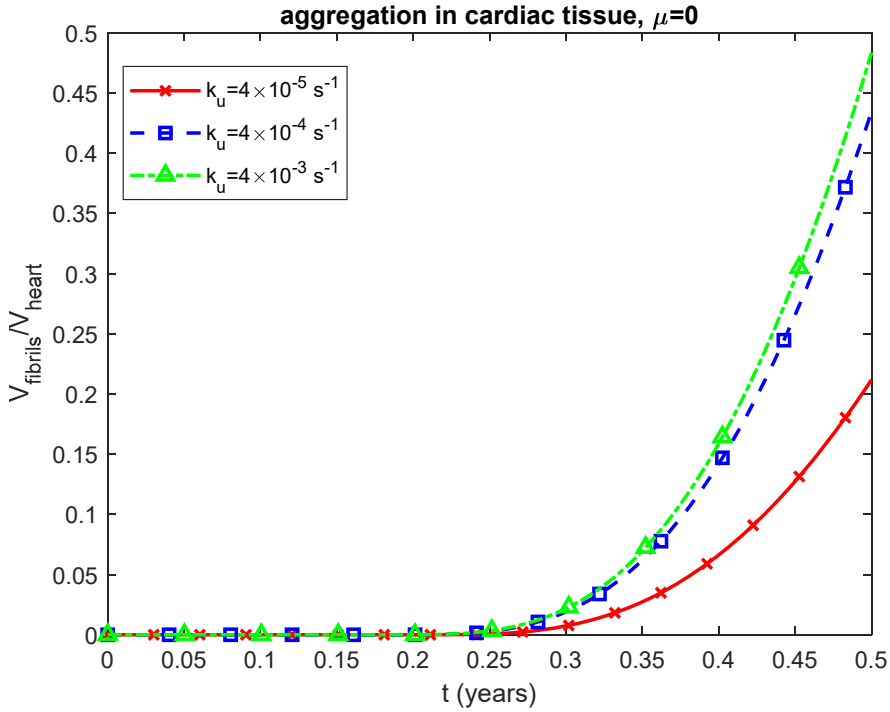

Fig. S16. Fraction of myocardial volume occupied by LC fibrils, $V_{fibrils} / V_{heart}$, vs time, t, for two scenarios: (a) aggregation occurring in the blood plasma and (b) aggregation occurring within the cardiac tissue. Results are shown for three different values of the rate of unfolding of LCs, k_u. Computations were performed for $k_1 = 10^{-6}$ s^{-1}, $k_2 = 10^{-6}$ μM^{-1} s^{-1}, $q_{LC} = 10^5 \ \frac{\text{LC molecules}}{\text{cell s}}$, $\theta_{1/2,B} = 10^7$ s, and $\theta_{1/2,I} = 10^7$ s. The case without anticancer therapy.

(a)

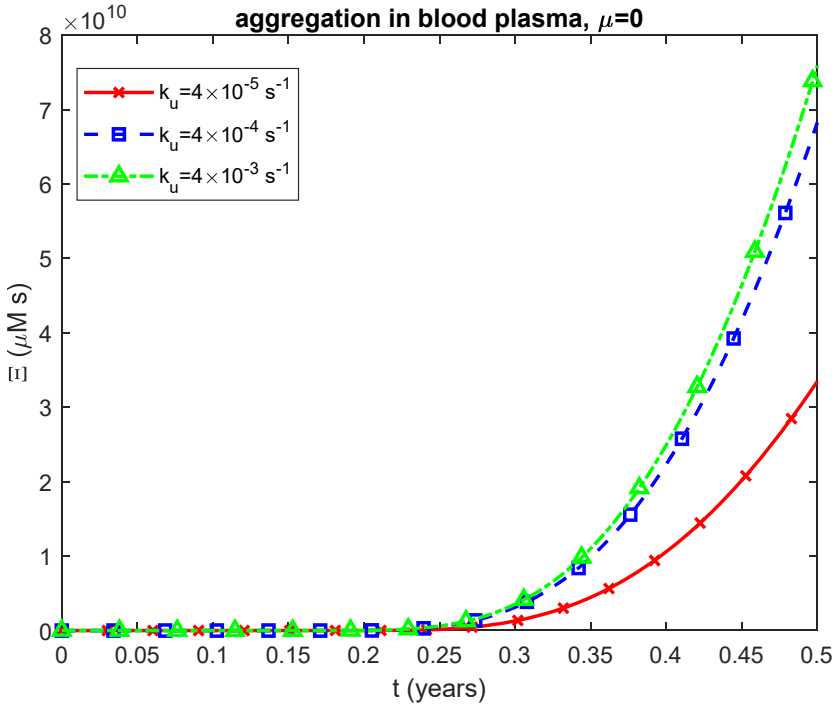

(b)

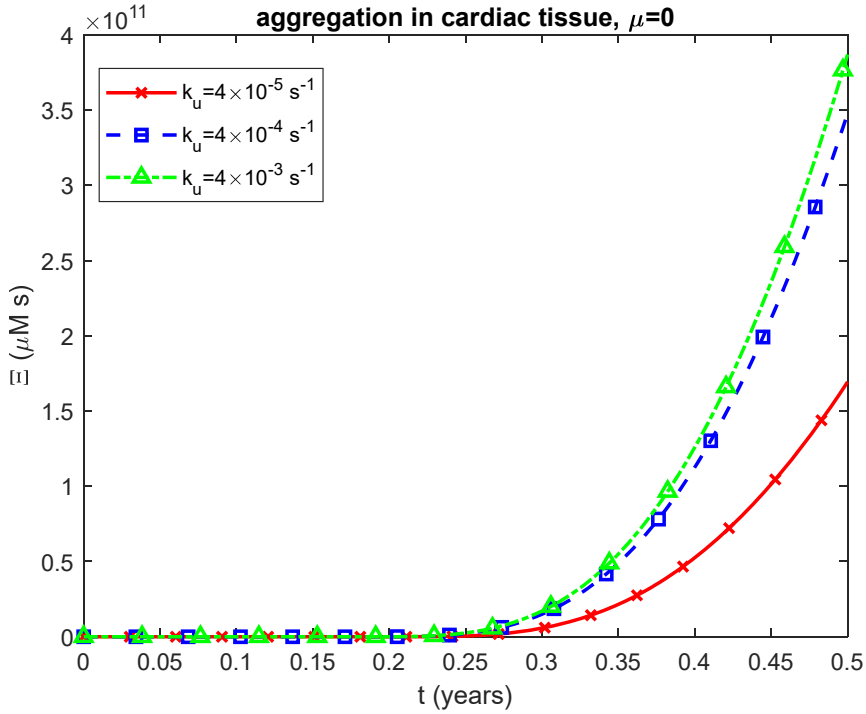

Fig. S17. Time-dependent criterion for accumulated cardiotoxicity induced by LC oligomers, Ξ, vs time, *t*, for two scenarios: (a) aggregation occurring in the blood plasma and (b) aggregation occurring within the cardiac tissue. Results are shown for three different values of the rate of unfolding of LCs, k_u.

Computations were performed for $k_1 = 10^{-6}$ s^{-1}, $k_2 = 10^{-6}$ μM^{-1} s^{-1}, $q_{LC} = 10^5 \ \frac{\text{LC molecules}}{\text{cell s}}$, $\theta_{1/2,B} = 10^7$ s, and $\theta_{1/2,I} = 10^7$ s. The case without anticancer therapy.

(a)

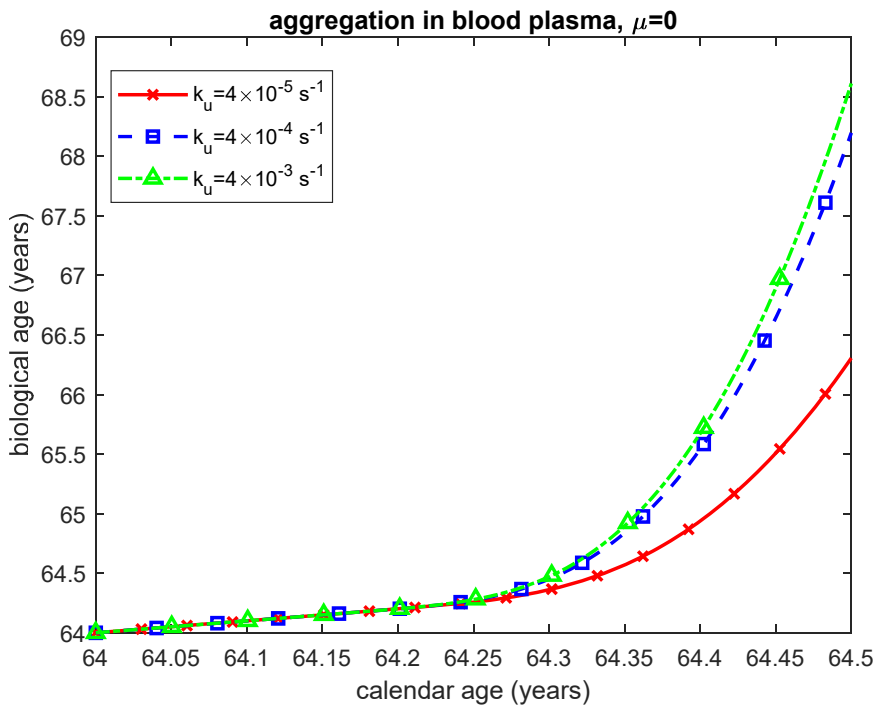

(b)

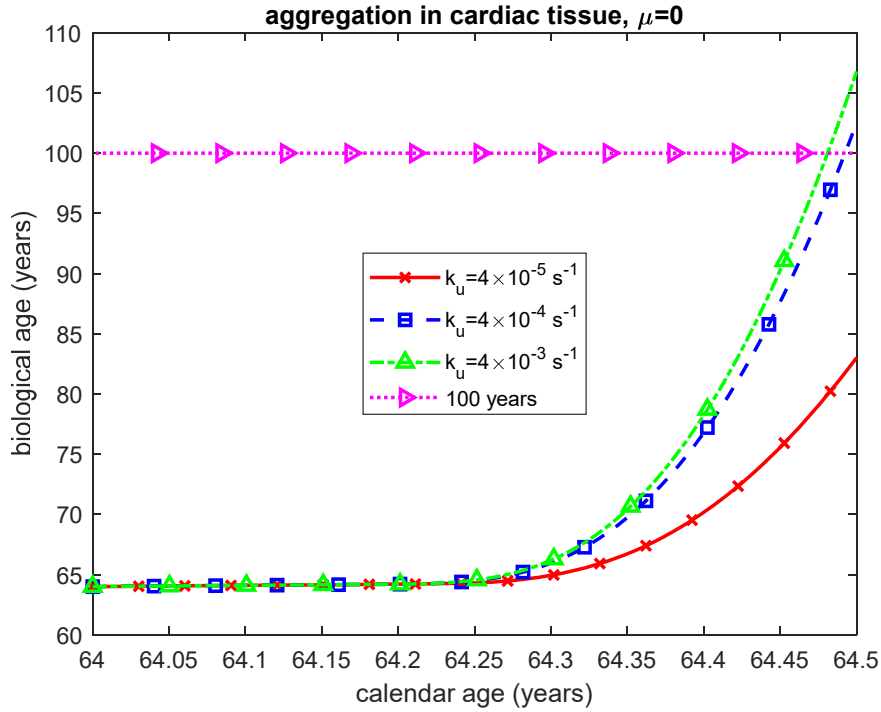

Fig. S18. Biological age vs calendar age under two scenarios: (a) aggregation occurring in the blood plasma and (b) aggregation occurring within the cardiac tissue. Results are shown for three different values of the rate of unfolding of LCs, k_u. Computations were performed for $k_1 = 10^{-6}$ s^{-1}, $k_2 = 10^{-6}$ μM^{-1} s^{-1}, $q_{LC} = 10^5 \ \frac{\text{LC molecules}}{\text{cell s}}$, $\theta_{1/2,B} = 10^7$ s, and $\theta_{1/2,I} = 10^7$ s. The case without anticancer therapy.

(a)

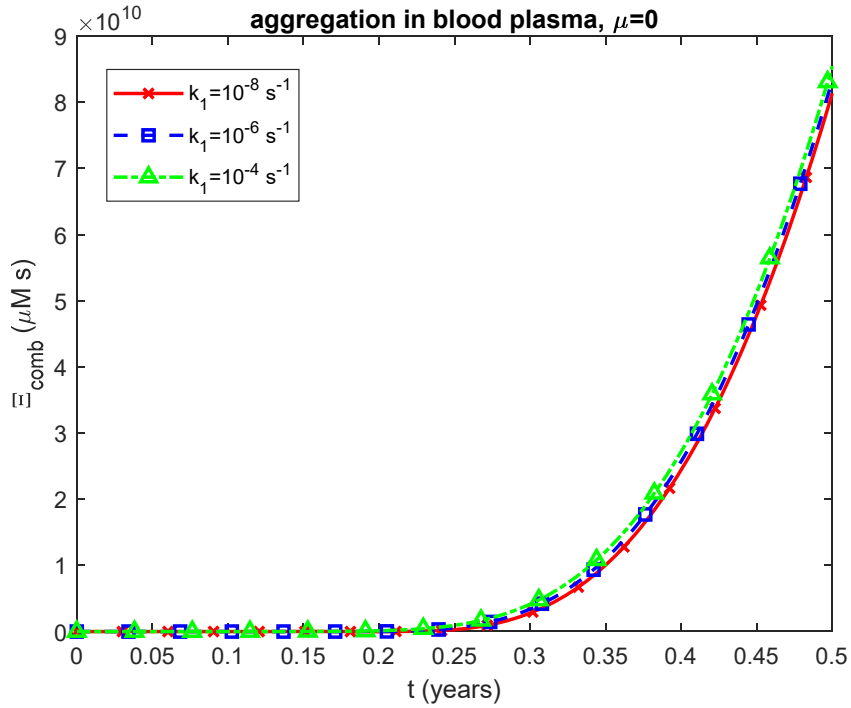

(b)

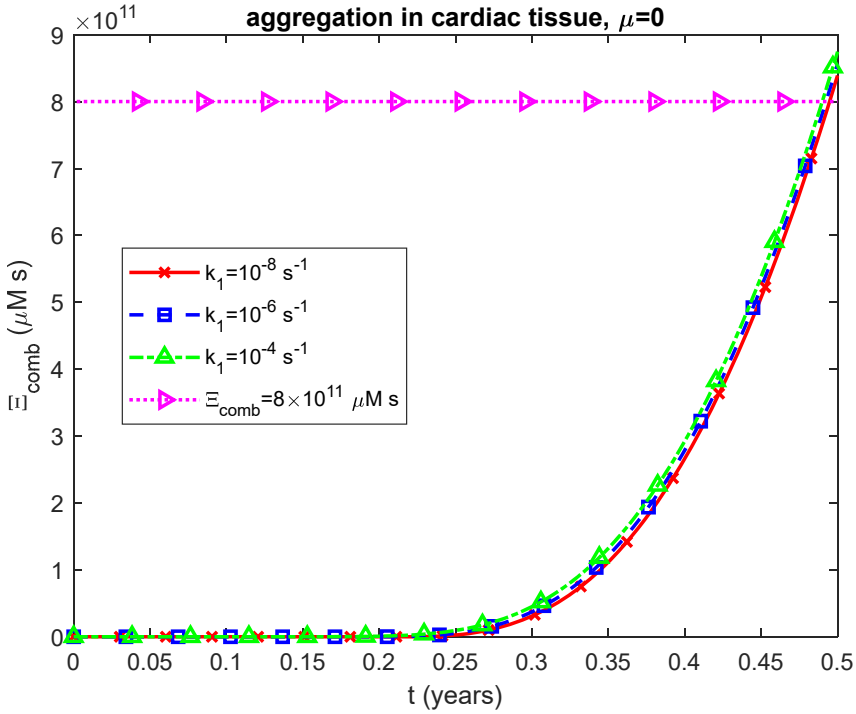

Fig. S19. Time-dependent criterion characterizing the combined effect of cytotoxicity and myocardial stiffening, Ξ_{comb}, vs time, t, for two scenarios: (a) aggregation occurring in the blood plasma and (b) aggregation occurring within the cardiac tissue. Results are shown for three different values of the rate

constant describing the first pseudoelementary (nucleation) step in the F-W model of LC oligomer formation, k_1. Computations were performed for $k_2 = 10^{-6}$ μM^{-1} s^{-1}, $k_u = 4\times10^{-4}$ s^{-1}, $q_{LC} = 10^5$ $\frac{\text{LC molecules}}{\text{cell s}}$, $\theta_{1/2,B} = 10^7$ s, and $\theta_{1/2,I} = 10^7$ s. The case without anticancer therapy.

(a)

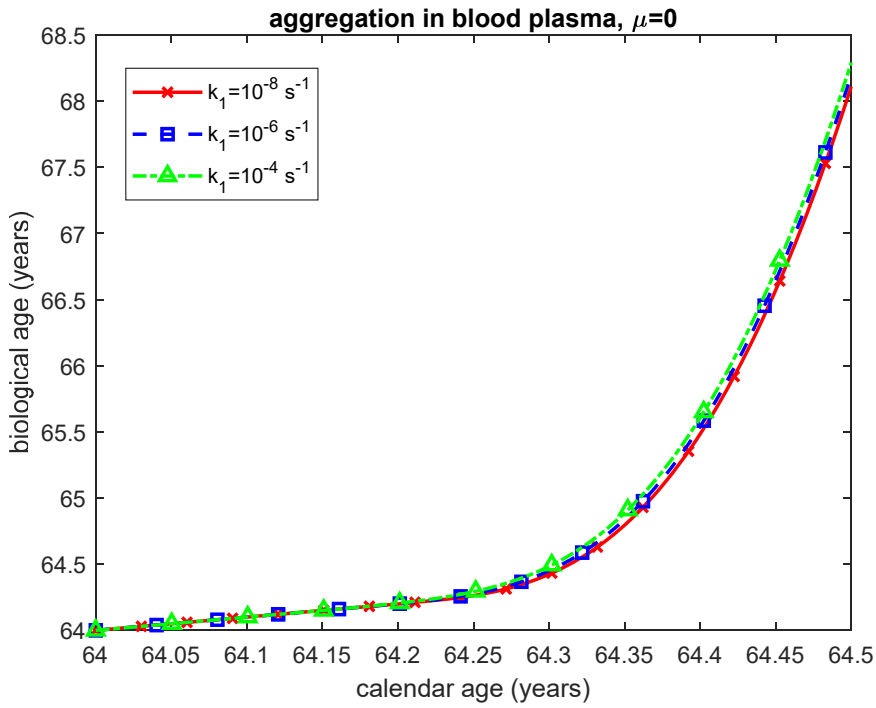

(b)

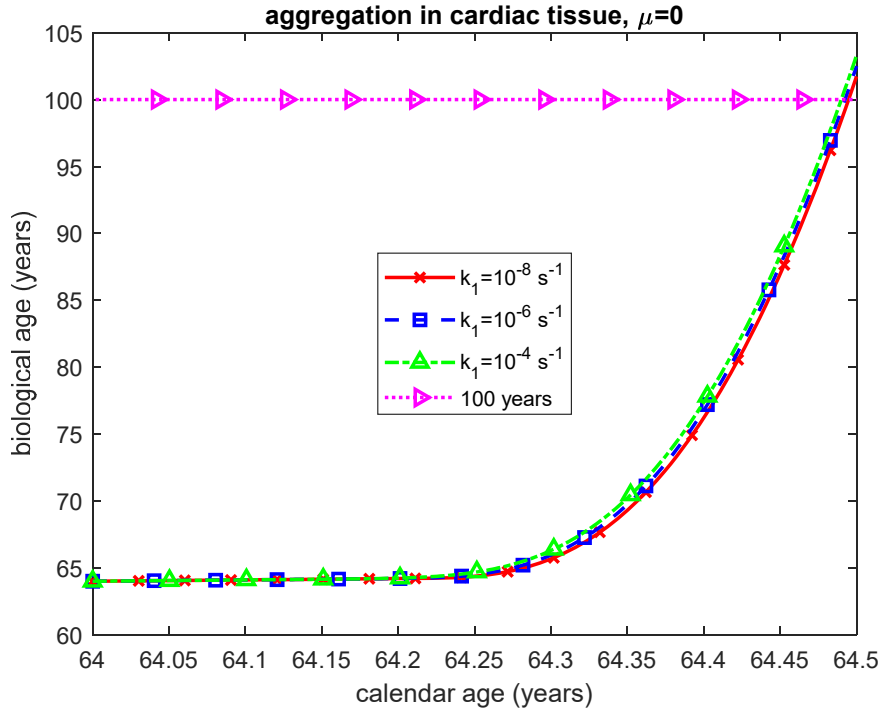

Fig. S20. Biological age vs calendar age under two scenarios: (a) aggregation occurring in the blood plasma and (b) aggregation occurring within the cardiac tissue. Results are shown for three different values of the rate constant describing the first pseudoelementary (nucleation) step in the F-W model of LC oligomer formation, k_1. Computations were performed for $k_2 = 10^{-6}$ μM^{-1} s^{-1}, $k_u = 4\times10^{-4}$ s^{-1}, $q_{LC} = 10^5 \ \frac{\text{LC molecules}}{\text{cell s}}$, $\theta_{1/2,B} = 10^7$ s, and $\theta_{1/2,I} = 10^7$ s. The case without anticancer therapy.

(a)

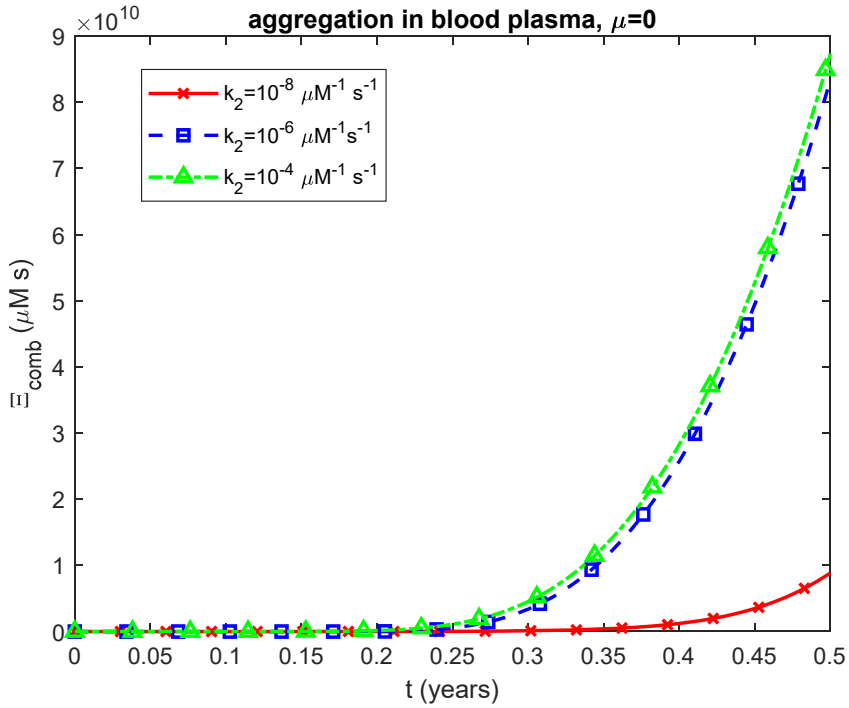

(b)

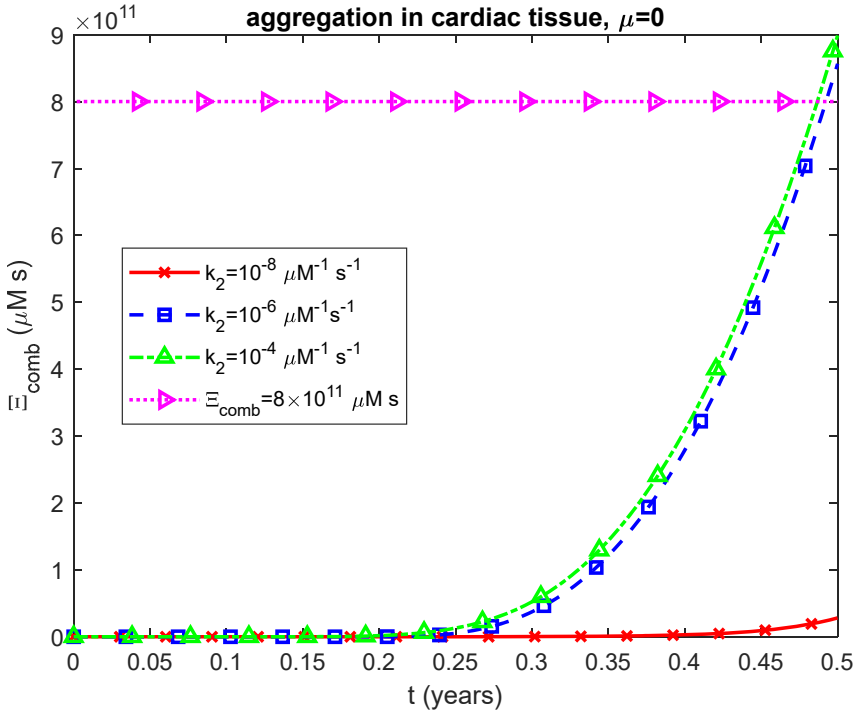

Fig. S21. Time-dependent criterion characterizing the combined effect of cytotoxicity and myocardial stiffening, Ξ_{comb}, vs time, t, for two scenarios: (a) aggregation occurring in the blood plasma and (b) aggregation occurring within the cardiac tissue. Results are shown for three different values of the rate

constant describing the second pseudoelementary (autocatalytic growth) step in the F-W model of LC oligomer formation, k_2. Computations were performed for $k_1 = 10^{-6}$ s^{-1}, $k_u = 4\times10^{-4}$ s^{-1}, $q_{LC} = 10^5$ $\frac{\text{LC molecules}}{\text{cell s}}$, $\theta_{1/2,B} = 10^7$ s, and $\theta_{1/2,I} = 10^7$ s. The case without anticancer therapy.

(a)

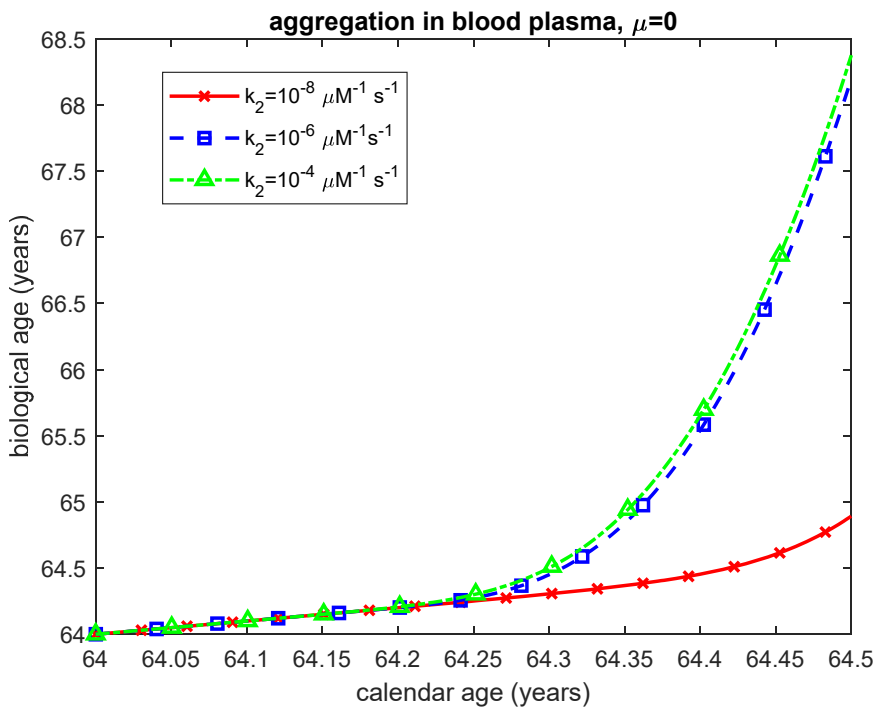

(b)

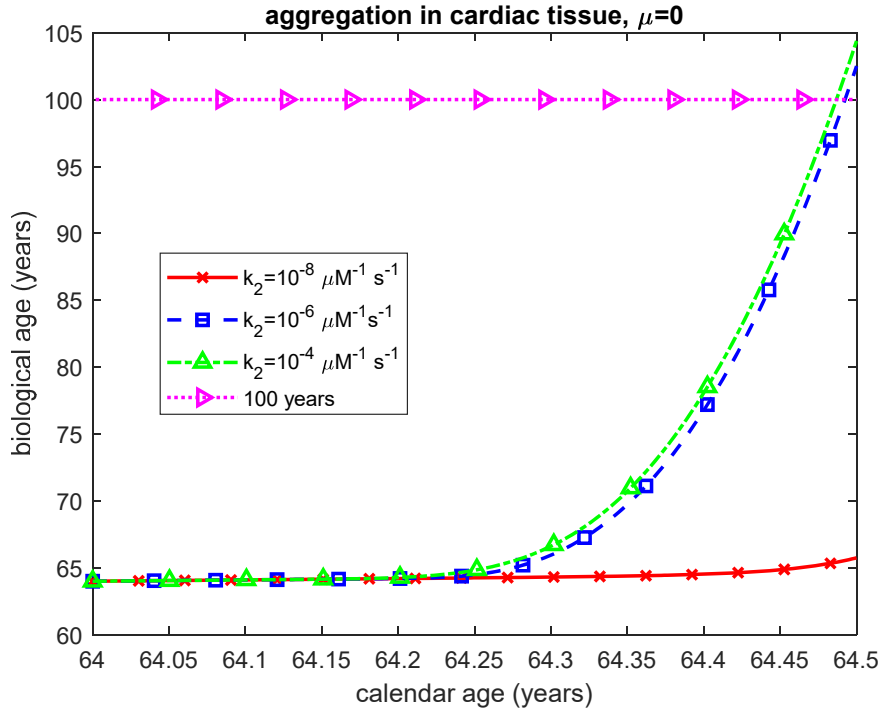

Fig. S22. Biological age vs calendar age for two scenarios: (a) aggregation occurring in the blood plasma and (b) aggregation occurring within the cardiac tissue. Results are shown for three different values of the rate constant describing the second pseudoelementary (autocatalytic growth) step in the F-W model of LC oligomer formation, k_2. Computations were performed for $k_1 = 10^{-6}$ s^{-1}, $k_u = 4\times10^{-4}$ s^{-1}, $q_{LC} = 10^5$ $\frac{\text{LC molecules}}{\text{cell s}}$, $\theta_{1/2,B} = 10^7$ s, and $\theta_{1/2,I} = 10^7$ s. The case without anticancer therapy.

(a)

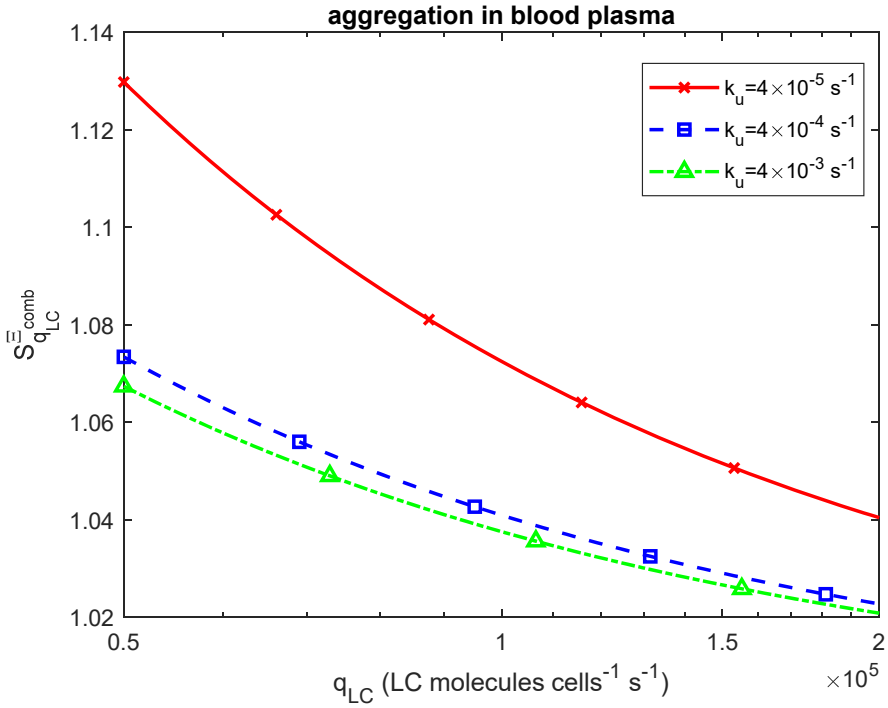

(b)

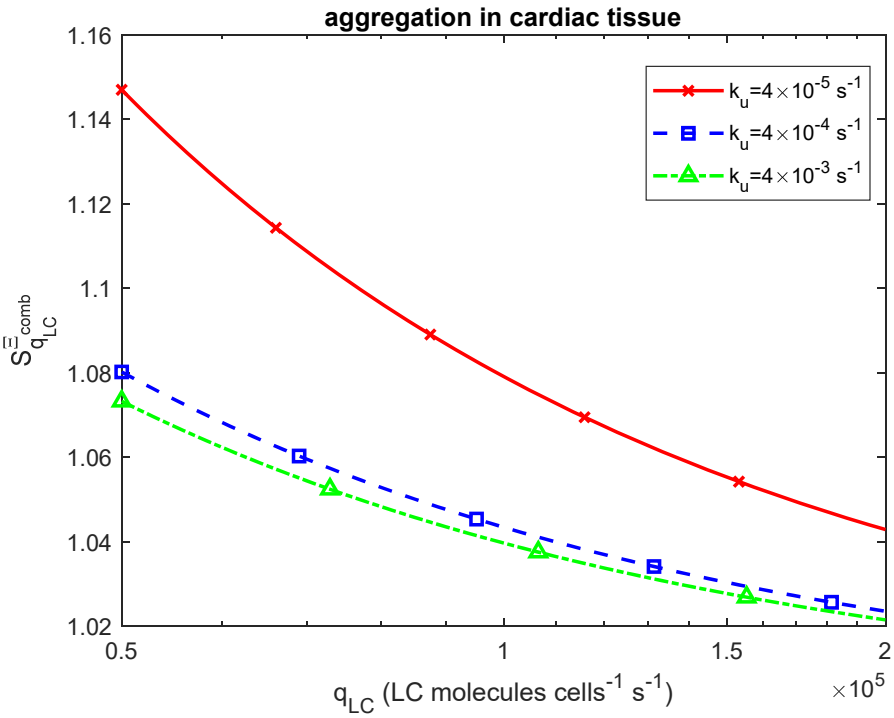

Fig. S23. Dimensionless sensitivity of the criterion characterizing the combined effects of cytotoxicity and myocardial stiffening to the rate of secretion of folded LCs by a single plasma cell belonging to a clonal population, $S^{\Xi_{comb}}_{q_{LC}}$, vs q_{LC}. Results are presented at six months following disease onset for three

different values of the LC unfolding rate constant, k_u. Computations were performed for $k_1 = 10^{-6}$ s^{-1}, $k_2 = 10^{-6}$ μM^{-1} s^{-1}, $\theta_{1/2,B} = 10^7$ s, and $\theta_{1/2,I} = 10^7$ s. The case without anticancer therapy.

(a)

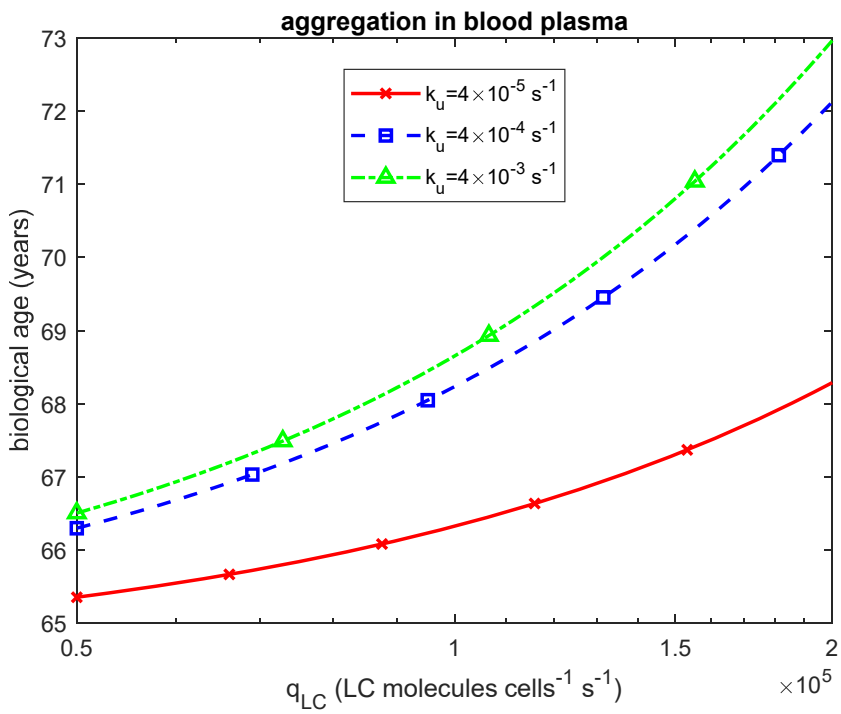

(b)

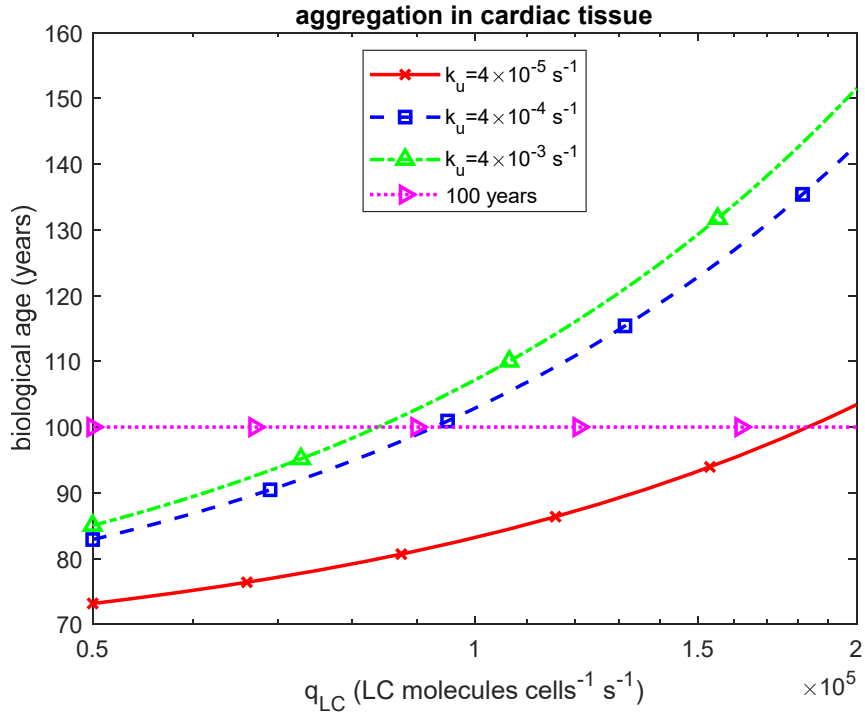

Fig. S24. Biological age vs the rate of secretion of folded LCs by a single plasma cell belonging to a clonal population after six months of the disease for two scenarios: (a) aggregation occurring in the blood plasma and (b) aggregation occurring within the cardiac tissue. Results are shown for three different values of the rate of unfolding of LCs, k_u. Computations were performed for $k_1 = 10^{-6}$ s^{-1}, $k_2 = 10^{-6}$ μM^{-1} s^{-1}, $\theta_{1/2,B} = 10^7$ s, and $\theta_{1/2,I} = 10^7$ s. The case without anticancer therapy.

(a)

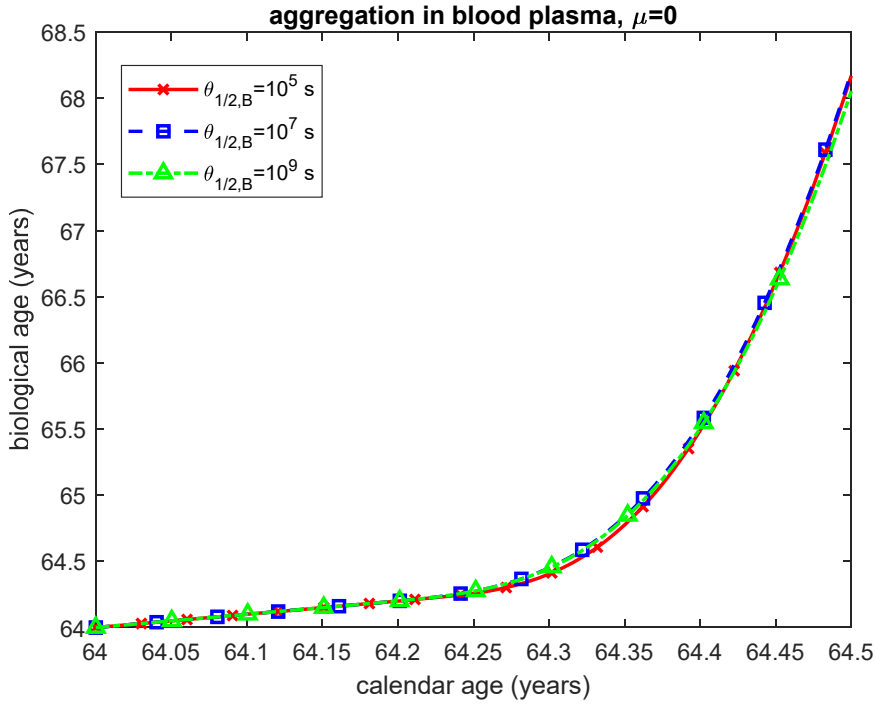

(b)

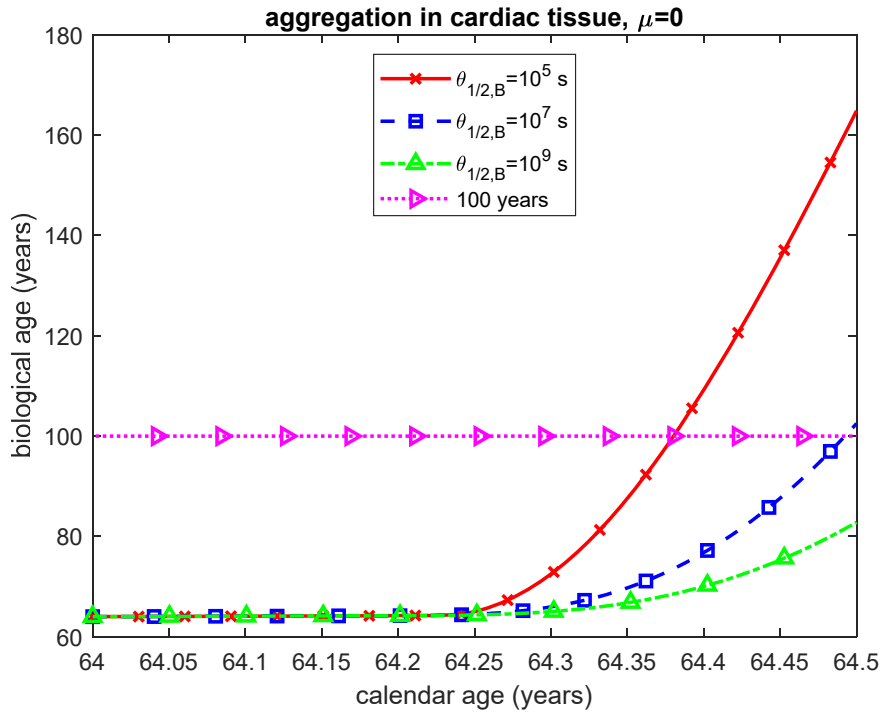

Fig. S25. Biological age vs calendar age for two scenarios: (a) aggregation occurring in the blood plasma and (b) aggregation occurring within the cardiac tissue. Results are shown for three different values of the half-deposition time for free LC oligomers to be incorporated into LC fibrils, $\theta_{1/2,B}$. Computations were

performed for $k_1 = 10^{-6}$ s^{-1}, $k_2 = 10^{-6}$ μM^{-1} s^{-1}, $k_u = 4\times10^{-4}$ s^{-1}, $q_{LC} = 10^5 \ \frac{\text{LC molecules}}{\text{cell s}}$, and $\theta_{1/2,I} = 10^7$ s. The case without anticancer therapy.

(a)

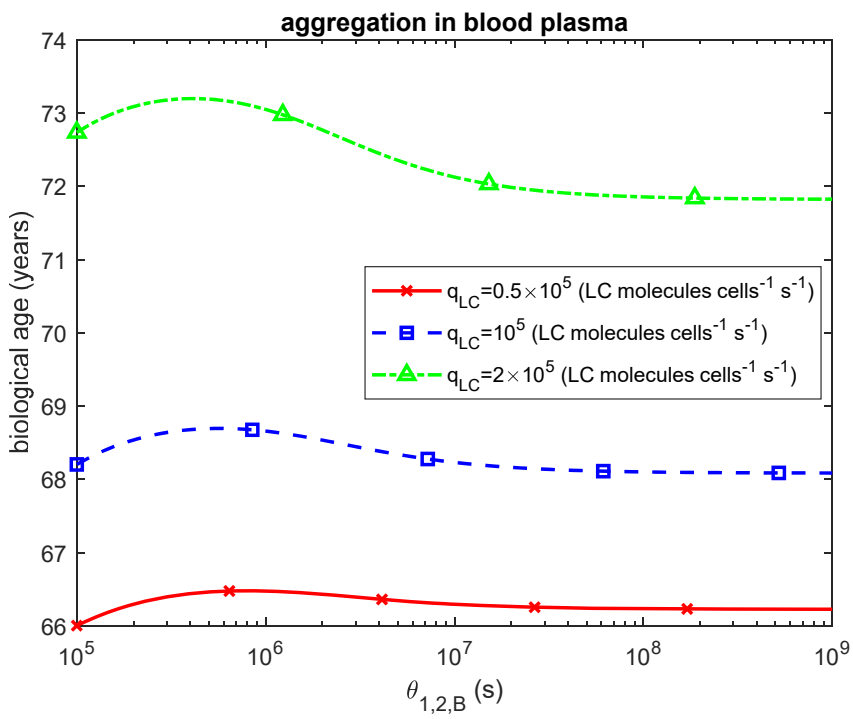

(b)

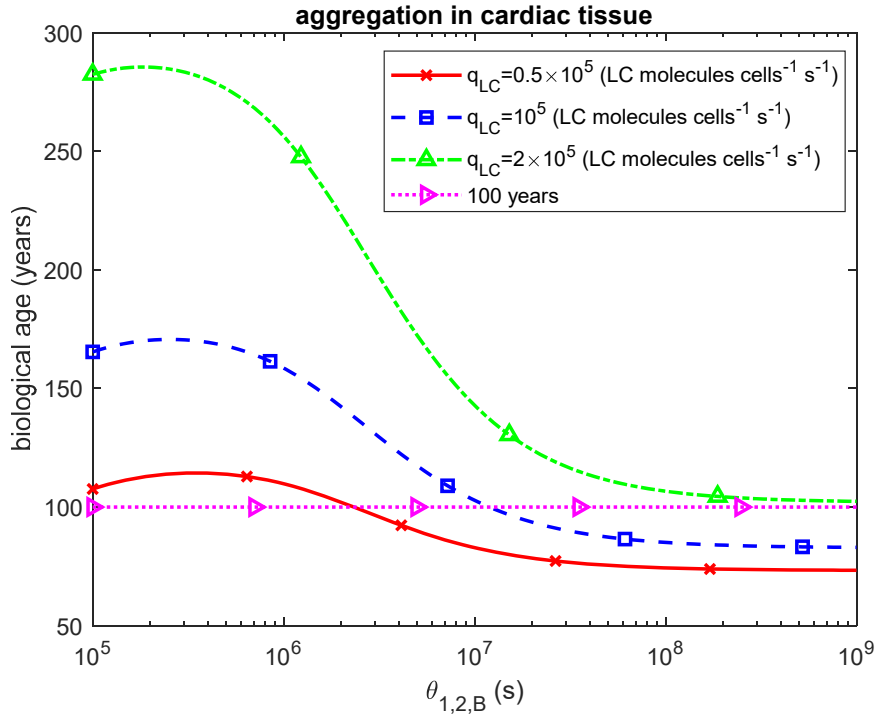

Fig. S26. Biological age vs the half-deposition time for free LC oligomers to be incorporated into LC fibrils after six months of the disease for two scenarios: (a) aggregation occurring in the blood plasma and (b) aggregation occurring within the cardiac tissue. Results are presented for three different values of the secretion rate of folded LCs produced by a single plasma cell belonging to a clonal population, q_{LC}. Computations were performed for $k_1 = 10^{-6}$ s^{-1}, $k_2 = 10^{-6}$ μM^{-1} s^{-1}, $k_u = 4\times10^{-4}$ s^{-1}, and $\theta_{1/2,I} = 10^7$ s. The case without anticancer therapy.

(a)

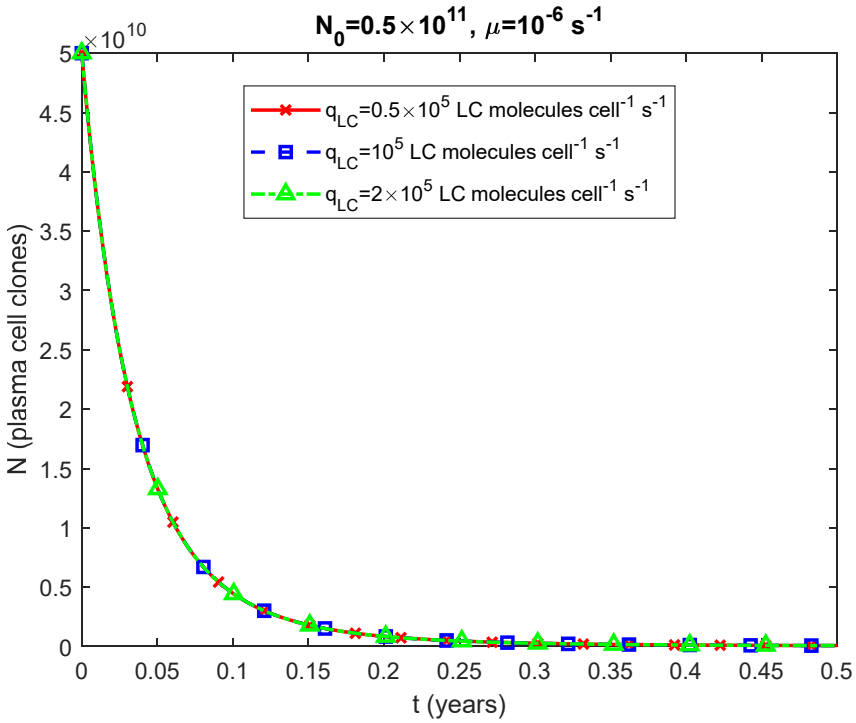

(b)

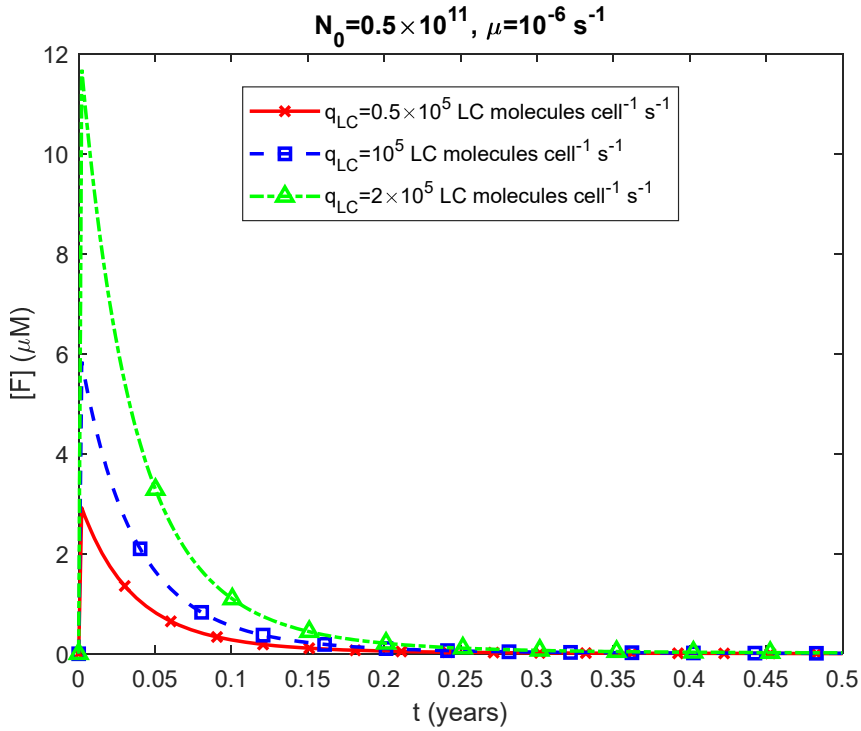

Fig. S27. (a) Number of plasma cell clones, *N*, vs time, *t*. The results indicate that this parameter is independent of q_{LC}. (b) Plasma molar concentration of natively folded Ig LC monomers secreted by clonal plasma cells vs time for three different values of the secretion rate of folded LCs per single plasma

cell belonging to a clonal population, q_{LC}. Computations were performed for $k_u = 4\times10^{-4}$ s^{-1}. The case with anticancer therapy.

(a)

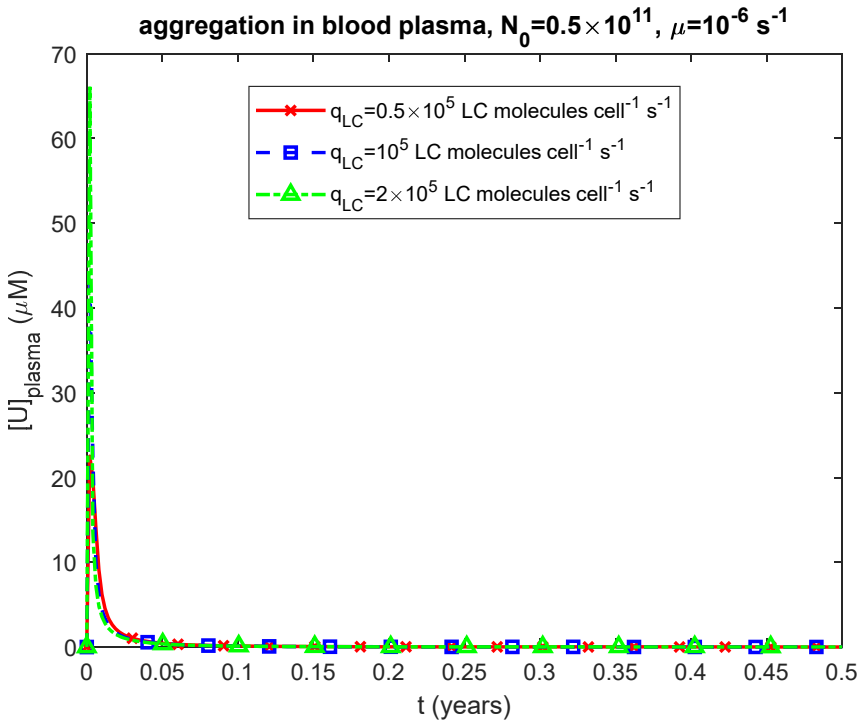

(b)

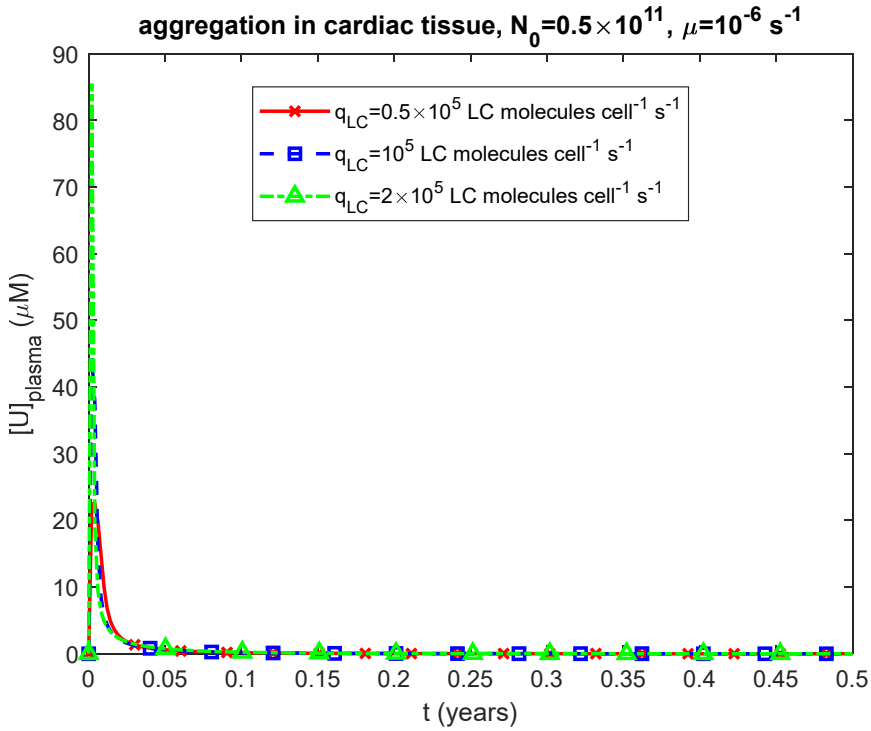

Fig. S28. Plasma molar concentration of unfolded Ig LC monomers susceptible to aggregation, $[U]_{plasma}$, vs time, *t*, for the scenarios of (a) aggregation occurring in the blood plasma and (b) aggregation occurring within the cardiac tissue. Results are shown for three different values of the secretion rate of folded LCs produced by a single plasma cell belonging to a clonal population, q_{LC}. Computations were performed for $k_1 = 10^{-6}$ s^{-1}, $k_2 = 10^{-6}$ μM^{-1} s^{-1}, $k_u = 4\times10^{-4}$ s^{-1}, $\theta_{1/2,B} = 10^7$ s, and $\theta_{1/2,I} = 10^7$ s. The case with anticancer therapy.

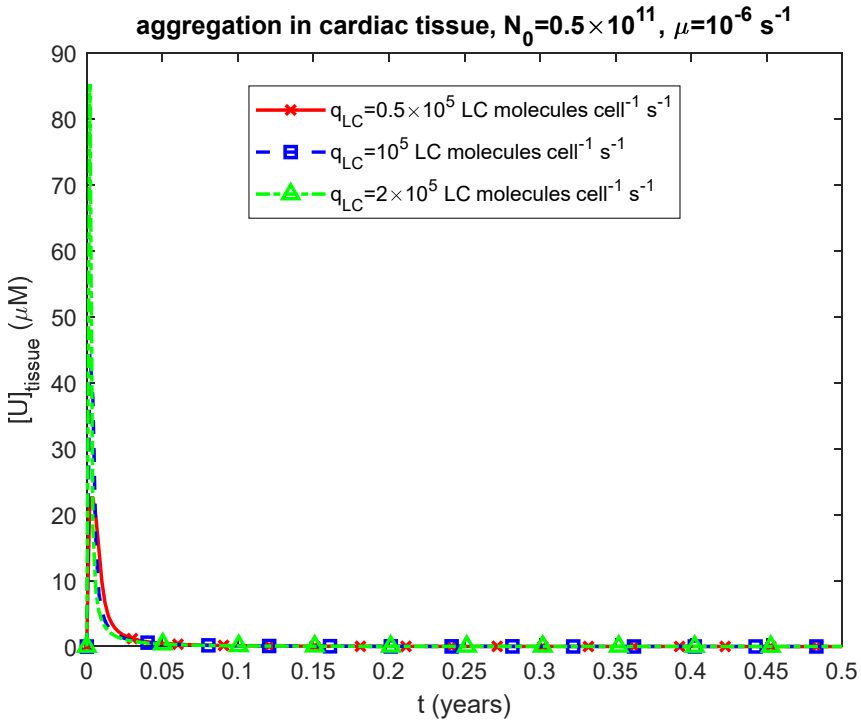

Fig. S29. Molar concentration of unfolded Ig LC monomers in cardiac tissue, $[U]_{tissue}$, vs time, t, for the scenario where aggregation occurs within the tissue. Results are shown for three different values of the secretion rate of folded LCs produced by a single plasma cell belonging to a clonal population, q_{LC}. Computations were performed for $k_1 = 10^{-6}$ s^{-1}, $k_2 = 10^{-6}$ μM^{-1} s^{-1}, $k_u = 4\times10^{-4}$ s^{-1}, and $\theta_{1/2,B} = 10^7$ s. The case with anticancer therapy.

(a)

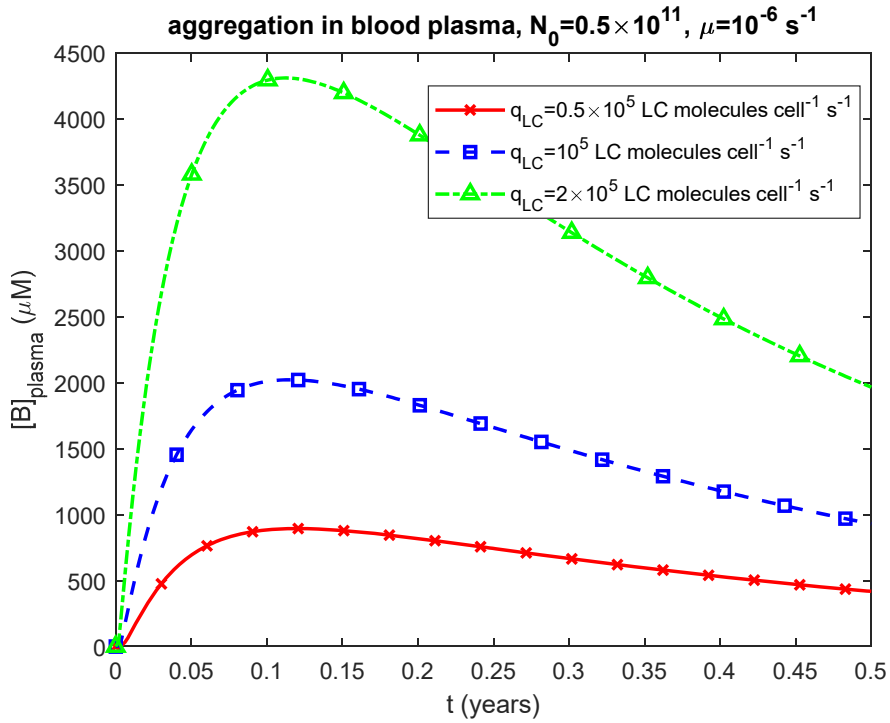

(b)

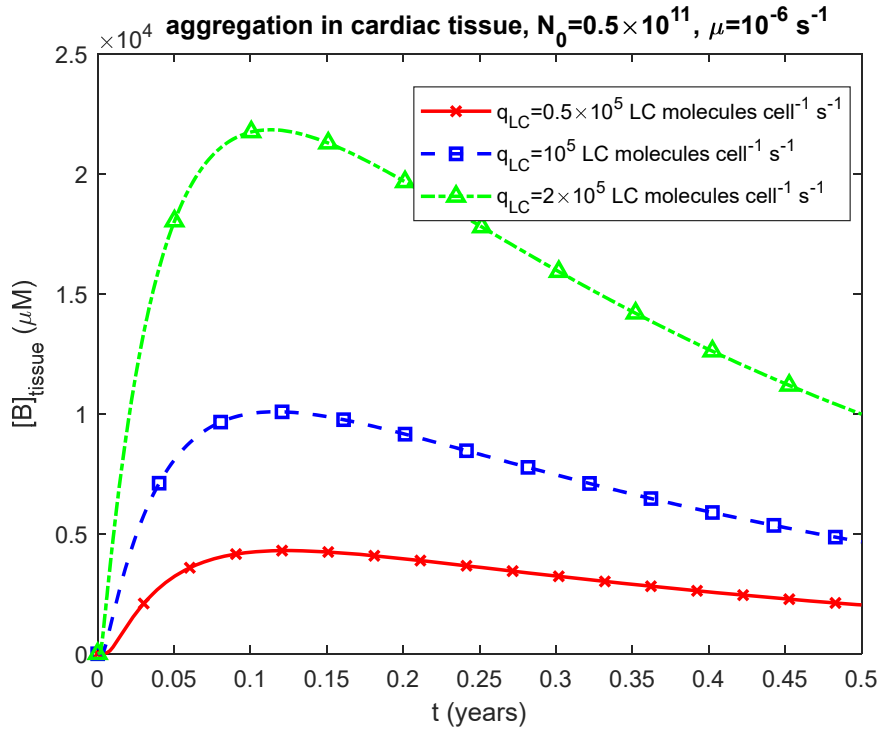

Fig. S30. (a) Molar concentration of free LC oligomers in blood plasma, $[B]_{plasma}$, vs time, t, when aggregation occurs in the plasma, and (b) molar concentration of free LC oligomers in cardiac tissue,

$[B]_{tissue}$, vs time, t, when aggregation occurs within the tissue. Results are shown for three different values of the secretion rate of folded LCs produced by a single plasma cell belonging to a clonal population, q_{LC}. Computations were performed for $k_1 = 10^{-6}$ s^{-1}, $k_2 = 10^{-6}$ μM^{-1} s^{-1}, $k_u = 4\times10^{-4}$ s^{-1}, $\theta_{1/2,B} = 10^7$ s, and $\theta_{1/2,I} = 10^7$ s. The case with anticancer therapy.

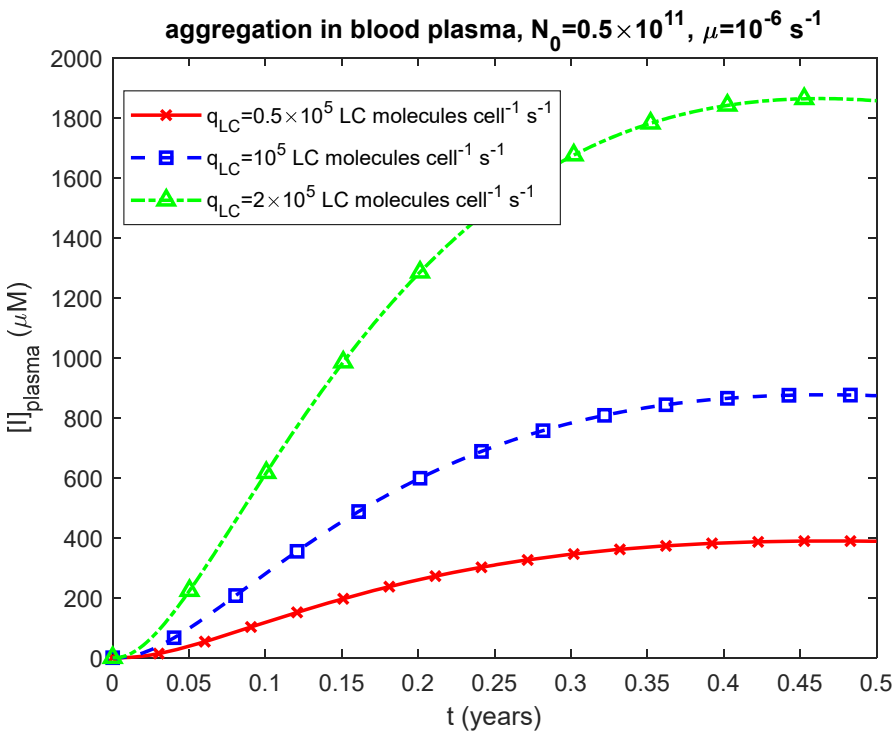

Fig. S31. Molar concentration of LC oligomers deposited into amyloid protofibrils circulating within blood plasma, $[I]_{plasma}$, vs time, t. Results are shown for three different values of the secretion rate of folded LCs produced by a single plasma cell belonging to a clonal population, q_{LC}. Computations were performed for $k_1 = 10^{-6}$ s^{-1}, $k_2 = 10^{-6}$ μM^{-1} s^{-1}, $k_u = 4\times10^{-4}$ s^{-1}, $\theta_{1/2,B} = 10^7$ s, and $\theta_{1/2,I} = 10^7$ s. The case with anticancer therapy.

(a)

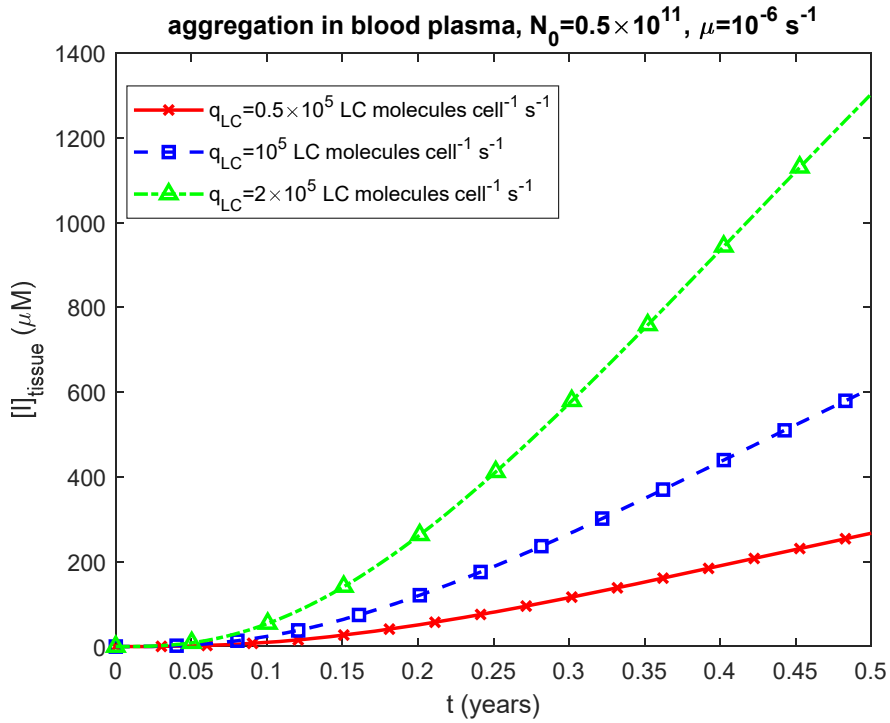

(b)

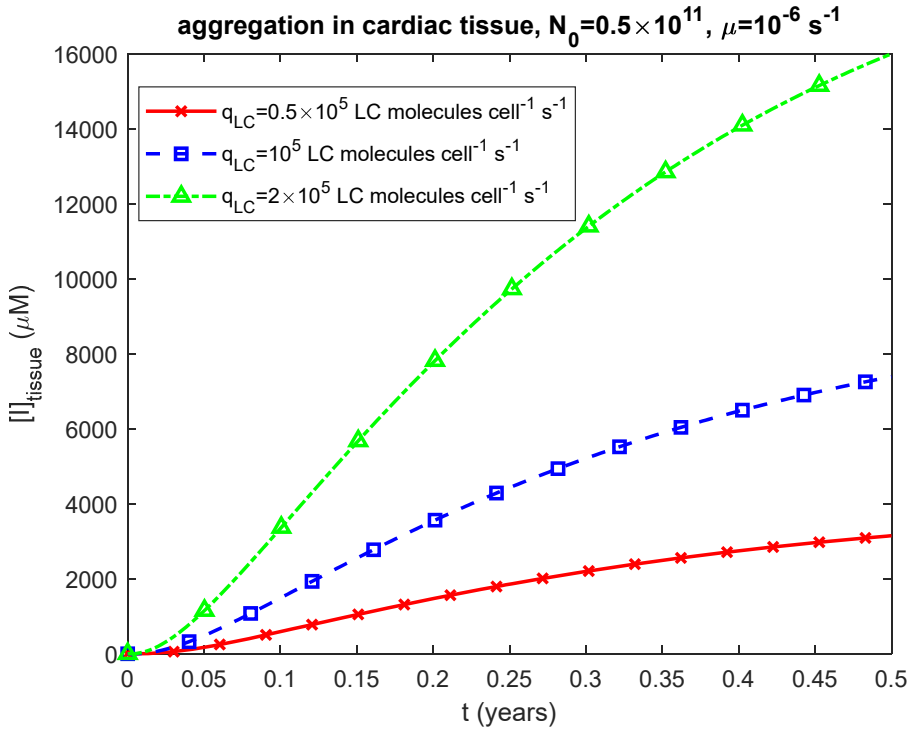

Fig. S32. Molar concentration of LC oligomers incorporated into amyloid fibrils infiltrating the cardiac tissue, $[I]_{tissue}$, vs time, t, for two scenarios: (a) aggregation occurring in the blood plasma and (b) aggregation occurring within the cardiac tissue. Results are shown for three different values of the

secretion rate of folded LCs produced by a single plasma cell belonging to a clonal population, q_{LC}. Computations were performed for $k_1 = 10^{-6}$ s^{-1}, $k_2 = 10^{-6}$ μM^{-1} s^{-1}, $k_u = 4\times10^{-4}$ s^{-1}, $\theta_{1/2,B} = 10^7$ s, and $\theta_{1/2,I} = 10^7$ s. The case with anticancer therapy.

(a)

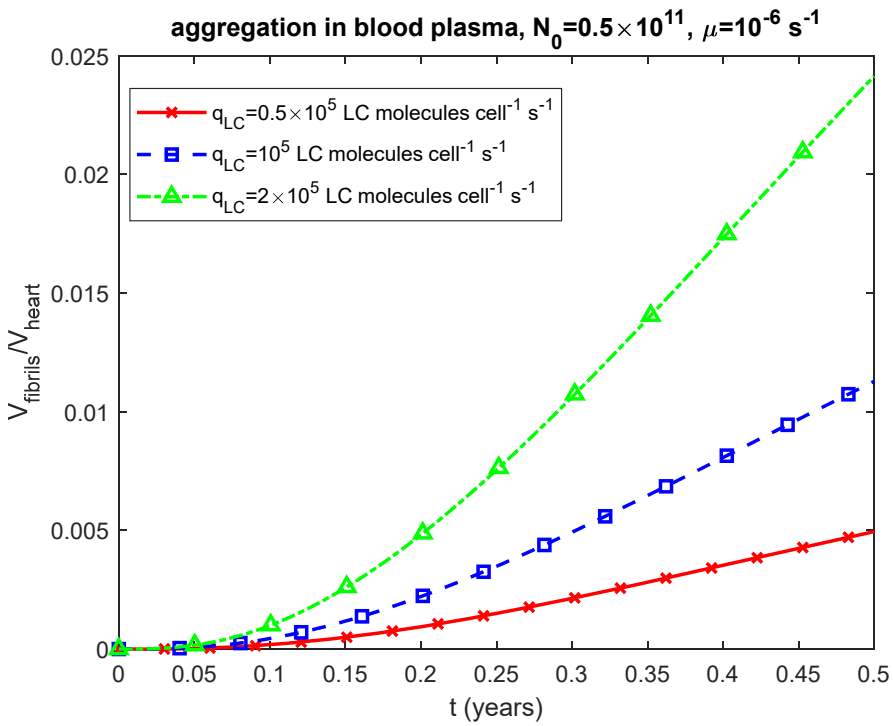

(b)

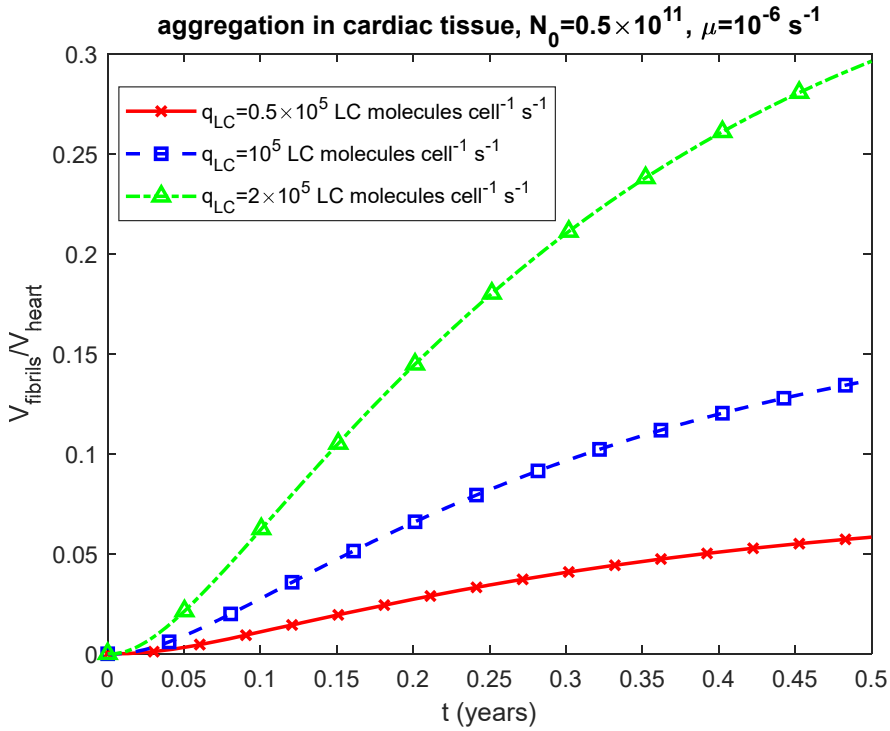

Fig. S33. Fraction of myocardial volume occupied by LC fibrils, $V_{fibrils} / V_{heart}$, vs time, t, for two scenarios: (a) aggregation occurring in the blood plasma and (b) aggregation occurring within the cardiac tissue. Results are presented for three different values of the secretion rate of folded LCs produced by a single plasma cell belonging to a clonal population, q_{LC}. Computations were performed for $k_1 = 10^{-6}$ s^{-1}, $k_2 = 10^{-6}$ μM^{-1} s^{-1}, $k_u = 4\times10^{-4}$ s^{-1}, $\theta_{1/2,B} = 10^7$ s, and $\theta_{1/2,I} = 10^7$ s. The case with anticancer therapy.

(a)

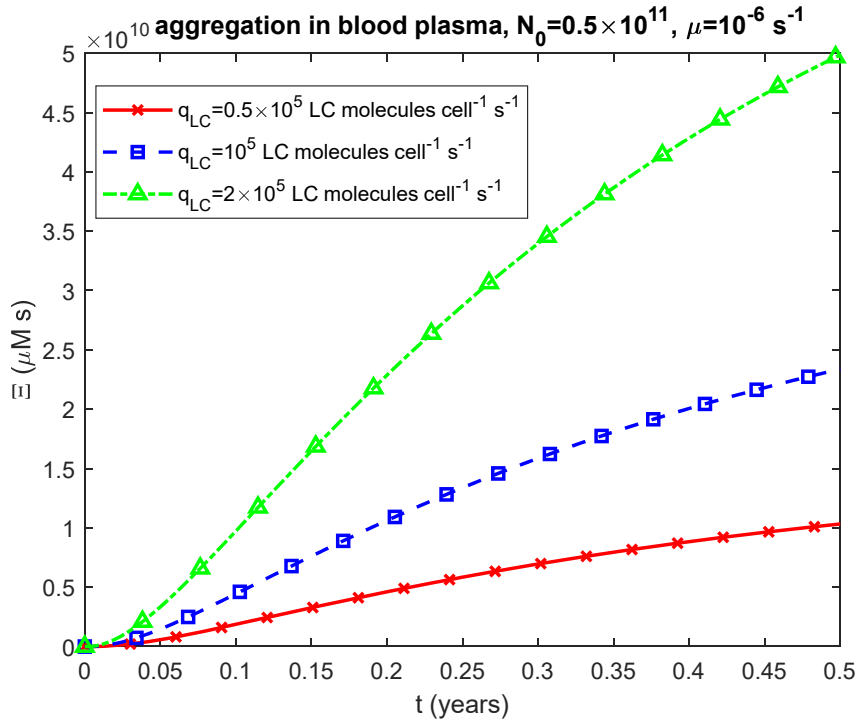

(b)

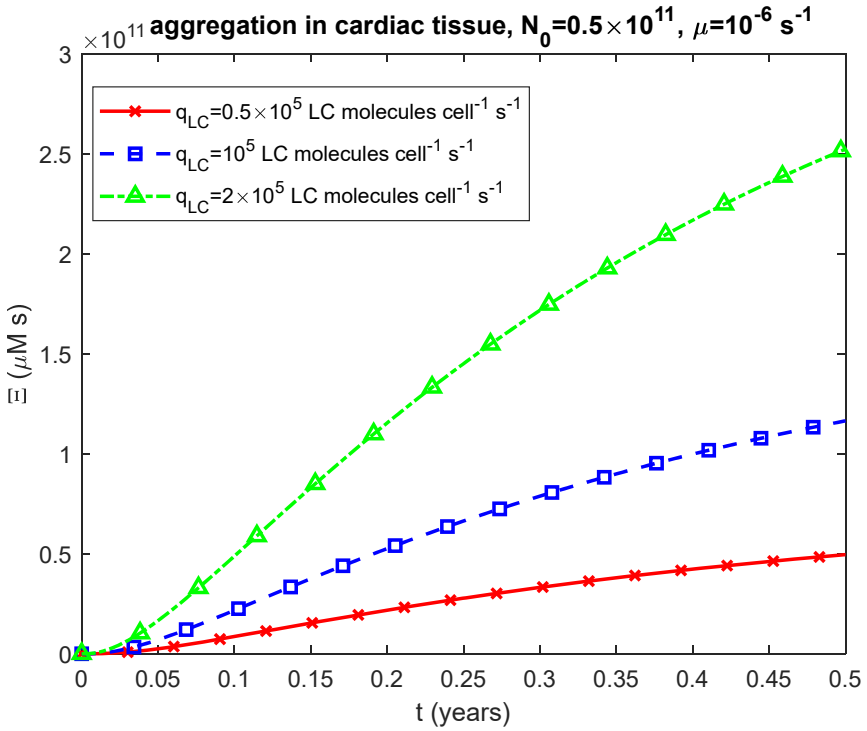

Fig. S34. Time-dependent criterion for accumulated cardiotoxicity induced by LC oligomers, Ξ, vs time, *t*, for two scenarios: (a) aggregation occurring in the blood plasma and (b) aggregation occurring within the cardiac tissue. Results are presented for three different values of the secretion rate of folded LCs

produced by a single plasma cell belonging to a clonal population, q_{LC}. Computations were performed for $k_1 = 10^{-6}$ s^{-1}, $k_2 = 10^{-6}$ μM^{-1} s^{-1}, $k_u = 4\times10^{-4}$ s^{-1}, $\theta_{1/2,B} = 10^7$ s, and $\theta_{1/2,I} = 10^7$ s. The case with anticancer therapy.

(a)

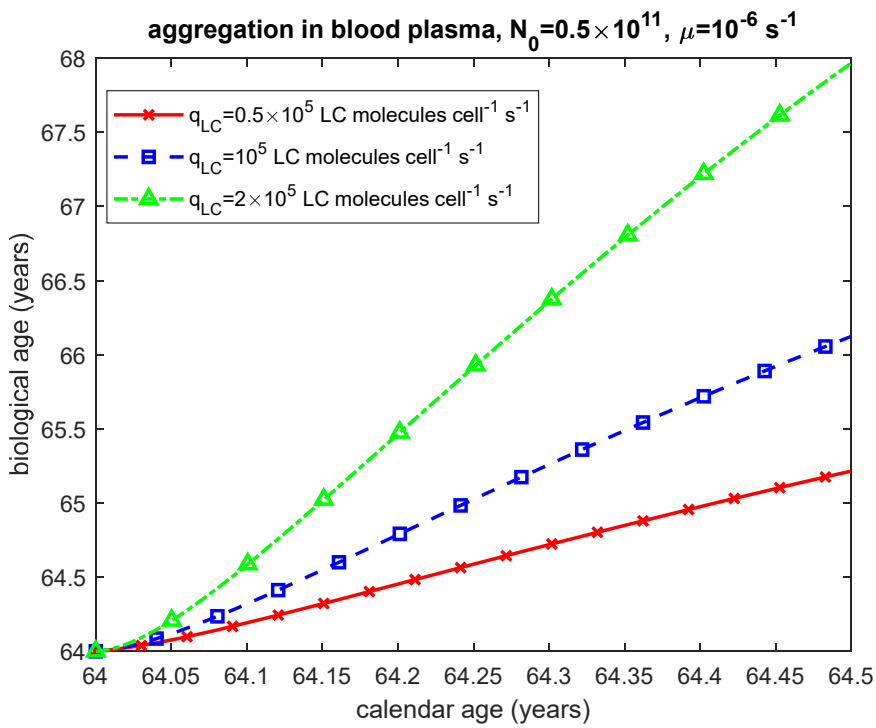

(b)

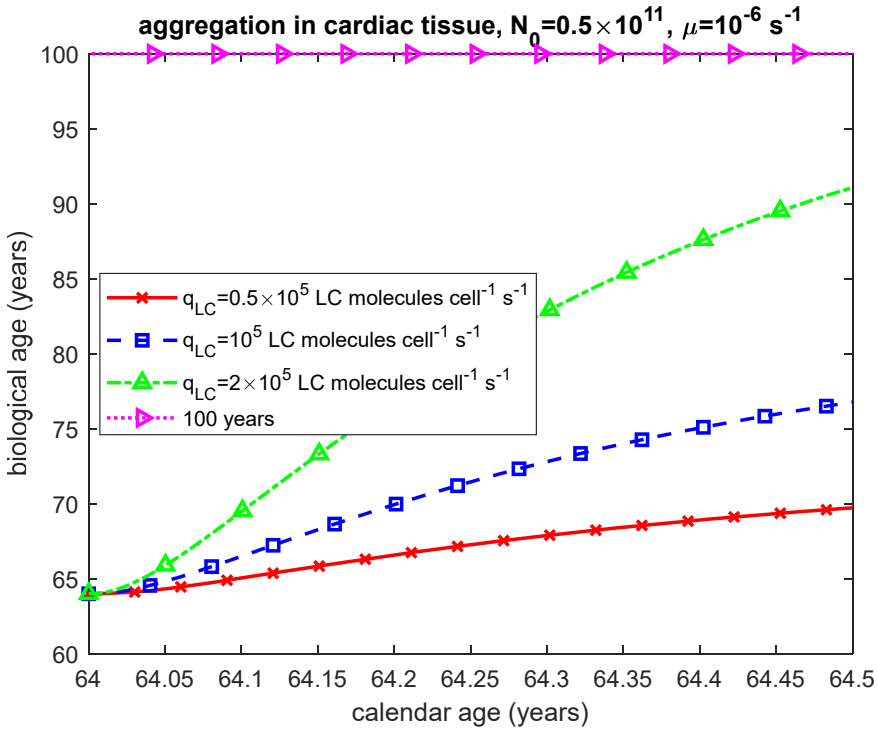

Fig. S35. Biological age vs calendar age under two scenarios: (a) aggregation occurring in the blood plasma and (b) aggregation occurring within the cardiac tissue. Results are presented for three different values of the secretion rate of folded LCs produced by a single plasma cell belonging to a clonal population, q_{LC}. Computations were performed for $k_1 = 10^{-6}$ s^{-1}, $k_2 = 10^{-6}$ μM^{-1} s^{-1}, $k_u = 4\times10^{-4}$ s^{-1}, $\theta_{1/2,B} = 10^7$ s, and $\theta_{1/2,I} = 10^7$ s. The case with anticancer therapy.